Understanding and Controlling the Degradation Mechanisms at Cathode-Electrolyte Interfaces in All-Solid-State Lithium-Ion Batteries

by

Younggyu Kim

B.S., Materials Science and Engineering, Seoul National University, Republic of Korea, 2017

Submitted to the Department of Materials Science and Engineering
in Partial Fulfillment of the Requirements for the Degree of

Doctor of Philosophy

at the

MASSACHUSETTS INSTITUTE OF TECHNOLOGY

May 2022

Signature of Author……

Younggyu Kim

Department of Materials Science and Engineering

May 13, 2022

Certified by……

Bilge Yildiz

Breene M. Kerr (1951) Professor

Professor of Nuclear Science and Engineering

Professor of Materials Science and Engineering

Thesis Supervisor

Accepted by……...

Frances M. Ross

Ellen Swallow Richards Professor in Materials Science and Engineering

Chair, Department Committee on Graduate Studies

Understanding and Controlling the Degradation Mechanisms at Cathode-Electrolyte Interfaces in All-Solid-State Lithium-Ion Batteries

by

Younggyu Kim

Submitted to the Department of Materials Science and Engineering on May 13, 2022 in Partial Fulfillment of the Requirements for the Degree of Doctor of Philosophy in Materials Science and Engineering

ABSTRACT

All-Solid-State Li-ion Batteries with $Li_7La_3Zr_2O_{12}$ solid electrolyte enable higher energy density compared to conventional batteries with liquid electrolytes since they are compatible with Lithium metal anode. Despite their promises, stability issues at the interface between cathode and solid electrolyte need to be solved for their implementation. The interface needs to be chemically stable at high temperature during sintering. Electrochemical and chemo-mechanical stabilities at the interface are necessary during the operation of the battery for good cyclability. In order to study interfacial stabilities we developed model system with thin film cathode. The cell design allowed characterization of the interface by interface-sensitive techniques without the needs of destructive techniques. We studied interfacial degradation between $LiNi_{0.6}Mn_{0.2}Co_{0.2}O_2$ (NMC622) cathode, and $Li_7La_3Zr_2O_{12}$ (LLZO) solid electrolyte. We evaluated thermal stability in controlled gas environments (Air, O_2, N_2, humidified O_2, CO_2) to identify contributors for secondary phase formations and their effect on charge transfer properties. Li_2CO_3, $La_2Zr_2O_7$, and $La(Ni,Co)O_3$ formed at the NMC622|LLZO interface when annealed at 700 °C in air, which increased the interfacial resistance by 2 orders of magnitude. Sintering in gas environment without CO_2 and H_2O (g) was necessary to obtain chemically stable interfaces. Sintering in O_2 gave excellent chemical stability and interfacial resistance comparable to lowest values obtained in literature with protective coatings at the interface. Sintering in N_2 caused oxygen loss at high temperature, but secondary phases did not form. NMC622|LLZO interface was electrochemically unstable due to limited oxidation stability of LLZO. Electrochemical degradation at the interface reduced Ni

during potentiostatic hold at 4.3 V vs Li/Li^+, and formed reduced phases with Ni^{2+} and Co^{2+} from cycling at 80 °C. Electrochemical degradation decreased capacities by overpotential increase. Reduction was not observable when cycling temperature was lowered to room temperature, indicating that the reaction could be kinetically inhibited. Stress due to lattice parameter changes of NMC622 during cycling caused intergranular cracks in NMC622 film and delamination at NMC622|LLZO interface. Chemo-mechanical degradation caused abrupt capacity decrease by disconnecting Li-ion conduction pathway, so it should be avoided for better cyclability. Understanding of interfacial degradation offers guidelines for designing All-Solid-State Li-ion batteries with better interfacial stability.

Thesis Supervisor: Bilge Yildiz

Title: Breene M. Kerr (1951) Professor

Professor of Nuclear Science and Engineering

Professor of Materials Science and Engineering

Acknowledgement

I thank my thesis advisor, Professor Bilge Yildiz, I learned how to ask scientific questions, examine experimental results with a keen eye, and share my thoughts with other people from you. I will cherish what I have learned from you. I am also thankful for thesis committee, Professor Yet-Ming Chiang, Professor Ju Li, and thesis area examination chair Professor Frances M. Ross, who gave me valuable advices.

I thank our group members as well. Gulin, thank you for giving me a head start by teaching me how to work with solid electrolytes. I always went back to your work when I felt stuck and needed guidance. Roland, thank you for your patience and guidance during my first few beamtimes. I am forever grateful. I don't think I could have completed my experiments without you. Dongha and Jiayue, thank you for accompanying me through most of my beamtime trips. I felt comfortable and relaxed when I was at the beamline because of you. It really helped. Ji-won, thank you for teaching me how to work with batteries. I remember your help, and I hope there will be a day when I can repay the favor. Georgios and Xiahui, thank you for helping me figuring out all those experimental details needed to make an experiment successful. Your comments were always helpful.

I appreciate help of beamline scientists. Ira and Adrian, thank you for your help and guidance at 23-ID-2 (IOS) NSLS-II. So many figures in this thesis were made by analyzing data obtained at your beamline. Thank you for helping me get the best possible dataset for each beamtime.

Lastly, I thank my family. I could keep moving forward because I knew you were supporting me with love and trust.

Table of Contents

List of figures

1. Introduction

1.1. Overview and working principles of Li-ion batteries

From 1990s when Sony developed their first commercial Li-ion batteries,[1] Li-ion batteries have been the leading choice for storing energy.[2] Li-ion batteries store energy in a portable chemical form, which can be easily converted to electrical energy with high efficiency.[3] Due to its high energy density and good cyclability, Li-ion batteries are used in portable electronic devices, electric vehicles, and large-scale grid energy storage systems.

Li-ion batteries are consisted of three parts. There is a cathode (positive electrode), an anode (negative electrode), and an electrolyte which separates cathode and anode. Cathodes and anodes are mixed ionic conductors, which allow flow of both electrons and Lithium ions. Electrolytes are lithium-ion conductors, and electronic insulators. During charge, electrons are extracted from cathode, and supplied to anode through an external circuit by an external power source. To maintain charge neutrality, Li ions migrate from cathode to anode through electrolyte. Opposite happens during discharge. Electrons travel back from anode to cathode through an external circuit, and Li ion migrates from anode to cathode through electrolyte. Amount of charge that can be extracted from and incorporated into electrodes determines the capacity of the battery. Measured voltage of the cell depends on the difference of electrochemical potential of electrons between cathode and anode.[4]

$$V = \frac{\tilde{\mu}_{e^-}(anode) - \tilde{\mu}_{e^-}(cathode)}{e}$$

Energy density, which is the key parameter for evaluating the performance of Li-ion batteries, can be calculated by multiplying capacity and voltage of the battery and dividing it by weight or volume. Dividing by weight gives gravimetric energy density (unit: Wh/kg), and dividing by volume gives volumetric energy density (unit: Wh/L). Rate capability and cyclability are also important parameters. Rate capability indicates the speed of charge and discharge. 1 C rate means the cell requires 1 h for full charge. 0.5 C rate means it needs 2 h, and 2 C rate means it needs 0.5 h. Cyclability indicates how much charge/discharge capacity decreases as cycling number increases.

1.2. All-solid-state Li-ion batteries with $Li_7La_3Zr_2O_{12}$ solid electrolyte

Next-generation Li-ion batteries should have better safety, and higher energy density compared to current Li-ion batteries. Current batteries based on liquid electrolytes have inherent safety issues due to their flammability. Liquid electrolytes consist ethylene carbonate (EC) mixed with linear carbonate species such as dimethyl carbonate (DMC) and $LiPF_6$ salt.[3] Carbonate solvents have low flash points around 30 °C,[5] and $LiPF_6$ salt can react with carbonate solvents over 60 °C.[6] Thermal instability issues can lead to fire and explosion. The energy density of commercial Li-ion batteries has increased from 80 Wh/kg to ~250 Wh/kg in the last 30 years.[1,7] However, the energy density needs to be increased further for the long range electric vehicles and grid energy storage purposes.[7,8]

Replacing liquid electrolyte to inorganic solid electrolyte eliminates flammability issues since they are not flammable. In order to increase energy density, the solid electrolyte should be compatible with electrodes with high energy density. Compatibility with the lithium metal anode is the most ideal, since the energy density of lithium metal (3860 mA/g) is more than 10 times of energy density of graphite anodes (372 mAh/g) which are currently used in commercial batteries.[2]

In this perspective, $Li_7La_3Zr_2O_{12}$ (LLZO) is the most promising solid electrolyte due to its excellent anode side stability which makes it compatible with lithium metal anode. Han et al.[9] and Richards et al.,[10] predicted 0.05 V vs Li/Li^+ and 0.07 V vs Li/Li^+ as stability limit of LLZO against reduction respectively. Although the predicted stability limit for reduction of LLZO is still slightly higher than oxidation potential of lithium metal, experimental studies reported electrochemical stability at LLZO|Li interface. Overpotentials form cycling experiments with symmetric Li|LLZO|Li cells remained constant as cycling number increased, which demonstrates non-existence of secondary chemical reactions at LLZO|Li interface during cycling.[11] Although there are still issues related to lithium dendrite growth through grain boundaries of LLZO,[12,13] many recent works have shown promising strategies to solve the issue.[14–16]

1.3. Cathode side interfacial issues of $Li_7La_3Zr_2O_{12}$

1.3.1. Computationally predicted chemical instabilities at cathode|$Li_7La_3Zr_2O_{12}$ interface

Unlike the excellent stability against reduction, LLZO has relatively poor stability against oxidation. This causes chemical stability issues at cathode|LLZO interface. Computationally predicted oxidation stability limit of LLZO is 2.91 V,[9] which is lower than typical cell voltages vs Li/Li^+ in batteries. LLZO is predicted to decompose into $Li_6Zr_2O_7$, Li_2O_2, La_2O_3 over 2.91 V, and $La_2Zr_2O_6$, Li_2O_2, La_2O_3 over 3.17 V.[9] Li_2O_2 is predicted to further oxidize into O_2 over 3.30 V.[9]

The computational prediction was consistent with experimental findings. Oxidation current appeared over 4.0 V from Cyclic Voltammetry (CV) scan of Li|LLZO|LLZO-C cell, along with decrease of O/Zr elemental ratio.[9] O/Zr elemental ratio decrease originated from oxygen loss from LLZO, which fitted with Density Functional Theory (DFT) predicted degradation pathway. $La_2Zr_2O_7$ formed after 120 h of potentiostatic hold at 4.1~4.3V vs Li/Li^+ at 350 °C.[17] Formation of delithiated phases upon oxidation matched with DFT prediction. Mismatches between voltages for experimentally observed onset of oxidation and computation prediction comes from overpotential.

Table 1 summarizes reaction products of layered oxide cathodes and LLZO predicted by DFT calculation and corresponding energies of reaction.

Table 1 Reaction products and reaction energies for reactions between layered oxide cathodes and LLZO

Reactants	**Products**	**Reaction Energy (meV/atom)**	**Reference**
$LiCoO_2$, LLZO	-	0	Nolan et al.[18]
$LiCoO_2$, LLZO	$Li_6Zr_2O_7$, La_2O_3, Li_5CoO_4	-2	Xiao et al.[19]
$Li_{0.5}CoO_2$, LLZO	O_2, La_2O_3, $LiCoO_2$, $La_2Zr_2O_7$	-21	Nolan et al.[18]
$Li_{0.5}CoO_2$, LLZO	$La_2Zr_2O_7$, $LiCoO_2$, La_2O_3, Li_2CoO_3	-57	Xiao et al.[19]

$LiNi_{1/3}Mn_{1/3}Co_{1/3}O_2$, LLZO	Li_2O, $LiCoO_2$, $Li_6Zr_2O_7$, Li_2NiO_3, NiO, La_2MnCoO_6	-87	Nolan et al.[18]
$LiNi_{1/3}Mn_{1/3}Co_{1/3}O_2$, LLZO	Li_5CoO_4, NiO, La_2O_3, $Li_6Zr_2O_7$, Li_2MnO_3	-1	Xiao et al.[19]
$Li_{0.5}Ni_{1/3}Mn_{1/3}Co_{1/3}O_2$, LLZO	$LiCoO_2$, $Li_6Zr_2O_7$, Li_2NiO_3, Li_2ZrO_3, Li_2O_2, La_2MnCoO_6	-132	Nolan et al.[18]
$Li_{0.5}Ni_{1/3}Mn_{1/3}Co_{1/3}O_2$, LLZO	La_2MnNiO_6, NiO, $LiNiO_2$, Li_2CoO_3, $La_2Zr_2O_7$, Li_2MnO_3	-44	Xiao et al.[19]
$LiNi_{0.6}Mn_{0.2}Co_{0.2}O_2$, LLZO	Li_2O, $Li_6Zr_2O_7$, Li_2NiO_3, NiO, La_2MnCoO_6	-63	Nolan et al.[18]
$Li_{0.5}Ni_{0.6}Mn_{0.2}Co_{0.2}O_2$, LLZO	Li_2NiO_3, Li_2ZrO_3, ZrO_2, NiO, La_2MnCoO_6	-117	Nolan et al.[18]
$LiNi_{0.8}Mn_{0.1}Co_{0.1}O_2$, LLZO	Li_2O, $Li_6Zr_2O_7$, Li_2NiO_3, NiO, La_2MnCoO_6	-38	Nolan et al.[18]
$Li_{0.5}Ni_{0.8}Mn_{0.1}Co_{0.1}O_2$, LLZO	Li_2NiO_3, ZrO_2, NiO, La_2MnCoO_6, $La_2Zr_2O_7$	-80	Nolan et al.[18]

Li rich phases (Li_5CoO_4, Li_2NiO_3, Li_2MnO_3, $Li_6Zr_2O_7$, Li_2ZrO_3, Li_2O, Li_2O_2), Ruddlesden-Popper phases with lanthanum and transition metals (La_2MnNiO_6, La_2MnCoO_6), and delithiated oxides with lanthanum and zirconium (La_2O_3, $La_2Zr_2O_7$) are predicted according to DFT predictions.[18,19] However, these DFT predictions did not consider effect of gas environments on the reaction between layered oxide cathodes and LLZO. Both layered oxide and LLZO reacts with H_2O (g) and CO_2 (g) in air and form LiOH and Li_2CO_3.[20–23] These reactions consume lithium, and inhibit formation of Li-rich DFT predicted phases. DFT calculation including CO_2

as a reactant predicted formation of Li_2CO_3, $La_2Zr_2O_7$, and La_2O_3, even when only 0.0004 CO_2 per LLZO atom were considered.[18] Li_2CO_3 formed as a secondary phase instead of other Li-rich phases when CO_2 was present. The discrepancy between predictions demonstrates importance of gas environment on reaction pathway.

Moreover, delithiation of layered oxide cathodes and LLZO makes them unstable. Layered oxide cathode decomposes into spinel and rock salt phases,[24] and LLZO degrades into Li_2O_2, $Li_6Zr_2O_7$, La_2O_3, $La_2Zr_2O_7$, O_2.[9] Delithiation of layered oxide cathode and LLZO can make the interface between two phases chemically unstable, and drive chemical reaction.

1.3.2. Thermal stability issues at cathode|$Li_7La_3Zr_2O_{12}$ interface

Table 2 summarizes reaction products between layered oxide cathodes and LLZO, and corresponding annealing conditions obtained from experimental works. Dwell time and gas environment were specified if authors provided the information. Products were left blank if the authors did not observe secondary phases formation.

Table 2 Experimentally characterized reaction products for layered oxide cathodes and LLZO after heat treatment

Reactants	**Products**	**Annealing condition**	**Reference**
$LiCoO_2$, LLZO	La_2CoO_4	700 °C, 2 h (Air)	Kim et al.[25]
$LiCoO_2$, LLZO	$LaCoO_3$	900 °C, 10 h (Air)	Ren et al.[26]
$LiNi_{1/3}Mn_{1/3}Co_{1/3}O_2$, LLZO	$La(Co,Mn)O_3$	900 °C, 10 h (Air)	Ren et al.[26]
$LiCoO_2$, LLZO	-	900 °C, 2 h (Air)	Yu et al.[27]
$LiNi_{0.8}Mn_{0.1}Co_{0.1}O_2$, LLZO	La_4NiLiO_8	900 °C, 2 h (Air)	Yu et al.[27]
$LiCoO_2$, LLZO	-	800 °C (Synthetic Air (O_2:N_2 = 21:79 (volume ratio))	Hong et al.[28]
$LiNi_{0.5}Mn_{0.3}Co_{0.2}O_2$, LLZO	Tetragonal LLZO	800 °C (N_2)	Hong et al.[28]
$LiCoO_2$, LLZO	-	800°C, 5 h (Air)	Wakasugi et al.[29]

$LiCoO_2$, LLZO	$LaCoO_3$	1100 °C, 2h	Uhlenbruck et al.[30]
$LiCoO_2$, LLZO	Tetragonal LLZO	700 °C, 1 h (Air)	Park et al.[31]
$LiCoO_2$, LLZO	$La_2Zr_2O_7$	600 °C, 1 h (Air)	Zhang et al.[32]
$LiNi_{1/3}Mn_{1/3}Co_{1/3}O_2$, LLZO	$LaNiO_3$, $La_2Zr_2O_7$	600 °C, 1 h (Air)	Zhang et al.[32]
$LiCoO_2$, LLZO	$LaCoO_3$, $La_2Zr_2O_7$	700 °C, 1 h (Air)	Zhang et al.[32]
$LiNi_{1/3}Mn_{1/3}Co_{1/3}O_2$, LLZO	$LaNiO_3$, $La_2Zr_2O_7$	700 °C, 1 h (Air)	Zhang et al.[32]

Perovskites ($La(Co,Mn)O_3$, $LaCoO_3$, $LaNiO_3$) and Ruddlesden-Popper phases with lanthanum and transition metals (La_2CoO_4), and Li-deficient phase ($La_2Zr_2O_7$) formed in experimental studies,[25,26,30,32] which matched with DFT predictions.[18,19] However, none of the experimental works reported formation of Li rich phases predicted by DFT calculation. In addition, there is no consensus on the secondary phases formed at the interface their onset conditions due to thermal degradation.[25–32]

1.3.3. Electochemical stability issues at cathode|$Li_7La_3Zr_2O_{12}$ interface

Charging makes layered oxide cathode|LLZO interface more unstable compared to discharged state. Reaction energies between half-lithiated layered oxide cathodes and LLZO are lower than fully lithiated layered oxide cathodes and LLZO according to DFT predictions.[18,19]

Despite theoretical prediction of electrochemical degradation at layered oxide cathode|LLZO interface, there has not been an experimental demonstration in a realistic operating condition yet. Hong et al. reported formation of secondary phases from decomposition of $LiNi_{0.5}Mn_{0.3}Co_{0.2}O_2$ and LLZO, as they annealed the cell after charging up to 3.8 V.[28] $La_2Zr_2O_7$, $La_2Li_{0.5}(TM)_{0.5}O_4$ (TM: transition metal), $La(TM)O_3$ (TM: transition metal) formed over 500 °C.[28] From the results, authors proposed Lithium migrate from LLZO to NMC during heat treatment, leading to formation of delithiated phases. The result matches with DFT predicted degradation at layered oxide cathode|LLZO interface.[18,19] However, it is difficult to get fundamental understanding of electrochemical stability from the work since the degradation in the work comes from both electrochemical and thermal instability at the interface. Cell operation at 500 °C is also not a practical condition. In-operando characterization of the cathode|LLZO interface during cycling

or potentiostatic hold under realistic temperature condition is necessary to properly investigate electrochemical stability issues at the interface.

1.3.4. Chemo-mechanical stability issues at cathode|$Li_7La_3Zr_2O_{12}$ interface

Charging causes stress at layered oxide|LLZO interface since lattice parameters of layered oxide cathodes depends on their lithium contents. Crystal structure of $LiNi_{0.6}Mn_{0.2}Co_{0.2}O_2$ (NMC622) cathode changes from H1 to H2 during charging as lithium content changes from $LiNi_{0.6}Mn_{0.2}Co_{0.2}O_2$ to $Li_{0.6}Ni_{0.6}Mn_{0.2}Co_{0.2}O_2$.[33] Lattice parameter changes from a = 2.86 Å, c=14.227 Å (H1) to a = 2.81 Å, c=14.375 Å (H2). Strain energy calculated from lattice parameter changes were higher than fracture energy at both $LiNi_xMn_yCo_{1-x-y}O_2$|LLZO, $LiCoO_2$|LLZO interfaces.[34] The calculation predicts crack formation and delamination at layered oxide cathode|LLZO interface during cycling. Liu et al. identified crack formation at cathode|LLZO interface with Scanning Electron Microscopy (SEM) after cycling $LiCoO_2$|Li_3BO_3-$In_{2(1-x)}Sn_{2x}O_3$|Ta-LLZO|Li cell at 150 °C.[35] The authors correlated this irreversible capacity loss. However, the authors did not discuss effects of intergranular cracks in the cathode particles in the work, potentially due to low magnification used in acquiring SEM image. Intergranular cracks within cathode particles in All-solid-state batteries increases lengths of conduction paths within cathodes and isolate grains from conduction path.[36] Overpotential increases and capacity decreases accordingly. Therefore, analyzing mechanical degradation at both cathode|$Li_7La_3Zr_2O_{12}$ interface and between grains of cathodes is necessary to fully understanding the effect of chemo-mechanical stability issues,

1.4. Overview of the thesis

Following chapters in this thesis discuss stability issues at the interface between layered oxide cathodes ($LiCoO_2$, $LiNi_{0.6}Mn_{0.2}Co_{0.2}O_2$ (NMC622)), and LLZO solid electrolyte. The thesis provides complete understanding on the interfacial degradation at the layered oxide cathode|LLZO interface from the manufacture stage (sintering to gain good contact between cathode and solid electrolyte) to operation stage (electrochemical cycling of the battery). By combining results from experimental techniques and Gibbs Free Energy analysis, we have identified major contributors for degradation in each stage. From the clear understanding of the degradation pathways, we suggested strategies to avoid interfacial degradation.

Following summarizes content of each chapter:

Chapter 2 discusses thermal degradation at NMC622|LLZO interface in air. We have prepared model system consisting thin film NMC622 to study interfacial region between NMC622 and LLZO. Identification of secondary phases (Li_2CO_3, $La_2Zr_2O_7$, $La(Ni,Co)O_3$) and their onset conditions were possible by analyzing experimental results from X-ray Absorption Spectroscopy and X-ray Diffraction. Formation of secondary phases after annealing in air at 700 °C increased the interfacial resistance at NMC622|LLZO interface by two orders of magnitude. Based on the formation of Li_2CO_3 and delithiated phases (La_2ZrO_7, $La(Ni,Co)O_3$), we have hypothesized that presence of CO_2 and delithiation of the interface by formation of Li_2CO_3 is a key contributor driving interfacial instability.

Chapter 3 tests the hypothesis by comparing thermal stability at $LiCoO_2$|LLZO and NMC622|LLZO in different gas environments. We evaluated interfacial instability in O_2, N_2, humidified O_2, and CO_2 gas environments to test detrimental role of H_2O (g) and CO_2. We investigated effect of H_2O (g) and CO_2 as they can both delithiate the interface by forming LiOH and Li_2CO_3 respectively. We did Gibbs Free Energy analysis to evaluate thermodynamic stability in different gas environments. We used model system with thin film cathode discussed in Chapter 2 to characterize phase degradation at the interface. Samples annealed in CO_2 suffered from severe secondary reactions, which fitted with Gibbs Free Energy analysis predicting spontaneous reaction. H_2O was detrimental at low temperature, but the effect could be reversed at high temperature. Avoiding CO_2 and H_2O gave chemically stable interface with lowered interfacial resistance. Notably, using pure O_2 gave interfacial resistance (130 cm^2) comparable to lowest values obtained in previous literatures with interlayer coatings at the interface.

Chapter 4 discusses electrochemical stability at NMC622|LLZO during potentiostatic hold at charging cutoff voltage, and electrochemical cycling. We hypothesized limited oxidation stability of LLZO and the presence of Ni^{4+} in the charged NMC622 will lead to instability at NMC622|LLZO interface. We designed cell for in-operando XAS study on NMC622|LLZO interface. Ni reduced during potentiostatic hold at charging cutoff voltage at room temperature, revealing electrochemical instability at NMC622|LLZO interface at high voltage. In contrast, in-operando XAS for cycling at room temperature did not show formation of reduced phases. Ex-situ XAS for samples cycled at higher temperature (80 °C) revealed formation of reduced phases

with Ni^{2+} and Co^{2+} after cycling. The discrepancy indicates that the secondary reaction at NMC622|LLZO interface could be kinetically limited at low temperature.

Chapter 5 discusses chemo-mechanical stability at NMC622|LLZO interface upon electrochemical cycling. Lattice parameters of NMC622 change during lithiation and delithiation, which causes stress between NMC622 grains and at NMC622|LLZO interface. We identified crack formation between NMC622 grains and at NMC622|LLZO interface from a cycled cell by FIB-SEM. Isolation of NMC622 particles during 1^{st} cycle caused steep decrease in capacity.

Chapter 6 summarizes thermal, electrochemical and chemo-mechanical degradation mechanisms at $LiCoO_2$|LLZO and NMC622|LLZO interface. Outlooks for further experiments based on findings from previous chapters are given.

2. Thermal stability at $LiNi_{0.6}Mn_{0.2}Co_{0.2}O_2$|$Li_7La_3Zr_2O_{12}$ interface in air[1]

2.1. Introduction

As discussed in Chapter 1, computational studies based on first-principles and thermodynamic calculations have predicted interfacial degradation between layered oxide cathodes and LLZO.[10,19] There had been attempts to characterize chemical reactions between layered oxide cathodes and LLZO, but a consensus on the nature of the decomposition products is missing,[25,26,30] and the onset conditions for the degradation remain unexplored. Furthermore, the theoretical predictions of the formation of Li-rich phases such as Li_2NiO_3, Li_5CoO_4, Li_2MnO_3,[10,19] does not match well with experimental findings in literature[25,26,31,32] as well as in recent work[37] from our group and present work. We believe the discrepancy comes from the role of different chemical species and elevated temperatures in the environment, that were not considered in those calculations.

Probing the cathode-solid electrolyte interface is a major challenge. X-ray diffraction on mixed powders is a practical approach to identify reaction phases between solid electrolyte and cathode materials. However, for detecting the secondary phases with good sensitivity using this bulk approach, the reaction has to have proceeded significantly to be within the detection limit of powder XRD. Thus, it misses the ability to detect the onset conditions and identify the effect of very thin reaction zones on the charge transfer kinetics. We have recently addressed this challenge by using thin film cathode layers as model systems, deposited on solid electrolyte pellets.[37] This approach positions the interfacial region within the detection depth of techniques such as X-ray absorption spectroscopy (XAS). This enabled us to capture the initiation of the degradation process at relatively low temperatures, and to precisely characterize the secondary phases and the reacted zone depth (on the order of nm-scale) at the $LiCoO_2$|LLZO interface.[37]

In this research, we have adopted the same thin-film cathode approach as in recent work from our group[37], and have focused on the layered oxide cathode, $LiNi_{0.6}Mn_{0.2}Co_{0.2}O_2$ (NMC622) on LLZO electrolyte. By substituting Co with Ni, it is possible to extract more electrons from the

[1] Reprinted (adapted) with permission from Kim, Y.; Kim, D.; Bliem, R.; Vardar, G.; Waluyo, I.; Hunt, A.; Wright, J. T.; Katsoudas, J. P.; Yildiz, B. Thermally Driven Interfacial Degradation between $Li_7La_3Zr_2O_{12}$ Electrolyte and $LiNi_{0.6}Mn_{0.2}Co_{0.2}O_2$ Cathode. Chem. Mater. 2020, 32 (22), 9531–9541. https://doi.org/10.1021/acs.chemmater.0c02261. Copyright 2020 American Chemical Society.

cathode during charging without triggering oxygen evolution.[38] In addition, Mn incorporation gives additional stability by suppressing Ni^{4+} formation.[39] Using NMC622 could lead to cells with high operating voltage and capacity,[40] and this makes the system more interesting for industrial applications.

Our approach combines synchrotron techniques (X-ray Absorption Near Edge Spectroscopy (XANES), Extended X-ray Absorption Fine Structure (EXAFS)) and lab-based techniques (X-ray Diffraction (XRD), Electrochemical Impedance Spectroscopy (EIS)). XRD enables preliminary phase analysis, but XRD alone is not sufficient to resolve the onset of the degradation where phases have low crystallinity and overlapping peaks. We used XANES and EXAFS to characterize the local chemical and atomic coordination environment, even at relatively low temperatures, where the onset of reactions has taken place but the products have not formed long range order yet. By combining the results obtained from our work and former literature on the instability of layered oxides, we explain the degradation behavior at the NMC622/LLZO interface. Results showed that cation intermixing and oxidation starts at 300 °C, and the effect becomes more severe as temperature rises in air. We found formation and crystallization of Li_2CO_3 starting from 500 °C. At 700 °C, $La(Ni,Co)O_3$ and $La_2Zr_2O_7$ were also detected. We assessed the impact of the chemically degraded interface on the charge transfer properties by performing EIS on symmetric NMC622|LLZO|NMC622 samples. Interfacial resistance increased with annealing temperature, showing that chemical degradation at the interface leads to blockage of Li ion transfer through the interface.

2.2. Experimental design and methods

In order to understand interfacial degradation between NMC622 cathode and LLZO, it is necessary to keep the interfacial region within the detection depth of characterization techniques. In our experiment, XANES experiment using soft X-rays set the upper limit of the thickness of NMC622 thin films that could be used. The thickness was chosen considering the mean free path of photons with 1 keV energy,[41] which is 100nm. Samples were prepared by depositing NMC622 on top of pre-prepared LLZO pellets by RF Sputtering at nominally room temperature conditions.

We bought Al doped LLZO powder from MSESupplies. Al doping concentration was 0.24mol per $Li_7La_3Zr_2O_{12}$. We pressed powder in a pellet form by using 10mm pressing die. We applied 6

Metric Tons for 2min to get a pellet. Pellets were sintered in an alumina crucible. Each pellet was covered by fresh LLZO powder to compensate Li loss and inhibit further Al doping from Alumina crucible. We sintered pellets at 1150°C for 12h in air. After sintering, we polished the pellets using polishing papers. 600 grit, 800 grit, 1000 grit, 1200 grit papers were used in sequence. Pellets were 9mm in diameter, 1mm in thickness after polishing. Pellets were stored in a glove box with Ar environment before sputtering.

NMC622 cathode and gold contact layers were deposited by RF Sputtering. NMC622 target had 10% excess Li to compensate Li loss during sputtering. Both targets were 2 inch in diameter. We polished pellets with 1200 grit polishing papers right before sputtering. Sputtering was done with 100W power. Pressure in the chamber during deposition was 3mTorr. For NMC622 deposition, we introduced argon and oxygen in the sputtering chamber during deposition (Ar: 9sccm, O_2: 3sccm). Au deposition was done in pure Ar environment (Ar: 12sccm) for the EIS samples. Sample stage was rotated during the deposition to ensure uniform deposition. Deposition was done in room temperature.

After deposition of NMC622, the samples were annealed at 300 °C, 500 °C, 700 °C in air for 4 h. We deposited Au after heat treatment at room temperature for EIS characterization. Annealing was done in air in order to consider the possible effect of CO_2 during chemical reaction. Temperature range was chosen to include the range for crystallizing layered oxide cathode thin films after deposition, which spans between 400°C and 700 °C.[42–45]

Chemical and structural characterization was done by XANES, EXAFS, and XRD. We used samples with the same geometry for all the characterization techniques. These characterization techniques complemented each other, and together led to a reliable identification of secondary phases and degradation behavior. XANES and EXAFS give information regarding oxidation state and local chemical and coordination environment of each element. By combining data obtained from those two techniques, and from XRD, we conclude which secondary phases have formed.

Effect of secondary phase formation on charge transfer at the interface was studied by EIS. We used symmetric cells with NMC622 on both sides of the LLZO pellets. This approach let us study the effect of cathode|electrolyte interface only, without a Li|electrolyte interface, and has simplified the analysis. 60 nm thick NMC622 thin film layers were deposited on both sides of

LLZO by RF sputtering. Annealing conditions were the same with the samples that we used for chemical characterization. After heat treatment, 60 nm thick Au layers were deposited on both sides as a current collector.

2.3. Oxidations states of transition metals before and after thermal degradation

The oxidation state and coordination of each element depends on the crystal in which the element resides in. Therefore, depending on the crystal structure of reactants and products, XANES spectra present different features before and after the NMC622|LLZO interface reaction. By analyzing the spectra, we narrowed down the possible set of candidates for the formed secondary phases. We studied the near edge regions of O K-edge, Ni L-edge, La M-edge, Co L-edge, Ni K-edge and Co K-edge.

Figure 1 shows O K-edge spectra for the 100 nm NMC622|LLZO samples, which were annealed at different temperatures. Feature A (528-532 eV) comes from the electronic transition stemming from hybridization of 3d orbitals of transition metals and 2p orbital of oxygen.[46,47] According to former studies on LLZO and Li_2CO_3 including our former work, the change of shape and magnitude of this feature are solely dependent on the chemical environment change of transition metals (Ni, Co, Mn), while O K-edge spectra from LLZO and Li_2CO_3 do not have any features in this energy range.[32,37,48] As seen in Figure 1 (a), magnitude of feature A gradually decreased as annealing temperature increased. This implies loss of transition metal atoms from the detection depth of XAS. This could arise from either diffusion of transition metals through NMC622|LLZO into LLZO and out of the detection depth, or a reaction and phase change involving these elements.

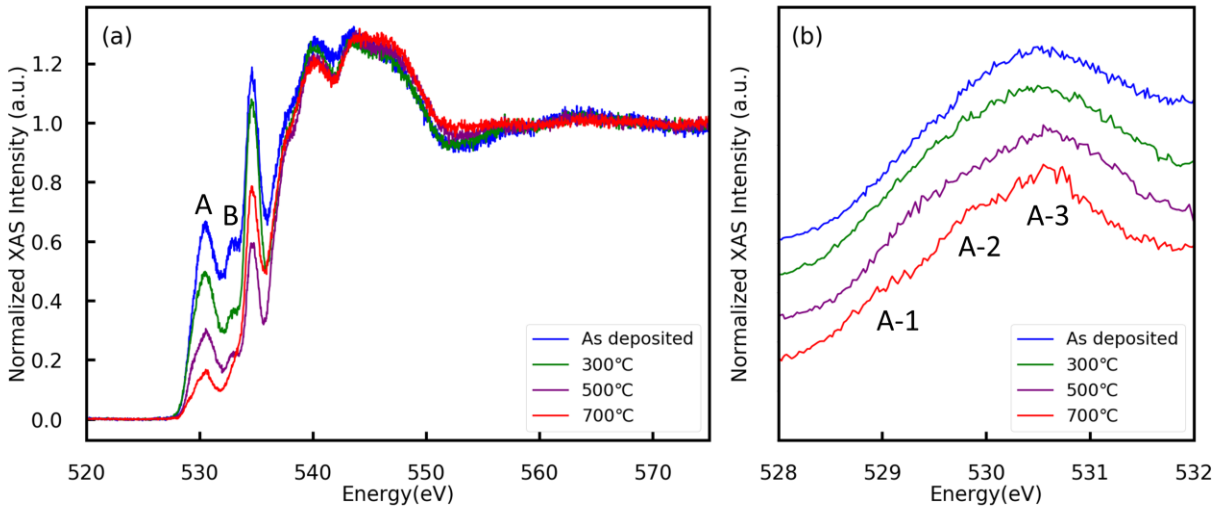

Figure 1 (a) O K-edge X-ray Absorption spectra (Partial Fluorescence Yield mode) for 100 nm NMC622|LLZO in the as deposited state, and annealed at different temperatures in air for 4 h. (b) Region A normalized by highest point in each region. Data shifted by arbitrarily chosen offset for comparison.

Interestingly, the shape of feature A changed when the sample was annealed at 700 °C, as shown in Figure 1 (b), where the intensity is normalized by the magnitude of feature A. The sample annealed at 700 °C shows a low energy shoulder at 529 eV (A-1). This feature has not been reported by other XAS studies on NMC, even when NMC was electrochemically cycled.[49,50] Since this feature appears after exposure to elevated temperature, we believe it is a consequence of a major change in the chemical environment of the transition metals. The meaning of the feature will be further discussed after we present the changes in the Ni and Co $L_{2,3}$-edges.

The loss of interfacial area can be characterized by examining the O K-edge XAS features. The feature B (532eV-533.5eV) in Figure 1 originates from bulk LLZO.[37] Since this Feature B is clearly seen from deposited sample, detection depth of the O K-edge XAS includes all of the NMC622 film and the upper portion of the LLZO pellet. Lack of this Feature B from the sample annealed at 700 °C indicates there is no LLZO left within the same detection depth. LLZO near the NMC interface had been completely transformed to secondary phases. Considering the

geometry of the sample, formed secondary phases completely covered the NMC622|LLZO interface.

Figure 2 (a) shows La M_5 edge, La M_4 edge, Ni L_3 edge, and Ni L_2 edge for each sample. We normalized data by the magnitude of La M_5 edge to compare the data. The M_4 and M_5 edges are evident from the as deposited sample. We attributed the changes in the shape and magnitude of these peaks to interfacial reactions. By comparing the magnitude of the La and Ni edges, we can see a decrease of Ni/La elemental ratio within the detection regime as annealing temperature increased. This implies Ni diffusion into LLZO away from the XAS detection depth, similar to the behavior deduced from Figure 1 above. In addition, Figure 2 (b) indicates that Ni gets more oxidized as annealing temperature increased. In the figure, data for Ni L_2 edge were normalized with the magnitude of low energy portion of the edge for comparison. Spectral weight shift to higher energy is explained by oxidation of Ni.[50–52] These findings together suggest formation of secondary phases including Ni and La at 700 °C. Further justification will be given by the following data.

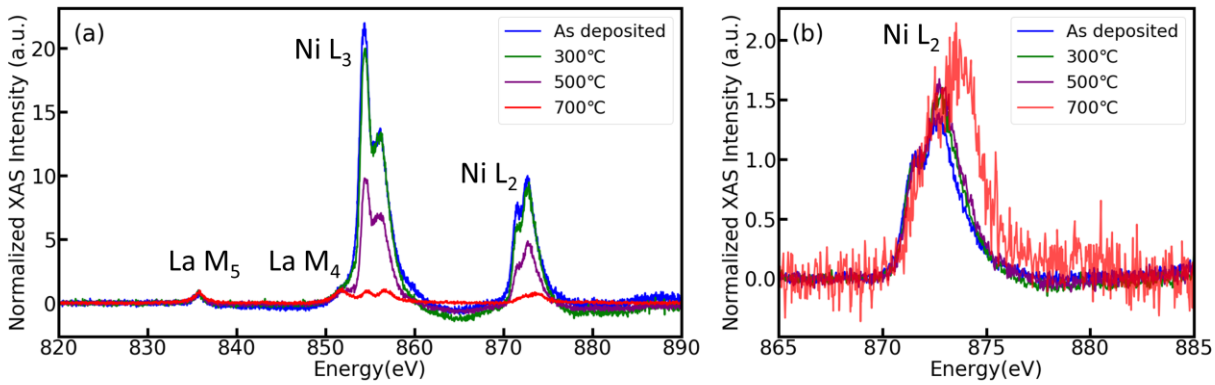

Figure 2 (a) La M_5, La M_4, Ni L_3, Ni L_2 X-ray absorption spectra (partial fluorescence yield mode) for 100 nm NMC622|LLZO in the as deposited state, and annealed at different temperatures in air. Amplitude of peaks normalized by La M_5 peak. (b) Ni L_2 X-ray absorption spectra (Partial Fluorescence Yield mode) for 100 nm NMC622|LLZO in the as deposited state, and annealed at different temperatures in air. Amplitude of peaks normalized by the low energy shoulder peak.

Co L_3 edge shifted toward higher energy, consistent with an increase in the Co oxidation state, as the annealing temperature increased, seen in Figure 3. Interestingly, the shape of Co L_3 edge and Co L_2 edge changed drastically at 700 °C. An increase of the pre-edge feature for Co L_3 edge at 780 eV and spectral weight shift to higher energy for Co L_2 edge are evident. Merz et al. reported these features from their study on doped $LaCoO_3$ perovskites.[53] The authors compared Co L-edge shape for $LaCoO_3$, $La_{0.7}Ce_{0.3}CoO_3$, and $La_{0.7}Sr_{0.3}CoO_3$, and found these features (the same as our Co $L_{2,3}$ edge spectrum at 700 °C) for Co^{4+}(high spin, HS) in $La_{0.7}Sr_{0.3}CoO_3$. Notably, undoped $LaCoO_3$ did not show features for Co^{4+}(HS) in their study.

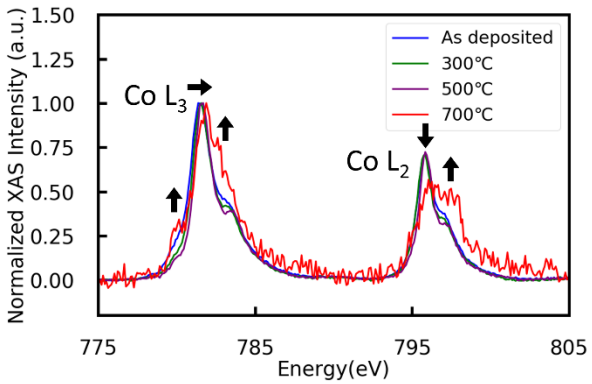

Figure 3 Co L_3, Co L_2 X-ray absorption spectra (partial fluorescence yield mode) for 100 nm NMC622|LLZO in the as deposited state, and annealed at different temperatures in air. Amplitude of peaks normalized by the Co L_3 edge.

In our previous work on the $LiCoO_2$|LLZO interface, formation of $LaCoO_3$ was a reaction product upon annealing.[37] Therefore, it is reasonable to assume the formation of similar perovskite phases at the NMC622|LLZO system, as we substituted elements of the cathode layer without changing crystal structure. However, formation of pure $LaCoO_3$ cannot explain the features in Co L-edge shown Figure 3. For this reason, we propose that the secondary phase formed at 700 °C is a doped $LaCoO_3$. Considering the evidence of Ni/La intermixing found from Figure 2, we suggest that Ni is the likely dopant in the $LaCoO_3$ formed here. Introducing Ni into $LaCoO_3$ as a B-site dopant increases Co^{4+}(HS) content, as reported by Huang et al.[54] Co L-edge edge shape change shown in Huang et al.'s data match well with the work of Merz et al.

mentioned above,[53] and with Figure 3 shown in this work. Therefore, we can conclude that the Co oxidation state increases and becomes 4+ (HS) after annealing the interface to 700°C.

Oxidization of Ni above +2 at 700 °C, shown in Figure 2 (b), requires that Ni concentration in $La(Ni,Co)O_3$ is higher than Co. If we denote the concentration of Ni as x in $LaNi_xCo_{1-x}O_3$ ($0.5 \leq x \leq 1$), we can rewrite the charge neutrality formula as $(La^{3+})(Ni^{2+})_{1-x}(Ni^{3+})_{2x-1}(Co^{4+})_{1-x}(O^{2-})_3$ according to Pérez's model.[55] In this formula the average oxidation state of Ni is 4-1/x, and it increases from +2 to +3 as Ni concentration increases from 0.5 to 1 in $La(Ni,Co)O_3$. Pérez's model also states that oxidation state of Ni is fixed to +2 for $LaNi_xCo_{1-x}O_3$ with $x \leq 0.5$. So, an increase of oxidation state of Ni above 2+ (as seen from Ni L_2-edge in Figure 2 (b)) means $x > 0.5$ in $LaNi_xCo_{1-x}O_3$. Assuming that the reaction front is at the buried interface between the LLZO and NMC, this argument is consistent with the Ni migration out of NMC622 (as seen from the decrease of Ni L_2/La M_5 ratio at 700 °C in Figure 2 (a)), presumably occurring during $La(Ni,Co)O_3$ formation.

Going back to Figure 1, increased oxidation of Co upon heat-treatment is seen further by analyzing the O K-edge carefully. The feature A-1 shown in Figure 1 (b) is seen in materials in which Co is octahedrally coordinated by oxygen ligand with holes.[56,57] Miyoshi and Yamaguchi[56] found that the feature A-1 became larger for $La_{0.6}Sr_{0.4}CoO_{3-\delta}$ as the oxygen partial pressure of the environment increased. In addition, Karvonen et al. showed that feature A-1 became larger as oxygen concentration increased in $SrCoO_{3-\delta}$.[57] Oxygen concentration increase leads to oxidation of transition metal in those system. Therefore, these works give further proof to the A-1 feature indicating further oxidation of Co.

The near edge regions of the Ni K-edge and Co K-edge spectra, shown in Figure 4, provide further support for the oxidation of Ni and Co. Data were obtained in fluorescence yield mode. We defined the edge by taking the energy at which the normalized absorption value was 0.5.[58] Both edges shift to higher energy as the annealing temperature increased, showing further oxidation of both Ni and Co.

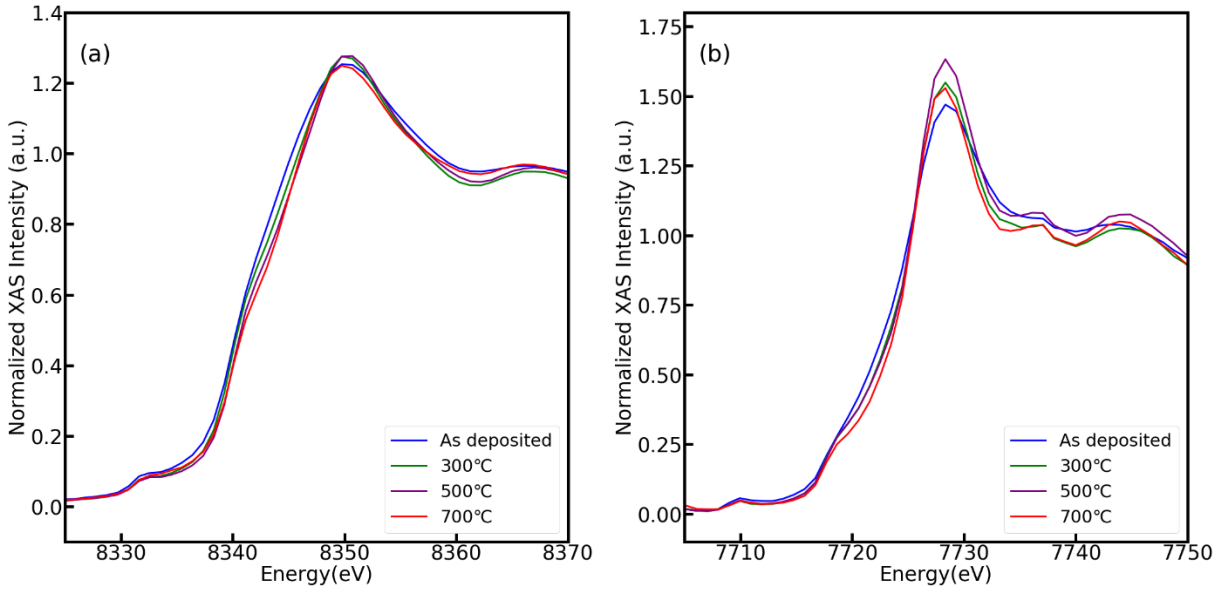

Figure 4 Ni K-edge, and (b) Co K-edge X-ray absorption spectra (fluorescence yield mode) for 100 nm NMC622|LLZO in the as deposited state, and annealed at different temperatures in air.

Figure 5 shows Mn L-edge spectra for the as-deposited sample, and for samples annealed at 300 °C, 500 °C, 700 °C. All data showed features for Mn^{4+}, but did not show features corresponding to Mn with other oxidation states (Mn^{2+}, Mn^{3+}).[59] Therefore, oxidation state of Mn remained the same before and after heat treatment.

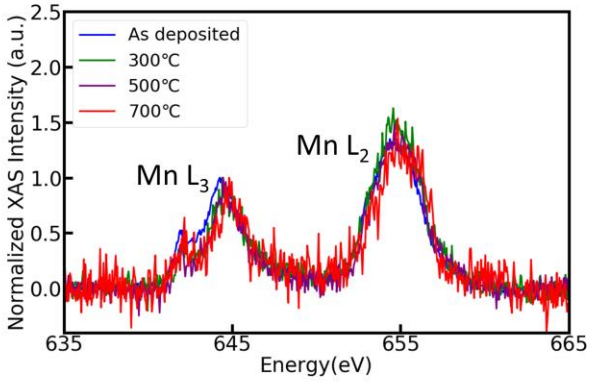

Figure 5 Mn L_3, Mn L_2 X-ray Absorption spectra (Partial Fluorescence Yield mode) for 100 nm NMC622|LLZO in the as deposited state, and annealed at different temperatures in air. Amplitude of peaks normalized by Mn L_3 edge.

2.3. Local chemical environment of elements due to secondary phase formation

Above we have deduced evidence for migration of Ni and Co out of NMC622 and formation of $La(Ni,Co)O_3$. Thus, we expect changes in the atomic coordination of these elements and examine the Ni K-edge and Co K-edge EXAFS. Figure 6 (a) and (b) shows Ni K-edge and Co K-edge EXAFS in R-space. Figure 6 (c) and (d) shows ideal scattering paths for Ni and Co in layered oxides ($LiNiO_2$, $LiCoO_2$) and in perovskites ($LaNiO_3$, $LaCoO_3$). The scattering paths are plotted for the 1st, 2nd, and 3rd shells for layered oxides, and the 1st and 2nd shells for perovskites.

As seen in the Figure 6 (c) and (d), $LaNiO_3$, $LaCoO_3$ shows almost identical scattering paths around Ni and Co respectively. This originates from the same crystal symmetry. Therefore, scattering paths obtained for Ni in $LaNiO_3$ and Co in $LaCoO_3$ could be used to model scattering path in $La(Ni,Co)O_3$. Same logic justifies using $LiNiO_2$ and $LiCoO_2$ to model the scattering path in NMC 622.

Magnitudes of feature A and feature B increase up to 500 °C for both Ni K-edge and Co K-edge. This shows crystallization of the sputtered NMC films because the feature A and B are related to first shell and second shell of layered oxide structure respectively.[60–62] This crystallization trend was also reported by our former study on annealing of $LiCoO_2$ thin film|LLZO system.[37] However, Ni K-edge EXAFS deviated from this trend at 700 °C. Magnitude of feature B dropped in comparison to the sample annealed at 500 °C, while magnitude of feature A remained almost the same. Moreover, magnitude of feature C increased compared to other temperature conditions.

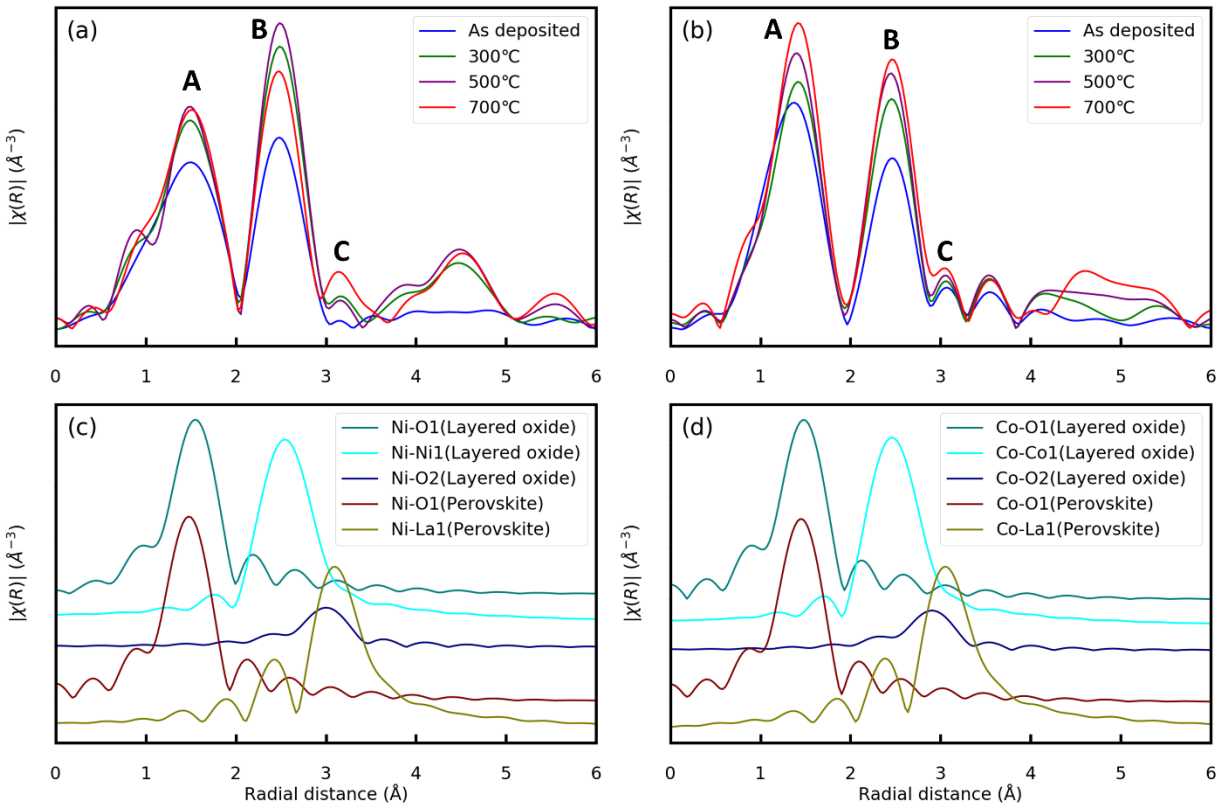

Figure 6 (a) Ni K-edge (b) Co K-edge EXAFS data in real space. (c) Single scattering paths for $LiNiO_2$ (mp-25592) and $LaNiO_3$ (mp-1075921). (d) Single scattering paths for $LiCoO_2$ (mp-24850) and $LaCoO_3$ (mp-1068396). (Numbers after mp indicate the identity for each crystal structure in the Materials Project Database[63])

Simultaneous increase of feature C and decrease of feature B at 700 °C can be explained by formation of $La(Ni,Co)O_3$ phase. Figure 6 (a) and (c) show that the scattering paths from the second shell of NMC622 mainly contributes to feature B of the Ni K-edge EXAFS. Therefore, Ni migrating out of NMC622 to form the perovskite phase leads to the decrease of feature B. Moreover, we can see that the second shell of $La(Ni,Co)O_3$ has a major contribution to feature C. Therefore, formation of the perovskite phase increases the feature C intensity. We also note that the first shells of both $La(Ni,Co)O_3$ and of NMC622 contribute to feature A. Therefore, decomposition of NMC622 and formation of $La(Ni,Co)O_3$ would not change the feature A, consistent with the lack of any change in feature A of the Ni K-edge in Figure 6 (a).

The behavior at 700 °C cannot be explained by only the crystallization of the NMC film. Feature C also has a contribution from the third shell of NMC622 as shown in Figure 6 (c). Therefore, if NMC622 is the only phase present, Feature C increase along with feature B decrease would indicate that crystallinity of the third shell of NMC622 increases while the second shell loses crystallinity. This is contradictory to increased crystallization.

In contrast to the major changes in Ni K-edge EXAFS, there is only a gradual increase of features A, B, and C of the Co K-edge EXAFS with increasing annealing temperature. This trend shown in Figure 6 (b) can be explained by increased crystallization of sputtered NMC622 films, without the need of another phase to explain the data. This shows that effect of chemical environment change around Co due to formation of $La(Ni,Co)O_3$ is overwhelmed by crystallization of sputtered NMC622 film. Therefore, we claim that Co does not participate as much as Ni in perovskite formation. This is consistent with our conclusion above, based on oxidation states that, Ni concentration in $La(Ni,Co)O_3$ is higher than Co.

2.4. Structural characterization of secondary phases

XRD was done to verify the formation of $La(Ni,Co)O_3$ and identify other secondary phases that formed due to annealing (Figure 7 (a)).

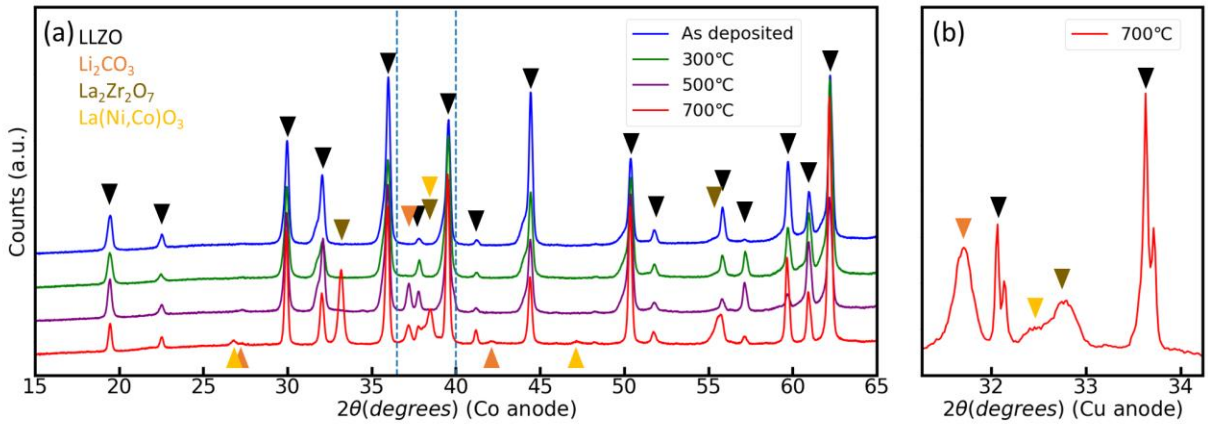

Figure 7 (a) 1D XRD pattern obtained using Co anode for the 100 nm NMC622|LLZO in the as deposited state, and annealed at different temperatures in air. (b) 1D XRD pattern (the same region marked with dashed lines in (a)), measured using Cu anode, for the 100 nm NMC622|LLZO annealed at 700 °C in air.

All samples showed peaks corresponding to bulk LLZO grains (ICDD:00-063-0174). The as-deposited sample and the sample annealed at 300 °C did not show peaks for secondary phases. In contrast, samples annealed at 500 °C and 700 °C showed peaks for Li_2CO_3 (ICDD: 00-022-1141) in addition to LLZO. For the sample annealed at 700 °C (Figure S5), we also identified peaks for $La_2Zr_2O_7$ (ICDD:01-070-5602). Peaks for (222) plane (33.3˚ [Co anode]), (400) plane (38.7˚ [Co anode]), and (440) plane (55.9˚ [Co anode]) were clearly seen.

We also expected peaks corresponding to $La(Ni,Co)O_3$ from the sample annealed at 700 °C considering the XANES and EXAFS results. We observed peaks at 27.0° and 47.4° corresponding to (012) and (202) planes of $LaNi_{0.5}Co_{0.5}O_3$ reference spectra (ICDD:00-054-0834), respectively. In order to give further proofs for the perovskite phase formation, we used Panalytical X'Pert Pro for a detailed scan. The result is shown in Figure 7 (b). Detailed scan was done within the angle range (A) shown on Figure 7 (a) and Figure S5 for the sample annealed at 700 °C. The angle range was chosen so that it includes the highest intensity peak for the perovskite phase. In Figure 7 (b), LLZO peaks show sharp doublets due to Cu $K\alpha_1$ and Cu $K\alpha_2$ radiation. Li_2CO_3 (002) (31.8˚ [Cu anode]) and $La_2Zr_2O_7$ (400) (33.2˚ [Cu anode]) are clearly identifiable. In addition, an additional small peak is present just before the $La_2Zr_2O_7$ (400) peak. This peak could not be resolved using Bruker GADDS due to its limited resolution. This peak fits with the (110) plane of $LaNi_{0.5}Co_{0.5}O_3$ reference spectra (ICDD:00-054-0834) (32.75˚ [Cu anode]), which is the strongest peak of the perovskite structure. This provides clear evidence for the formation of $La(Ni,Co)O_3$. Crystallite size of $La(Ni,Co)O_3$ was calculated using FWHM of XRD peak corresponding to (110) plane using the Scherrer equation.[64] Crystallite size of $La(Ni,Co)O_3$ was found to be 27 nm. However, this value does not necessarily correspond to the reaction layer thickness, as the reaction layer can consist of more than one crystal size of depth.

EXAFS data (Figure 6) shows the increase of short-range order in NMC622 film after annealing. Intensity of the features corresponding to both Ni-O bond (1st shell) (Figure 6 (a)) and Co-O bond (1st shell) (Figure 6 (b)) increased as annealing temperature increased. However, XRD peaks corresponding to the NMC phase could not be detected by using the Bragg-Brentano geometry. We attribute this to the reaction between NMC622 and LLZO, leading to only a small amount of NMC622 left in the system. Because of this, XRD with Bragg-Brentano geometry was

not sensitive enough to the NMC phase, even when EXFAS analysis showed increase of short-range order in NMC. Signal from bulk LLZO pellet and from the formed secondary phases overwhelmed the signals from the remaining NMC622 in the system. In order to confirm the increased crystallinity of NMC, we performed grazing incidence XRD using Rigaku Smartlab. Figure S6 shows grazing incidence XRD data for the sample annealed at 700 °C in air. A broad peak at 18.7° [Cu anode] corresponds to the XRD peak from the (003) plane of NMC622 (ICDD: 00-066-0854). Formation of a broad peak for (003) plane has been also reported by previous woks on RF deposited $LiCoO_2$ films.[65,66] In addition, the peak strength for (003) plane increased as the incident angle decreased from 2° to 1°. This further justifies that the peak originated from NMC622, which had crystallized on top of the LLZO pellet. We could also observe a peak which could potentially come from the (104) plane of NMC622 (44.4° [Cu anode]). However, peak assignment was difficult to confirm due to a nearby peak from LLZO (620) plane (44.0° [Cu anode]).

2.5. Effect of the degradation on interfacial resistance

Electrochemical impedance spectroscopy allowed to quantify the impact of the interfacial chemical degradation on the electrochemical charge transfer properties. The samples were Au|NMC622|LLZO|NMC622|Au symmetric cells, with 60nm thick NMC622 thin film layers on both sides of polished LLZO pellets. Au was deposited as a current collector after samples were prepared and annealed in air.

Figure 8 shows the EIS data for samples with different annealing conditions. In Figure 8 (a)-(d), EIS data are shown in a narrower frequency range compared to Figure 8 (e)-(h), so that the small arcs at higher frequencies are discernable.

We used two different equivalent circuit models to analyze the EIS data. For the as-deposited sample and the sample annealed at 300 °C, we used $(R_{bulk}C_{bulk})(R_{interface1}CPE_{interface1})(CPE_{tail})(L)$ circuit since there were two semicircles. On the other hand, we used $(R_{bulk}C_{bulk})(R_{interface1}CPE_{interface1})(R_{interface2}CPE_{interface2})(CPE_{tail})(L)$ circuit for samples annealed at 500 °C and 700 °C as there were three apparent semicircles in the plot. Serially connected inductor comes from the wiring of the setting. This element has been used by works using LLZO pellets and improved fitting the data at the high frequency range.[67,68] Serially connected constant phase element corresponds to the low frequency tail shown in Figure 8.

We observed the high frequency semicircle ($R_{bulk}C_{bulk}$) around 2.5 MHz in all samples. This comes from the geometry of the LLZO pellet. The conductivity and relative permittivity deduced from this arc are 2.7×10^{-1}mS/cm and ~80, respectively, consistent with values reported in former works on LLZO.[68,69]

We also identified additional arcs at 4 kHz ($R_{interface1}CPE_{interface1}$) in all samples as seen in Figure 8. We attribute this feature to the NMC622|LLZO charge transfer resistance. The feature in the similar frequency range was also attributed to the interface charge transfer resistance in our former work on the $LiCoO_2$|LLZO.[37] In addition, a new arc arises around 40 kHz ($R_{interface2}CPE_{interface2}$) for the samples annealed at 500 °C and 700 °C. We confirmed with XRD that sample annealed at 500 °C had Li_2CO_3, and sample annealed at 700 °C had Li_2CO_3, La(Ni,Co)O_3 and $La_2Zr_2O_7$ as secondary phases. Based on those findings, we attribute this feature around 40 kHz to the impedances arising from secondary phases.

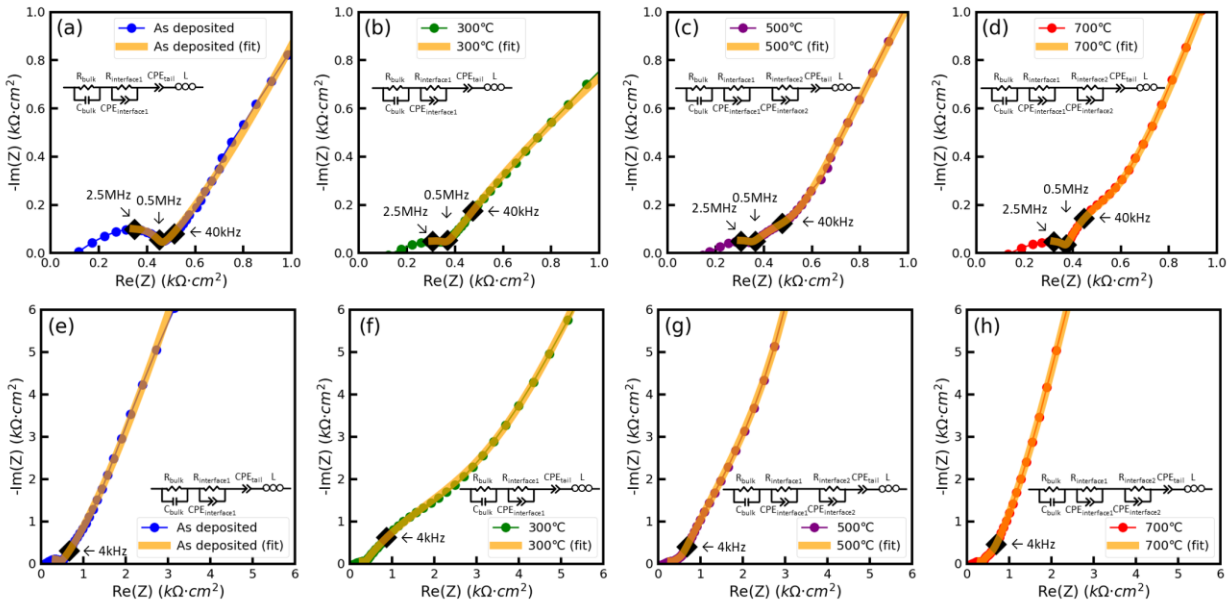

Figure 8 Electrochemical impedance spectroscopy (EIS) data for Au|NMC622|LLZO|NMC622|Au symmetric cells. (a)-(d): EIS data for frequency range where the impedance is less than 1.0kΩ·cm^2 are plotted. Data for (a) As deposited (7.94MHz-794Hz), and samples annealed at (b) 300 °C (6.31MHz-3.16kHz), (c) 500 °C (6.31MHz-1.26kHz), (d) 700 °C (6.31MHz-1.58kHz) in air for 4h are shown. (e)-(h): EIS data for the frequency range where the impedance is less than 6.0kΩ·cm^2 are plotted. Data for (e) As deposited (7.94MHz-

63.1Hz), and samples annealed at (f) 300 °C (6.31MHz-39.8Hz), (g) 500 °C (6.31MHz-100Hz), (h) 700 °C (6.31MHz-158Hz) in air for 4h are shown.

Figure 9 shows comparison of cathode|electrolyte interfacial resistance for each sample. As we used symmetrically constructed sample, effect of the interfacial resistance is twice as large compared to the cell with only one cathode|electrolyte interface. In order to get interfacial resistance through single cathode|electrolyte interface, Figure 9 plots the $R_{interface}/2$ for cathode|electrolyte interfacial resistance for the as deposited sample and the sample annealed at 300 °C, and the $(R_{interface1}+R_{interface2})/2$ for the samples annealed at 500 °C and 700 °C.

As seen in Figure 9, the Area Specific Resistance (ASR) increases with annealing temperature. Obtained ASR arising from the interface or from the interface reactions, for as deposited, 300 °C, 500 °C treated samples are 1.4kΩ·cm^2, 1.7kΩ·cm^2, 2.1kΩ·cm^2 respectively. Notably, ASR increases dramatically to 102kΩ·cm^2 when the sample was annealed at 700 °C. This fits well with the findings from XANES, EXAFS, and XRD that, major interfacial chemical and structural degradation takes place by 700 °C. Formation of phases that do not conduct Li ions, such as $La_2Zr_2O_7$, $La(Ni,Co)O_3$, Li_2CO_3 are expected to increase the ASR at the interface.[37]

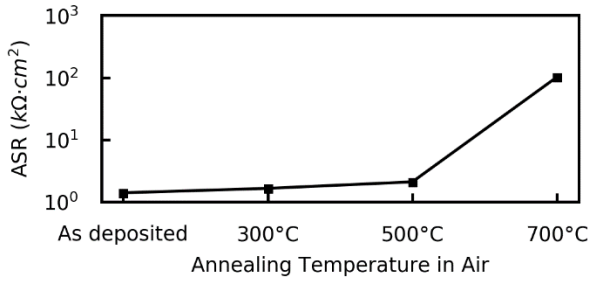

Figure 9 Area Specific Resistance (ASR) for a single cathode|electrolyte interface from the as deposited NMC622|LLZO, and after annealing at different temperatures for 4h in air.

2.5. Discussion

The first key point we discuss is that, the secondary phases formed due to the interfacial degradation ($La_2Zr_2O_7$, $La(Ni,Co)O_3$ and Li_2CO_3) are not Li conductors. $La_2Zr_2O_7$ has poor Li conductivity, and it is a typical secondary phase found in delithiated LLZO.[70] $La(Ni,Co)O_3$ is not expected to be a Li-conductor. There are perovskite Li-conductors such as $(Li,La)TiO_3$, but Li

conduction requires substantial A-site vacancy fraction.[71] Li_2CO_3 has much poorer Li conductivity (~10^{-3}mS/cm) at room temperature compared to LLZO.[72]

There is a large difference in interfacial resistances of the sample that only contains Li_2CO_3 after exposure to 500 °C, and that of the sample that contains Li_2CO_3, $La_2Zr_2O_7$ and $La(Ni,Co)O_3$ after exposure to 700 °C. Interfacial resistance found from the former was 2.1 kΩ·cm^2 and that from the latter was 102 kΩ·cm^2. This proves that formation of interfacial products ($La_2Zr_2O_7$ and $La(Ni,Co)O_3$) beyond Li_2CO_3 led to a substantial degradation of the charge transfer properties of the interface. This explains the stark increase of interfacial resistance for the sample annealed at 700 °C. Complete coverage of the interface with secondary phases (Li_2CO_3, $La_2Zr_2O_7$, $La(Ni,Co)O_3$ which are poor Li conductors) led to poor Li transfer at the interface, with two orders of magnitude increase in the interface impedance.

The second key point is that, Ni has higher tendency than Co to participate in the formation of $La(Ni,Co)O_3$, as deduced from the Ni K-edge and Co K-edge EXAFS data taken from sample annealed at 700 °C. The features for $La(Ni,Co)O_3$ in the Ni K-edge EXAFS spectra indicates that substantial amount of Ni experienced a chemical environment change. In contrast, Co K-edge EXAFS spectra could be fully explained by crystallization of the NMC film. Therefore, only small portion of Co in NMC622 film participated in perovskite formation and majority of those remained in NMC622.

Different reaction tendencies of transition metal cations can originate in part from their mobility in NMC lattice. With this, we mean two processes: i) move of the transition metal to the Li sites, and ii) the migration of the transition metal once it resides at the Li sub-lattice. Migration of transition metal cations to the nearby octahedral site of the Li sub-lattice makes them mobile in the oxide.[73] Ni is able to move to the Li sites more readily than Co and Mn in NMC because the energy needed for Li^+/Ni^{2+} exchange is lower than Li^+/Co^{3+} or Li^+/Mn^{4+} exchange. Calculated formation energy for the Ni_{Li}-Li_{Ni}, Co_{Li}-Li_{Co}, Mn_{Li}-Li_{Mn} antisite pairs in $LiNi_{1/3}Co_{1/3}Mn_{1/3}O_2$ are 0.57eV, 1.42eV, 2.60eV respectively.[74] Moreover, Ni has low migration barrier, ~0.25eV, once it migrates into Li site by Li^+/Ni^{2+} exchange.[75] This value is on the same order of migration barrier of Li in layered oxide cathodes.[75–78] Solid state reaction between two phases in contact requires flux of elements toward the interface. As Ni is the most mobile transition metal species in NMC lattice, Ni flux will be larger than Co and Mn. For this reason, if there is an external

chemical driver for reaction, we expect Ni will more readily migrate to the interface and participate in the reaction.

The result suggests that increasing Ni content in the layered oxide to obtain a high power and high capacity cell can lead to inferior interfacial instability. Ni rich cathode is already well-known to react with organic electrolyte and form SEI.[79] Our work is the first experimental demonstration that the same problem exists in this all solid system, too.

EXAFS analysis for Mn coordination was not possible due to overlap of La L1-edge and Mn K-edge, but XRD and oxidation state analysis indicated no detectable reactivity of Mn in our system. There weren't any Mn containing secondary phases detected using XRD. Oxidation state of Mn did not change after annealing as seen by Mn L-edge spectra (Figure S1). Therefore, we conclude that Mn is not participating in the secondary phase formation between LLZO and NMC622 in our experimental conditions.

The third key point we discuss here, is the inconsistency between prior computational predictions of NMC|LLZO interfacial reactions and our experimental findings. We propose that this is because of not having considered the elevated temperature and gas environment effects. Xiao et al., predicted Li_5CoO_4, NiO, La_2O_3, $Li_6Zr_2O_7$, Li_2MnO_3 formation for reaction between NMC and LLZO.[19] Richards et al., predicted $La_2Zr_2O_7$, Li_2NiO_3, La_2O_3 for $LiNiO_2$|LLZO, and $La_2Zr_2O_7$, Li_2MnO_3, La_2O_3 for $LiMnO_2$|LLZO.[10] Both works do not predict formation of $La(Ni,Co)O_3$ phase, and we did not find evidence to La_2O_3 or to Li-rich transition metal oxides. Most importantly, the pervasive Li_2CO_3 formation in our experimental findings is missing from previous theoretical reports. The discrepancy between our experimental results and prior calculations could arise from two key factors. First, the computational predictions we see in literature[19,10] have not considered the potential role of gaseous species in the environment, in particular CO_2 and $H_2O_{(g)}$. We find substantial Li_2CO_3 formation as a sink of Li, consumed by CO_2. As a result, this process is not permitting the formation of the predicted lithium rich phases such as Li_5CoO_4, Li_2NiO_3, Li_2MnO_3. Li_2CO_3 is also responsible for the formation of delithiated phases. These are $La_2Zr_2O_7$ that precipitate from LLZO, and $La(Ni,Co)O_3$ that can form as a reaction product when LLZO and NMC are delithiated and become more unstable. As neither NMC622 nor LLZO contains carbon, reaction requires substantial carbon influx from outside the sample to proceed. Since we annealed the sample in air, CO_2 is the carbon source. This shows

the importance of the gas environment in the interfacial degradation. Based on this, we argue that controlling the gas environment, especially P_{CO_2} during the synthesis of these interfaces is important in achieving better stability.

Another reason behind the seeming discrepancy is likely the effect of entropy, which becomes important at higher temperatures. Both Xiao et al., and Richards et al., calculated energies for phases which are in ground state or in equilibrium at a certain composition, and used those to find the reaction giving largest driving force.[10,19] However, as Xiao et al., noted in their work, this approach could underestimate the effect of configurational entropy at elevated temperatures.[80]

The results presented in this chapter prompt us to hypothesize that CO_2 is the major contributor for interfacial degradation between NMC622 and LLZO at elevated temperature. Li_2CO_3 forms by reacting with CO_2 in ambient air. This reaction reduces the Li content in NMC and in LLZO, rendering them less stable. As a result, delithiated phases, $La(Ni,Co)O_3$ and $La_2Zr_2O_7$, form between NMC and LLZO. This hypothesis warrants more work to probe the NMC|LLZO interface after subjecting it to different gas conditions, and that is the topic of the next chapter (Chapter 3) of this thesis.

2.6. Conclusion

In this chapter, we revealed products of interfacial reactions at NMC622|LLZO during annealing, starting with onset temperatures as low as 500 °C in air. This was possible by using thin film cathodes within the detection depth of near-surface sensitive techniques, and by combining findings from synchrotron based XANES and EXAFS with lab-based XRD. Major decomposition products, Li_2CO_3, $La_2Zr_2O_7$, and $La(Ni,Co)O_3$, were found in the sample annealed at 700 °C. In contrast, such phases were not present in the sample annealed at 300 °C, and only Li_2CO_3 was present in the sample annealed at 500 °C. Identification of $La(Ni,Co)O_3$, with substantial Ni content, was possible by careful analysis of XANES and EXAFS data. Ni was found to be more reactive than Co in forming this secondary phase at the LLZO interface. Importantly, the formed secondary phases are detrimental to the electrochemical properties. Area specific resistance at the cathode|electrolyte interface increased by two orders of magnitude after annealing up to 700 °C compared to the as-prepared NMC622|LLZO. Based on these results, we can conclude that using low temperature processing is necessary to avoid detrimental secondary

phase formation if the production is done in air. Considering the reactants and products of the degrading reaction, we hypothesize that CO_2 is the major contributor for interfacial degradation between NMC622 and LLZO at elevated temperature, and we suggest using a gas environment that doesn't contain CO_2 to minimize interfacial degradation. Effect of gas environments on interfacial degradation will be further explored in the next chapter (Chapter 3).

3. Effect of gas environment on thermal stability at $LiCoO_2|Li_7La_3Zr_2O_{12}$ and $LiNi_{0.6}Mn_{0.2}Co_{0.2}O_2|Li_7La_3Zr_2O_{12}$ interfaces[2]

3.1. Introduction

In the previous chapter (Chapter 2), we have indicated the importance of the importance of the gas environment on the thermal stability of LLZO in contact with layered oxide cathode materials.[37,81] Li_2CO_3, $LaCoO_3$, $La_2Zr_2O_7$ formed at the $LiCoO_2$|LLZO interface,[37] and Li_2CO_3, $La(Ni,Co)O_3$, $La_2Zr_2O_7$ formed at $LiNi_{0.6}Mn_{0.2}Co_{0.2}O_2$(NMC622)|LLZO[81] when these interfaces were annealed in air from 300 °C to 700 °C. Computational predictions, on the other hand, predicted the formation of Li-rich phases (Li_2NiO_3, Li_5CoO_4, Li_2MnO_3).[10,19] In particular the presence of Li_2CO_3 as a reaction product prompted us to hypothesize that CO_2 favors the formation of Li_2CO_3, and this leads to delithiating the LLZO, LCO and NMC622, rendering these phases more unstable and more likely to react with each other, resulting in the formation of Li-deficient secondary phases. This warrants new experiments and calculations considering the gas environment explicitly when evaluating the stability of layered oxide cathode|LLZO interfaces, as we present in this chapter.

It is well known that both bulk LLZO and layered oxide cathodes degrade by losing Li as they react with H_2O(g) and CO_2(g). LLZO degrades by forming LiOH and Li_2CO_3 near the surface under H_2O and CO_2 gas environment.[22,23] Layered oxide cathodes, especially the ones with high Ni content, also have similar stability issues with H_2O and CO_2.[20,21] Both LLZO and layered oxide cathodes become unstable by losing Li. LLZO decomposes into Li_2O_2, $Li_6Zr_2O_7$, La_2O_3, $La_2Zr_2O_7$, O_2 upon delithiation.[9] Delithiated layered oxide cathodes transform to spinel and rock salt phases by losing oxygen.[24] Such instabilities due to Li-loss from LLZO and/or the layered oxide cathode can aggravate the thermodynamic instability between these phases at elevated temperatures. This is consistent also with the theoretical prediction that the reaction between

[2] Reprinted (adapted) with permission from Kim, Y.; Waluyo, I.; Hunt, A.; Yildiz, B. Avoiding CO_2 Improves Thermal Stability at the Interface of $Li_7La_3Zr_2O_{12}$ Electrolyte with Layered Oxide Cathodes. Advanced Energy Materials 2022, 12 (13), 2102741. https://doi.org/10.1002/aenm.202102741.

delithiated LCO and LLZO is thermodynamically more favorable compared to the reaction between fully lithiated LCO and LLZO.[82]

Based on our earlier findings[37,81], and the known detrimental role of H_2O(g) and CO_2(g) in destabilizing LLZO and layered oxide cathodes,[20,22,23] we believe it is important to assess the role of the gas environment in the stability of cathode|LLZO interfaces. In this work, we test this hypothesis by simple thermodynamic calculations and by model thin-film experiments with controlled gas environments. We used NMC622, which is a promising high voltage layered oxide cathode for experimental characterization. We used $LiCoO_2$ for thermodynamic calculations to predict and interpret qualitatively the reactivity between LLZO and a layered oxide cathode. LCO is simpler than NMC622 in deducing the reaction pathways and products, but yet representative given the presence of Co as a transition metal. We chose O_2, N_2, humidified O_2, and CO_2 gas environments to isolate their effect on the interfacial stability, as these constitute majority of gas species in air. Humidified O_2 and CO_2 environment were chosen to study the effect of H_2O(g) and CO_2(g) on interfacial degradation. O_2 and N_2 environments were control groups which don't contain H_2O(g) and CO_2(g).

Model systems comprising thin film cathode layers on LLZO pellets present advantages for studying interfacial degradation as demonstrated in our previous works.[37,81] The buried interface region of such thin films (≤100 nm) is within the detection depth of near-surface sensitive techniques such as soft X-ray absorption spectroscopy (XAS) using fluorescence yield detection mode. This allows us to detect the onset temperature of degradation and identify the phases without relying on destructive techniques such as transmission electron microscopy. Moreover, as XAS is sensitive to the oxidation state and local chemical environment, we could identify the onset of chemical reactions even when the formed phases had low crystallinity, unlike X-ray diffraction on bulk powder samples whose sensitivity needs a large fraction of the sample to have degraded and formed high crystallinity.

Precise characterization of phase degradation and evaluation of their effect on charge transfer properties were possible by combining findings from X-ray absorption spectroscopy (XAS), X-ray diffraction (XRD), electrochemical impedance spectroscopy (EIS). Ruling out phases that did not match with XAS improved the reliability of our thin film XRD analysis.

As a result, pure O_2 gas condition was ideal, with good interface stability and decrease of interface resistance up to 700 °C. Sample annealed at 700 °C in O_2 had the lowest Area Specific Resistance (ASR), 130 $\Omega \cdot cm^2$. This value is comparable to the lowest ASRs obtained at $LiCoO_2$|LLZO interfaces *with* coated interlayers.[83–86] In this work, by removing CO_2 from the gas environment during sintering, we succeeded in obtaining comparably low ASRs without the additional steps of depositing a protective interlayer.

To verify the relevance of the O_2-annealed interface, we have prepared and tested a Pt|NMC622|LLZO|Li cell, where the NMC622|LLZO was first annealed in O_2 at 700 °C. This sample had a first-charge capacity of 117 mAh/g, comparable to an earlier report on NMC622|LLZO all solid battery with a Li_3BO_3 interlayer[87], and with the voltage plateaus for charging and discharging consistent with the lithiation and delithiation of NMC622. This result demonstrated that annealing the NMC622|LLZO in pure O_2 can indeed provide good initial electrochemical properties. Annealing in N_2 also led to a stable interface without any secondary phase formation. However, XAS revealed oxygen loss from NMC622. Even though the N_2 condition was less ideal than pure O_2, it could be a more cost-effective alternative compared to pure O_2 gas. Samples were hydrated after they were annealed in humidified O_2 at 500 °C, causing interface resistance increase. Upon further increase of annealing temperature in humidified O_2, NMC622 was dehydrated at 700 °C and had a lower interface resistance, comparable to that in pure O_2. This verified that the detrimental effect of humidity can be avoided if the annealing temperature is high enough. Finally, CO_2 environment was the most detrimental. Secondary phases formed at 500 °C and 700 °C, leading to a complete loss of the cathode|electrolyte capacitance. This comparison concludes that CO_2 is the key contributor for the interface degradation of NMC622|LLZO under thermal annealing conditions in ambient air.

These experimental results agree well with our thermodynamic predictions described above. The reaction between the cathode and the electrolyte was nonspontaneous ($\Delta G_{reaction} > 0$) for O_2 and N_2 environment, demonstrating that the interface should be stable in both gas conditions. The reaction was spontaneous at 300 °C ($\Delta G_{reaction} < 0$) and nonspontaneous at 700 °C ($\Delta G_{reaction} > 0$) in humidified environment, which is consistent with the experimental findings that the adverse effect of humidity can be reversed at high temperature. Finally, the reaction was spontaneous

($\Delta G_{reaction} < 0$) for pure CO_2 at 300 °C to 700 °C, which is consistent with the major degradation found in CO_2 environment.

Our findings demonstrate the importance of controlling the gas environment during the sintering process to obtain good contact between the ceramic cathode and ceramic electrolyte in solid state batteries. Co-sintering the cathode and electrolyte in O_2 environment gives chemically stable interface with low interfacial resistance.

3.2. Experimental design and methods

We prepared Al doped $Li_7La_3Zr_2O_{12}$ (LLZO) pellets in a two-step process. The first step was to make LLZO powder by solid-state reaction. We mixed the precursors (Li_2CO_3, La_2O_3, ZrO_2, Al_2O_3) in a mortar for 30 minutes. Al:Li:La:Zr molar ratio in the mixture was 0.24:6.9:3:2. We used 10% excess Li to compensate for Li loss during the high temperature treatment. The mixture was sintered in an alumina crucible at 900 °C for 12 h in air. After the heat treatment, we grinded the product in a mortar for 30 min to make fine powder. The second step was to make pellets from the powder. We pressed the powder in a 10 mm diameter pressing die to make pellets. The pellets were sintered in a MgO crucible at 1160 °C for 15 h in air. We covered the pellets with LLZO powder during sintering to compensate for Li evaporation. We polished the sintered pellets using 600 grit, 800 grit, 1000 grit, 1200 grit paper in sequence.

We prepared samples for XAS and XRD by depositing 100 nm thin dense NMC622 layers on top of polished LLZO pellets by RF sputtering at ambient temperature. Conditions for RF sputtering of NMC622 was same as discussed in section 2.2. This thickness allows for sensitivity to the buried interface while measuring the transition metal L-edge spectrum XAS.[81] Annealing conditions were 300 °C, 500 °C, 700 °C for 4 h in different gas environments, including pure O_2, pure N_2, humidified O_2 (2 wt% H_2O in O_2), and pure CO_2 at 1 atm. We prepared the humidified O_2 (2 wt% H_2O in O_2) environment by flowing O_2 through a gas bubbler at room temperature. Temperature range used for annealing in this work includes crystallization temperatures for deposited layered oxide cathode thin films.[42–45]

We prepared symmetric cells for EIS characterization by depositing 60 nm NMC622 on both sides of polished LLZO pellets, and with 60 nm Au on NMC622 for current collection. Annealing of the samples in the same conditions as described above were done prior to Au

deposition. Since these symmetric cells do not have an anode|electrolyte interface, the change in the EIS was only a result of changes at the cathode|electrolyte interfaces. We worked with a thicker NMC622 layer, 370 nm, with ¼" diameter, for electrochemical cycling experiment. After annealing the NMC622|LLZO at 500 °C for 4 h in O_2, we deposited 200 nm Pt current collector on top of NMC622 film. We used a 5/16" diameter Li metal foil anode, pressed onto the polished LLZO pellet in the glovebox. Annealing condition for Li attachment was 160 °C, 30 min. Polishing, annealing and pressing lowers the LLZO|Li interfacial resistance and gives stable overpotential at the interface during cycling.[11,22]

3.3. Thermodynamic calculations of interfacial degradation

We used $LiCoO_2$ for thermodynamic calculation of the Gibbs free energy to predict and interpret qualitatively the reactivity between LLZO and a layered oxide cathode. LCO is simpler than NMC622 in deducing the reaction pathways and products, but yet representative as a layered transition metal oxide. In our earlier work, we have found that $LiCoO_2$|LLZO interface decomposes by forming Li deficient phases ($LaCoO_3$, $La_2Zr_2O_7$) and a Li-sink (Li_2CO_3) upon thermal annealing in air.[37] Based on this finding, we propose that the following reactions between $LiCoO_2$ and LLZO in different gas conditions include a Li-sink and Li-deficient phases:

(a) Pure O_2 environment:
$Li_7La_3Zr_2O_{12} + LiCoO_2 + 2O_2\ (g) \rightarrow 4Li_2O_2 + LaCoO_3 + La_2Zr_2O_7$

(b) Inert environment:
$Li_7La_3Zr_2O_{12} + LiCoO_2 \rightarrow 4Li_2O + LaCoO_3 + La_2Zr_2O_7$

(c) Humidified environment:
$Li_7La_3Zr_2O_{12} + LiCoO_2 + 4H_2O\ (g) \rightarrow 8LiOH + LaCoO_3 + La_2Zr_2O_7$

(d) CO_2 environment:
$Li_7La_3Zr_2O_{12} + LiCoO_2 + 4CO_2\ (g) \rightarrow 4Li_2CO_3 + LaCoO_3 + La_2Zr_2O_7$

Then, we calculated the Gibbs free energy for each reaction with following approach. First, we obtained the formula for $C_p(T)$ for each phase. We used data from NIST-JANAF Thermochemical Tables to obtain $C_p(T)$ for Li_2CO_3, Li_2O, Li_2O_2, LiOH, O_2, CO_2, and H_2O.[88] $C_p(T)$ for LLZO[89] and $LiCoO_2$[90] were given by respective former works. As for $La_2Zr_2O_7$[91] and $LaCoO_3$,[92] we fitted experimentally given C_p for discrete temperatures to the following function.

$$C_p(T) = A + BT + CT^2 + DT^3 + \frac{E}{T^2}$$

Second, we calculated H°(T,1 bar) and S°(T,1 bar) for each phase by using standard formation enthalpy (H_f°(298.15 K, 1 bar)), standard entropy (S°(298.15 K, 1 bar)) and C_p(T). We used data from NIST-JANAF Thermochemical Tables to acquire standard formation enthalpy and standard entropy for Li_2CO_3, Li_2O, Li_2O_2, LiOH, O_2, CO_2, and H_2O.[88] Standard formation enthalpy and standard entropy for LLZO,[89] $LiCoO_2$,[93] $La_2Zr_2O_7$,[91] $LaCoO_3$[92,94] are given from corresponding works. We haven't considered terms for C_p(T) of elements when calculating H°(T,1bar) since they cancel out in the next step.

$$H°(T, 1\ bar) = H_f°(298.15\ K, 1b\ ar) + \int_{298.15\ K}^{T} C_p(T_1)dT_1$$

$$S°(T, 1\ bar) = S°(298.15K\ , 1\ bar) + \int_{298.15\ K}^{T} \frac{C_p(T_1)}{T_1} dT_1$$

Third, we calculated ΔH°(T,1 bar) and ΔS°(T,1 bar) for the proposed reaction by using H°(T,1 bar) and S°(T,1 bar) found for each phase in the previous step.

Finally, we calculated ΔG(T,P_{gas}) for the proposed reaction by using ΔH°(T,1 bar), ΔS°(T,1 bar) found in previous step and considering pressure dependence. Since $\left|\left(\frac{\partial G}{\partial P}\right)_T\right|$ for the gas phase is much bigger than the solid or liquid phase, we only considered the pressure dependence of gas phase.

$$\Delta G(T, P) = \Delta H°(T, 1\ bar) - T\Delta S°(T, 1\ bar) + \sum n_{gas} RT \ln \frac{P_{gas}}{P°}$$

P°=1 bar

Figure 10 shows the Gibbs free energy, ΔG(T,P_{gas}) (in units of kJ/mol of LLZO), of these reactions for each gas environment. The pressure and temperature ranges for these calculations are 10^{-5} bar to 1.01325 bar (1 atm), and 300 °C to 700 °C respectively.

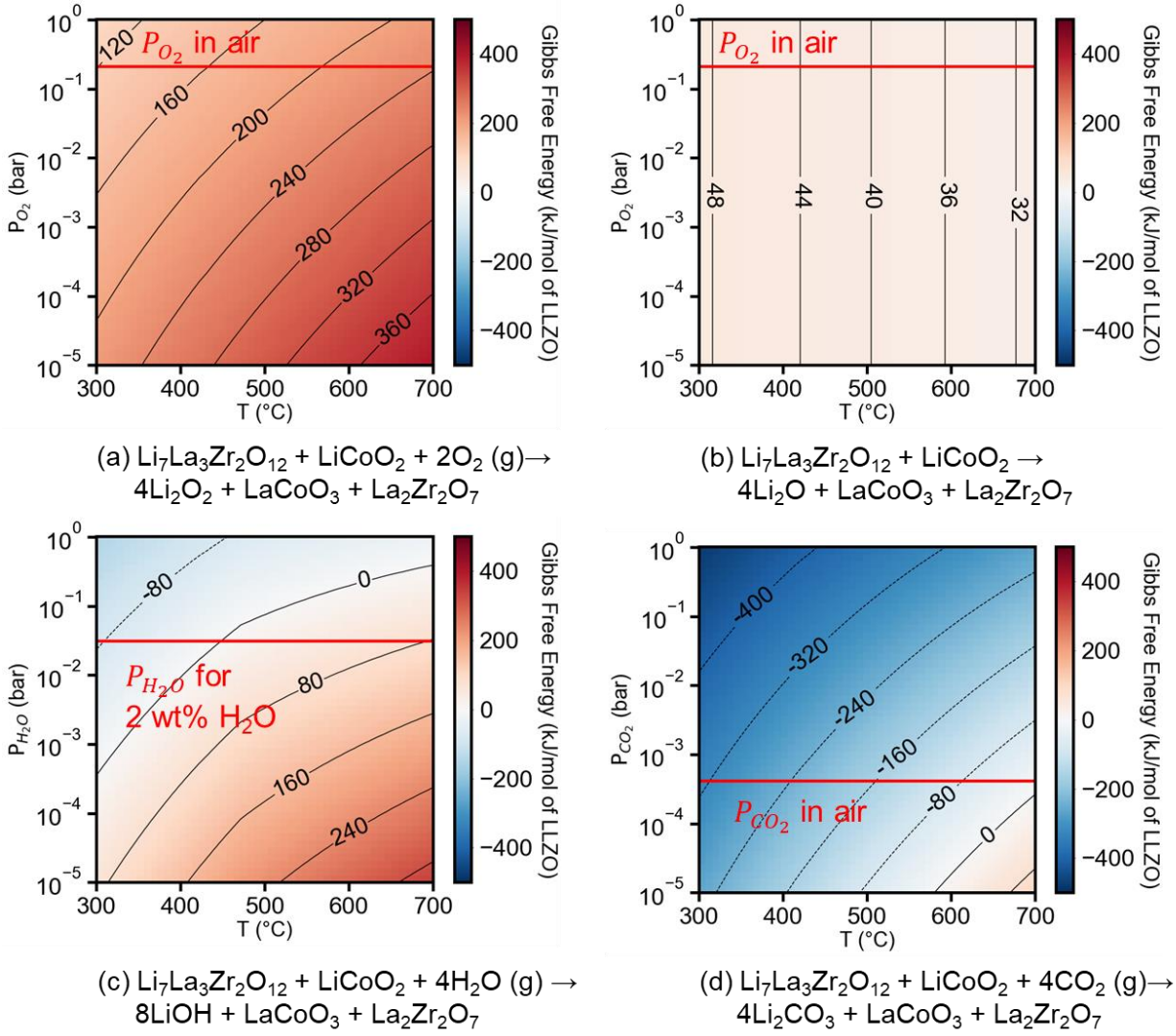

Figure 10. The Gibbs free energy, $\Delta G(T,P_{gas})$ (kJ/mol of LLZO) calculated between LLZO and fully lithiated $LiCoO_2$ in (a) $Li_7La_3Zr_2O_{12} + LiCoO_2 + 2O_2(g) \rightarrow 4Li_2O_2 + LaCoO_3 + La_2Zr_2O_7$, (b) $Li_7La_3Zr_2O_{12} + LiCoO_2 \rightarrow 4Li_2O + LaCoO_3 + La_2Zr_2O_7$, (c) $Li_7La_3Zr_2O_{12} + LiCoO_2 + 4H_2O(g) \rightarrow 8LiOH + LaCoO_3 + La_2Zr_2O_7$, (d) $Li_7La_3Zr_2O_{12} + LiCoO_2 + 4CO_2(g) \rightarrow 4Li_2CO_3 + LaCoO_3 + La_2Zr_2O_7$

The calculated reaction energies $\Delta G(T,P_{gas})$ indicate stable cathode|electrolyte interface when the sample is annealed in O_2 and in inert environment. Reactions in those two gas environments were always nonspontaneous in the temperature and pressure ranges in Figure 10 (a) and Figure 10 (b). In contrast, $\Delta G(T,P_{gas})$ for the reaction including $H_2O(g)$ was negative (spontaneous) below 449°C and positive (nonspontaneous) over 449 °C for humidified O_2 (2 wt% H_2O in O_2) (Figure 10 (c)). CO_2 was the most detrimental gas environment. $\Delta G(T,P_{gas})$ for CO_2 environment

was the most negative when compared to $\Delta G(T,P_{gas})$ values for other environments at same pressure and temperature conditions (Figure 10 (d)). Moreover, ΔG was always negative for 1atm CO_2 at 300 °C to 700 °C. Therefore, these thermodynamic calculations predict interfacial degradation upon annealing in CO_2 environment.

3.4. Oxidation state and local chemical environment analyzed by soft X-ray absorption spectroscopy

We investigated O K-edge, Ni $L_{2,3}$-edge, La $M_{4,5}$-edge, Co $L_{2,3}$-edge of the NMC622|LLZO samples annealed in different gas environments. Figure 11 shows O K-edge spectra. for The pre-edge feature (528-532 eV) corresponds to electronic transition from the oxygen 1s orbital to the oxygen 2p orbital that is hybridized with the transition metal 3d orbitals.[46] Neither LLZO nor Li_2CO_3 has features in this energy range.[32,37,47] Therefore, any change in this O K pre-edge feature is only dependent on the change of the oxygen-transition metal bonds in the system. Broad features around 542 eV correspond to electronic transition to hybridized states between oxygen p orbitals and transition metal 4s, 4p orbitals. [46]

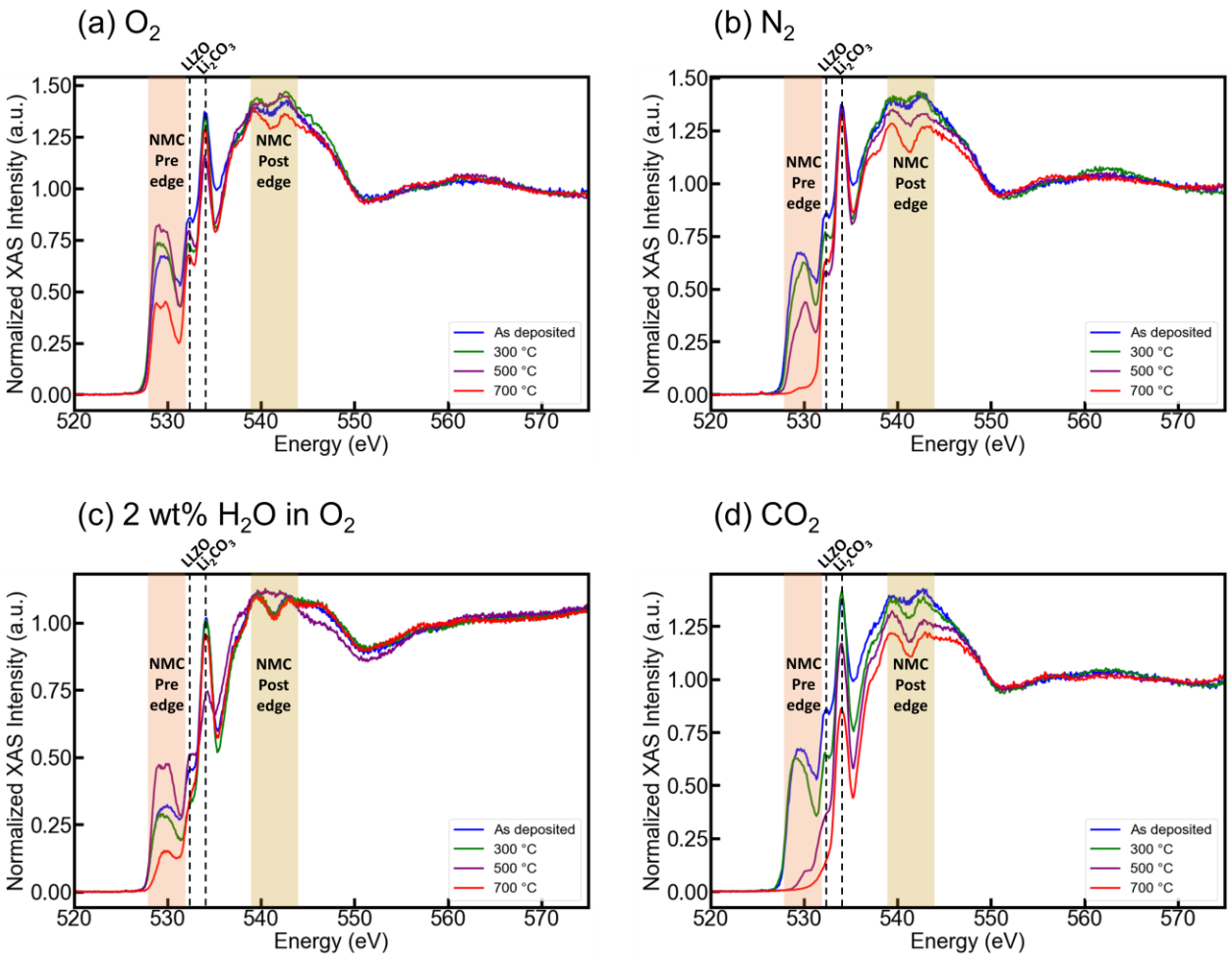

Figure 11 O K-edge X-ray Absorption Spectra measured by partial fluorescence yield (PFY) mode for 100 nm NMC622|LLZO. Spectra for the as-deposited sample and the samples annealed in (a) O_2, (b) N_2, (c) 2 wt% H_2O in O_2, (d) CO_2 at 300-700 °C for 4 h are shown.

The intensity of the pre-edge feature increased up to 500 °C and decreased at 700 °C for samples annealed in O_2 (Figure 11 (a)). The pre-edge intensity growth originates from the increase of coordination number of transition metals with oxygen due to oxidation of the sample. Decrease of the pre-edge feature at 700 °C shows that there exists some degree of chemical evolution even in O_2 environment, but it is not as severe as other gas environment (N_2, humidified O_2, CO_2) as seen in Figure 11 (b)-(d).

The pre-edge feature intensity decreased as annealing temperature increased for samples annealed in N_2 (Figure 11 (b)). Especially, the intensity of the pre-edge feature at 700 °C

dropped considerably compared to the as-deposited sample. The trend originates from the decrease of coordination number of transition metals with oxygen due to oxygen loss in N_2 environment. The result matches well with works by Guo et al.,[95] and Zhong et al.[96] on oxides with transition metal-oxygen bonds. O K pre-edge intensity decreased as the number of oxygen vacancies increased in both studies.[95,96]

Pre-edge intensity for the sample annealed in humidified O_2 was highest at 500 °C. Data from the sample annealed at 500 °C stood out since pre-edge intensity for the other temperature conditions in humidified O_2 decreased as annealing temperature increased. Moreover, post-edge features around 542 eV were much broader than the spectra obtained from other temperature conditions.

Hydration of NMC622 at 500 °C explains findings from the O K-edge analysis. Hydration of $LiNiO_2$, which has the same crystal structure as NMC622, happens by Li^+/H^+ substitution.[97,98] Moshtev et al., suggested that γ-NiOOH, which is isostructural to $LiNiO_2$, forms by Li^+/H^+ substitution in $LiNiO_2$.[99] Pritzl et al.,[100] and Jeong et al.[101] also claimed phase transformation from layered oxide to M-OOH(M:Ni,Co) like structure by hydration. Especially, Jeong et al., observed formation of CoOOH at the surface of hydrated $LiCoO_2$ with XPS.[101]

γ-NiOOH O K-edge EELS spectra had a stronger pre-edge feature and a broader post-edge feature compared to $LiNiO_2$,[102] which agrees with our finding (Figure 11(c)). In our case, hydration led to the formation of γ-NiOOH local chemical environment, rather than full transformation to crystallized γ-NiOOH phase since the corresponding peaks could not be seen from XRD data. Since XAS depends on local chemical environment, this is sufficient for identifying the identity of the compound from the XAS spectra in Figure 11 (c).

Pre-edge intensity decreased as annealing temperature increased for samples annealed in CO_2 (Figure 11 (d)). Notably, the pre-edge feature for NMC622 completely disappeared at 700 °C. O K-edge spectral shape matched well with Li_2CO_3.[103] Since the typical detection depth of PFY is ~100 nm,[41] more than 100 nm Li_2CO_3 has grown on the surface during annealing.

Figure 12 shows XAS spectra for La $M_{4,5}$-edge and Ni $L_{2,3}$-edge. We normalized data by La M_5-edge to compare the magnitude of Ni $L_{2,3}$-edge for each sample as we assume La oxidation state does not change. L-edge originates from 2p to 3d electronic transition,[104] so the intensity of the

Ni L-edge depends on both quantity of Ni in the detection regime and number of holes in 3d orbitals. Therefore, Figure 12 gives not only the elemental ratio of Ni/La within the detection depth, but also the electronic configuration in each Ni 3d orbitals.

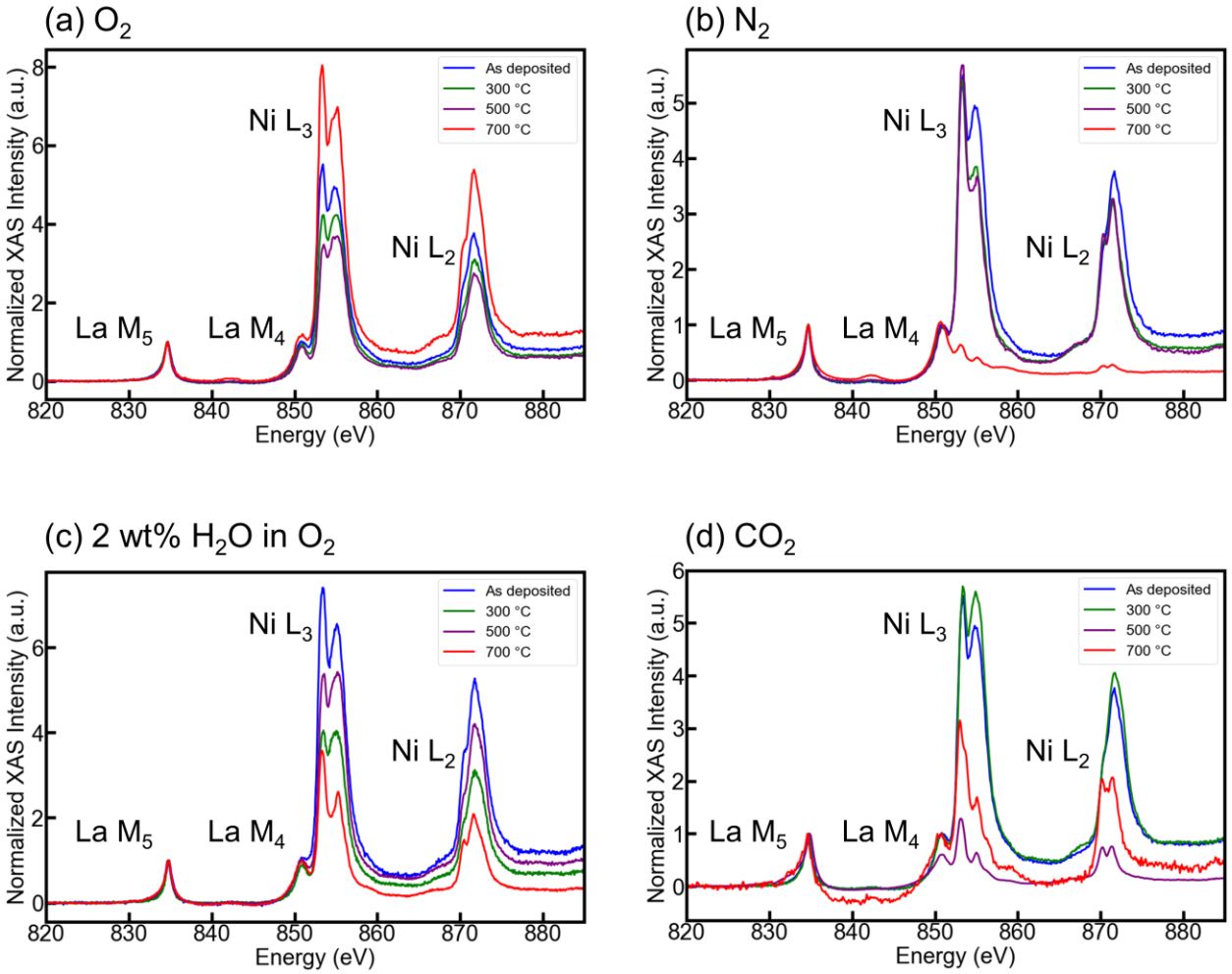

Figure 12 La M_5, La M_4, Ni L_3, Ni L_2 X-ray Absorption Spectra measured by partial fluorescence yield (PFY) mode for 100 nm NMC622|LLZO samples. Spectra for as deposited sample and sample annealed in (a) O_2, (b) N_2, (c) 2 wt% H_2O in O_2, (d) CO_2 for 4 h are shown. Intensities of peaks were normalized by La M_5 edge.

Ni L-edge intensity decreased up to 500 °C for samples annealed in O_2, likely due to migration of Ni through NMC622|LLZO interface (Figure 12 (a)). Interestingly, Ni L-edge intensity increased at 700 °C. The behavior could originate from the increase of number of Ni-O bonds due to annealing in O_2 environment. This can be due to both increased oxidation state and

increased crystalline order, along with changes in electronic structure, compared to the films that were sputter-deposited at room temperature. This led to more electrons transferred from Ni 3d orbitals to O 2p orbitals, causing increase of L-edge intensity[105].

Ni L-edge intensity decreased as annealing temperature increased for samples annealed in N_2 (Figure 12 (b)). Notably, Ni L-edge intensity decreased steeply at 700 °C because of oxygen loss, as the sample was annealed in reducing environment. Oxygen loss led to more electrons localized in Ni 3d orbitals, and decrease of L-edge intensity. If the behavior at 700 °C was due to Ni migration, evidences for secondary phase formation from Co L-edge XAS or XRD should also be seen considering our former study on NMC622|LLZO interfacial degradation.[81] However, those indicators were not found.

Ni L-edge intensity decreased as annealing temperature increased in humidified O_2, except the sample annealed at 500 °C (Figure 12 (c)). Formation of γ-NiOOH like local environment explains high L-edge intensity found at 500 °C, which we noted during O K-edge analysis. Oxidation state of Ni in γ-NiOOH is 3.48~3.68.[106] Therefore, it explains increase of Ni L-edge intensity due to increase of number of holes in 3d orbital.

Moreover, Ni got reduced at 700 °C in humidified O_2 (Figure 13). The low energy shoulder of the Ni L_2 edge grew and the peak shifted toward lower energy at 700 °C, which indicated reduction.[50,52,107] This comes from dehydration of the sample at 700 °C after hydration during temperature ramp up. Similar to NiOOH which decomposes to NiO, O_2, H_2O at high temperature,[97,108] dehydration of hydrated NMC622 would also leave reduced phases.

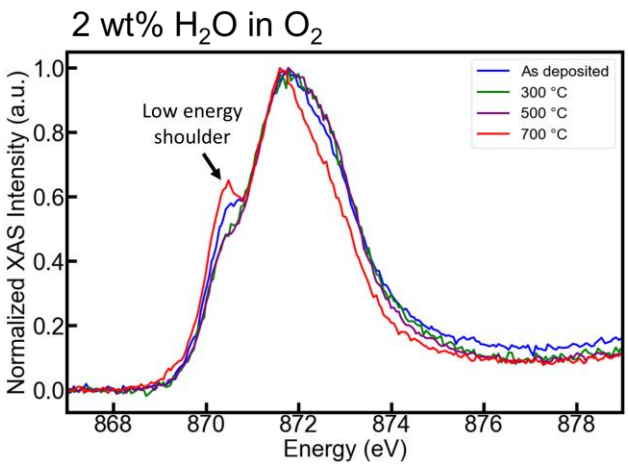

Figure 13 Ni L_2 X-ray Absorption Spectra measured by partial fluorescence yield mode for 100 nm NMC622|LLZO samples. Spectra for as deposited sample and sample annealed in humidified O_2 (2 wt% H_2O in O_2) for 4 h are shown. Intensities of peaks were normalized to 1.

Ni L_2-edge shape for samples annealed in CO_2 at 500 °C and 700 °C corresponded to Ni^{2+} (Figure 12 (d)).[109,110] This is the decisive proof for secondary phase formation as NMC622 cannot consist of 100% Ni^{2+} regardless of Li concentration.

Figure 14 shows Co L-edge spectra. We normalized signals by the height of the Co L_3 edge. Annealing in pure O_2 did not cause oxidation state change of Co, as seen by the constant peak position of the L_3 and L_2 edges. Moreover, shoulder features of L_3 and L_2 got gradually sharper as annealing temperature increased, which indicates better ordering in the film with crystallinity improvement. Although we cannot easily resolve this from XRD, it is reasonable to expect an increased crystalline order in the NMC622 films with increasing temperature. Therefore, this result indicates that O_2 environment is the ideal sintering environment, as Co remains chemically stable during sintering, along with improved crystallinity of the NMC622 film.

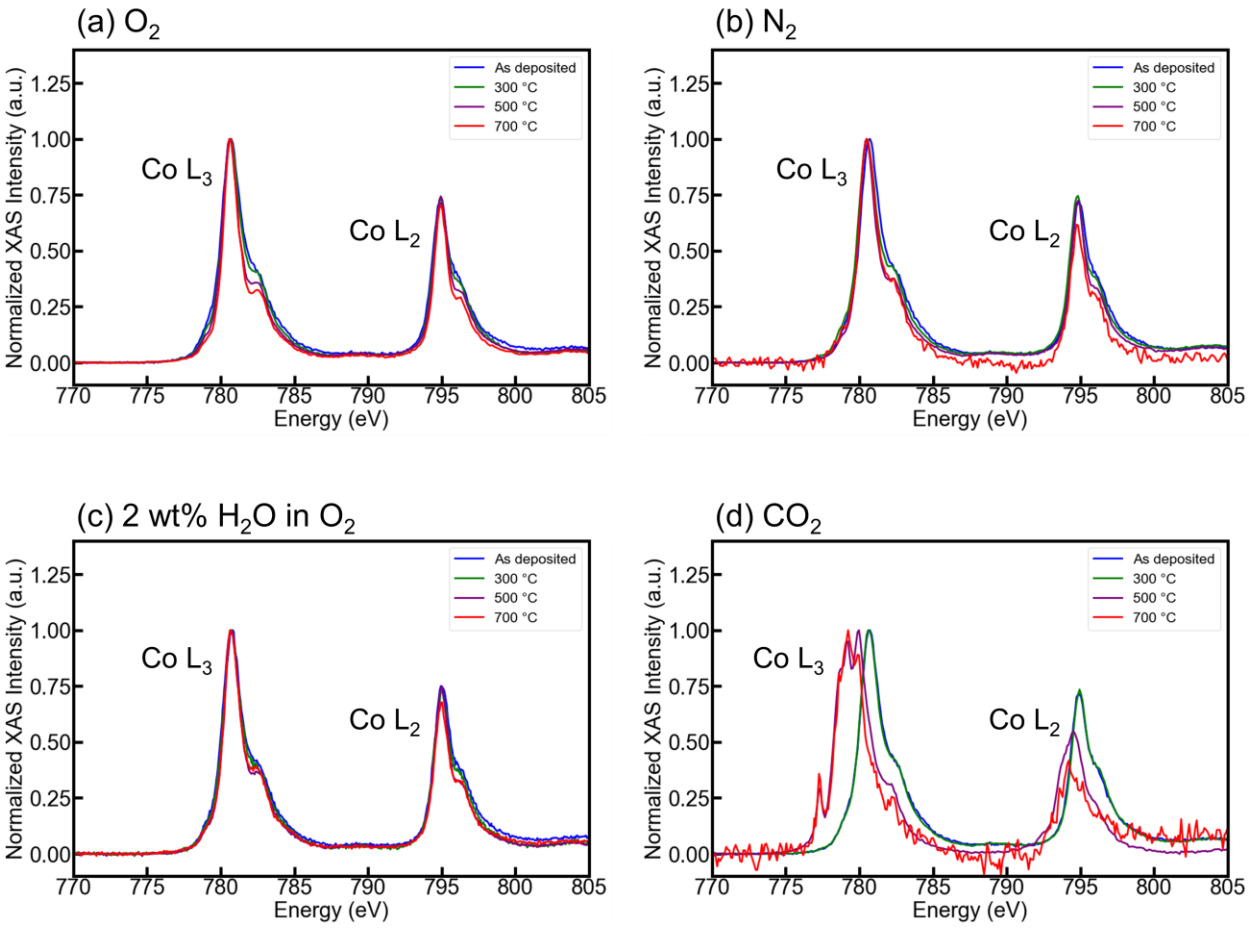

Figure 14 Co L_3, Co L_2 X-ray Absorption Spectra measured by partial fluorescence yield (PFY) mode for 100 nm NMC622|LLZO samples. Spectra for as deposited sample and sample annealed in (a) O_2, (b) N_2, (c) 2 wt% H_2O in O_2, (d) CO_2 for 4 h are shown. Intensities of peaks were normalized by Co L_3 edge.

Co was reduced after annealing in N_2, as seen by Co L-edge shift toward lower energy (Figure 14 (b)). Co was also reduced at 700 °C in humidified O_2 (Figure 14 (c)). Co L_3/L_2 intensity ratio increased at 700 °C, which indicated reduction of Co.[49] Reduction in N_2 environment came from oxygen loss, and reduction in humidified O_2 environment came from dehydration of the sample.

Annealing in CO_2 resulted in severe reduction of samples at 500 °C and 700 °C (Figure 14 (d)). The shape of both spectra matched with octahedrally coordinated Co^{2+},[111,112] which was clearly different from spectral shape for Co^{3+} (Low Spin). This is a major evidence for phase decomposition since Co with +2 oxidation state does not exist in NMC622.

3.5. Structural characterization of the interface by X-ray Diffraction

We performed XRD characterization to investigate whether crystalline secondary phases formed after annealing in each gas environment. Figure 15 (a)-(d) shows 1D XRD plots obtained using Co anode.

Secondary phases did not form after annealing in O_2 (Figure 15 (a)) and N_2 (Figure 15 (b)). We observed peaks for LLZO (ICDD:01-084-6181), and small Li_2CO_3 (ICDD: 00-022-1141) peaks from all samples. Li_2CO_3 formed due to air exposure during sample transfer and XRD characterization. In order to identify the upper limit of temperature that gives rise to a chemically stable interface in pure O_2, we annealed the NMC622|LLZO sample in O_2 at 900 °C. La_2O_3 (ICDD: 00-005-0602) and $La_2Zr_2O_7$ (ICDD: 01-070-5602) formed at 900 °C (Figure 16). Thus we can conclude that the annealing temperature should be lower than 900 °C in O_2 to avoid formation of secondary phases.

Intensity for Li_2CO_3 peaks were higher from samples annealed in humidified O_2 compared to O_2 and N_2 treated samples (Figure 15 (c)). LiOH(s) could have formed during hydration of LLZO, which formed Li_2CO_3 during sample transport to the XRD by reacting with CO_2(g) in air. Both of the reactions are thermodynamically favorable at 25 °C.[22] In addition, $La_2Zr_2O_7$ (ICDD: 01-070-5602) formed at 700 °C, potentially due to Li loss via LiOH(s) formation during annealing.

As for the CO_2 treated sample (Figure 15 (d)), Li_2CO_3 formed at 300 °C, Li_2CO_3, $La_2O_2CO_3$, $NiCO_3$, $CoCO_3$ formed at 500 °C, and Li_2CO_3, $La_2O_2CO_3$, $NiCO_3$, $CoCO_3$, La_2NiO_4, La_2CoO_4, $La_2Zr_2O_7$ formed at 700 °C.

Formation of $NiCO_3$, $CoCO_3$, La_2NiO_4, La_2CoO_4 is consistent with XAS analysis as they contain Ni^{2+} and Co^{2+}. XRD peak positions for samples annealed at 500 °C and 700 °C matched with $NiCO_3$ (ICDD:04-002-6999) (29.5° (40.5%), 38.6° (100%)) and $CoCO_3$ (ICDD: 00-011-0692) (29.2° (40.0%), 38.1° (100%)). As for the sample annealed at 700 °C, we also assigned peaks for La_2NiO_4 (ICDD:04-014-8282) (28.0° (30.2%), 36.6° (100%), 51.2° (31.4%), 55.2° (32.1%)) and La_2CoO_4 (ICDD: 04-013-8633) (27.9° (28.1%), 36.7° (100%), 51.3° (32.6%), 54.9° (32.9%)).

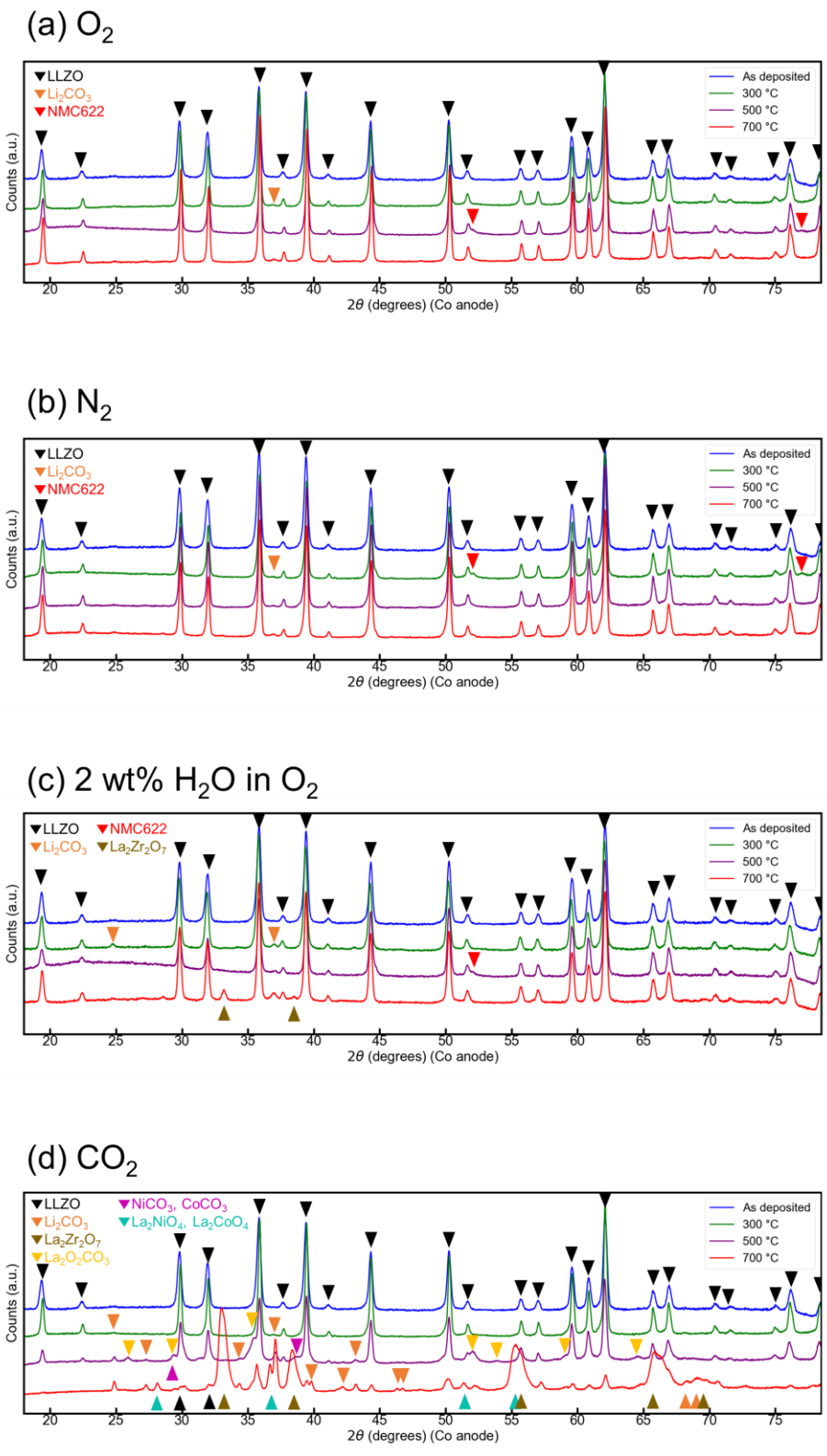

Figure 15 1D XRD plots for 100nm NMC622|LLZO samples. Plots for as deposited sample and samples annealed in (a) O_2, in (a) O_2, (b) N_2, (c) 2 wt% H_2O in O_2, (d) CO_2 for 4 h are shown.

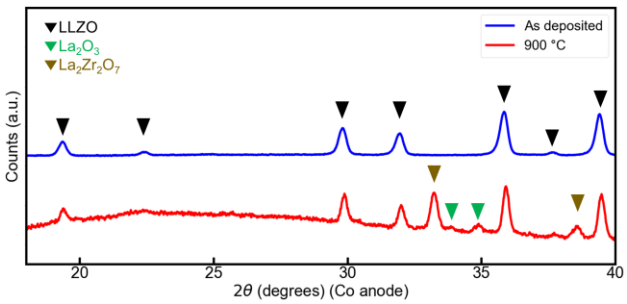

Figure 16 1D XRD plots for 100 nm NMC622|LLZO samples. Plots for as deposited sample and sample annealed in O_2 at 900 °C for 4 h are shown.

La containing secondary phases without any transition metals formed as well. $La_2O_2CO_3$ (ICDD:00-037-0804) formed at 500 °C and 700 °C as seen by peaks at 35.4° (100%), 52.0° (75%), which are two strongest peaks of the phase. $La_2Zr_2O_7$ (ICDD: 01-070-5602) formed at 700 °C, showing clear XRD peaks at 33.3° (100%), 38.7° (29.9%), 55.9° (44.3%), and 66.7° (36.9%).

Figure 17 summarizes the experimental findings from XAS and XRD analysis on chemical stability of NMC622|LLZO interface as a function of gas and temperature environment. Findings from annealing in air is from our previous paper, which we show here for comparison. Red boxes indicate secondary phases formed in each experimental condition. In the case of humidified O_2 environment, LiOH that formed during annealing further degrades into Li_2CO_3 when the sample was exposed to air after the gas exposure experiment.

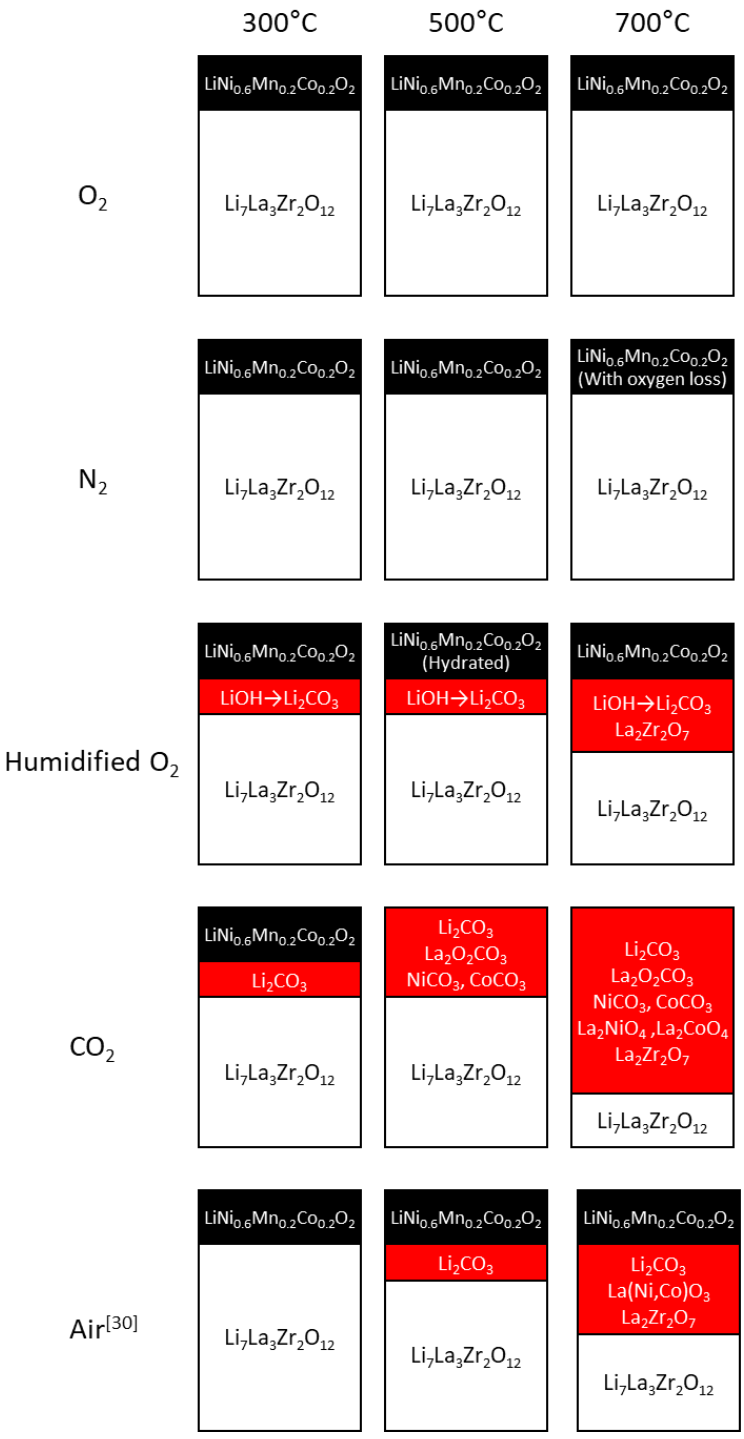

Figure 17 Reaction products at NMC622|LLZO interfaces at different temperatures in each gas environment as deduced by XAS and XRD analysis in this work. Reaction product for annealing in air is from our previous work [81] and shown here for comparison.

3.6. Implication of heat treatment in each gas environment on interfacial resistance

We performed electrochemical impedance spectroscopy (EIS) on symmetric cells, Au|NMC622|LLZO|NMC622|Au, to evaluate the effect of annealing in each gas environment on cathode|electrolyte interfacial resistance. We repeated each experiment twice, and obtained the same trend. All EIS experiments were done at room temperature.

We used a circuit model consisting of $(R_{bulk}C_{bulk})(R_{interface1}CPE_{interface1})(CPE_{tail})(L)$ to analyze the impedance spectra from the as deposited sample (Figure 18) and the samples annealed in O_2 (Figure 19), N_2 (Figure 20), humidified O_2 (Figure 21). We used different impedance ranges on the x-axes and y-axes for the figures to clearly show the semicircle corresponding to cathode|electrolyte interfacial resistance in all figures. Figures plotted with same x-axes and y-axes ranges are in Supporting Information (Figure S2-S6).

$(R_{bulk}C_{bulk})$ circuit element corresponds to capacitance of bulk LLZO pellet, and it appeared as a high frequency semicircle found at 2 MHz in all samples. C_{bulk} from samples were in the range of 20 pF to 60 pF. Considering the geometry of the sample, relative permittivity was in the range of 30-100, which consistent with former EIS studies on LLZO pellets,[68,69] and our former work with the same sample design.[81] Inductance (L) originates from wiring of the experimental setup. CPE_{tail} describes behaviors of blocking electrodes at low frequency. These two circuit elements were used in previous EIS study on LLZO pellets,[68,69] and our own previous work on symmetric cells with same structure.[81] $(R_{interface1}CPE_{interface1})$ originates from capacitance at the cathode|electrolyte interface. Semicircles corresponding to this circuit element appeared at 4kHz, which are consistent with our former works on similarly constructed symmetric cells ($Au|LiCoO_2|LLZO|LiCoO_2|Au$[37], Au|NMC622|LLZO|NMC622|Au[81]). $CPE_{interface1}$ for the as-deposited sample and the samples annealed in O_2, N_2, humidified O_2 were ~10^{-7} F, which agrees with former findings from our group[37] and reported values for electrode|electrolyte interface.[113]

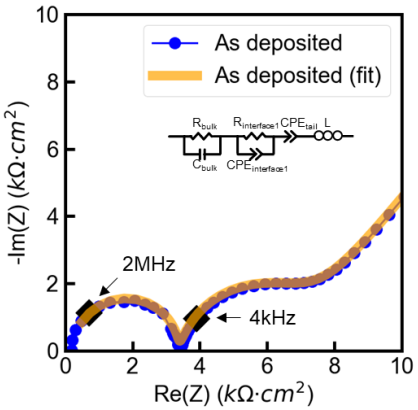

Figure 18 Electrochemical Impedance Spectroscopy plot for Au|NMC622|LLZO|NMC622|Au symmetric cells with as deposited condition. (5 MHz-31.5 Hz): $R_{interface1}/2$=1.52 kΩ·cm^2 Frequency range for the data with impedance less than 10 kΩ·cm^2 has been plotted.

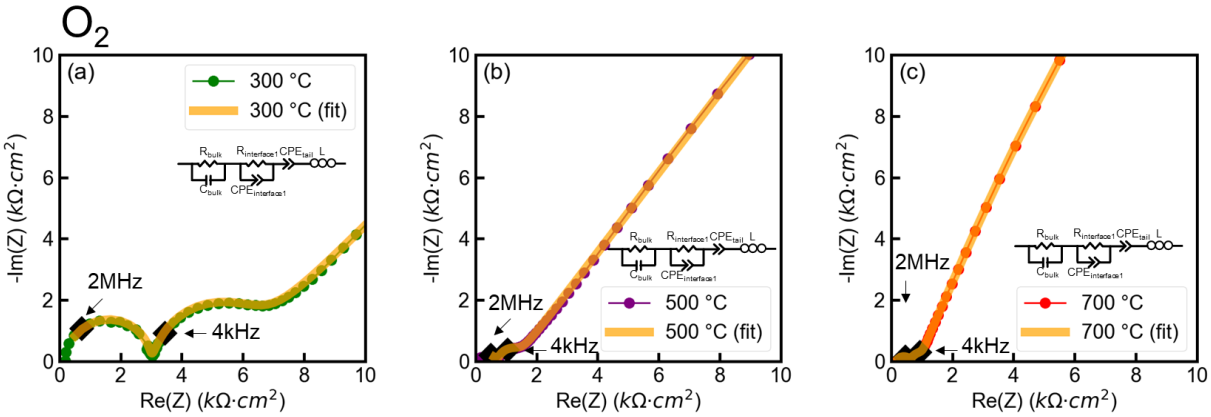

Figure 19 Electrochemical Impedance Spectroscopy plot for Au|NMC622|LLZO|NMC622|Au symmetric cells annealed in O_2 for 4 h. Frequency range for the data with impedance less than 10 kΩ·cm^2 has been plotted. (a) Annealed at 300 °C (5 MHz-19.9 Hz): $R_{interface1}/2$=1.36 kΩ·cm^2, (b) 500 °C (3.97 MHz-3.15 Hz): $R_{interface1}/2$=0.29 kΩ·cm^2, (c) 700 °C (5 MHz-19.9 Hz): $R_{interface1}/2$=0.13 kΩ·cm^2

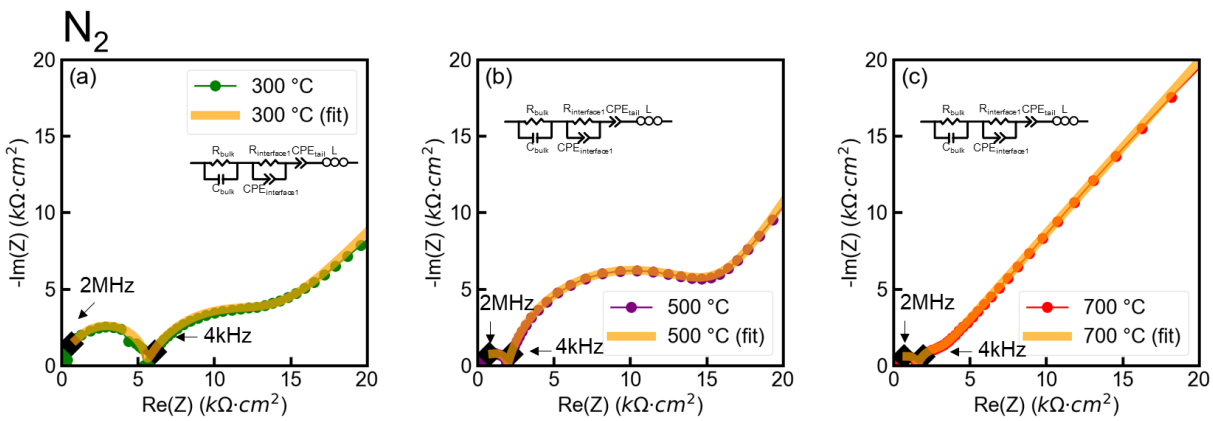

Figure 20 Electrochemical Impedance Spectroscopy plot for Au|NMC622|LLZO|NMC622|Au symmetric cells annealed in N_2 for 4 h. Frequency range for the data with impedance less than 20 kΩ·cm^2 has been plotted. (a) Annealed at 300 °C (5 MHz-6.29 Hz): $R_{interface1}/2$=3.34 kΩ·cm^2, (b) 500 °C (3.97 MHz-6.29 Hz): $R_{interface1}/2$=6.04 kΩ·cm^2, (c) 700 °C (3.97 MHz-2.51 Hz): $R_{interface1}/2$=0.41 kΩ·cm^2

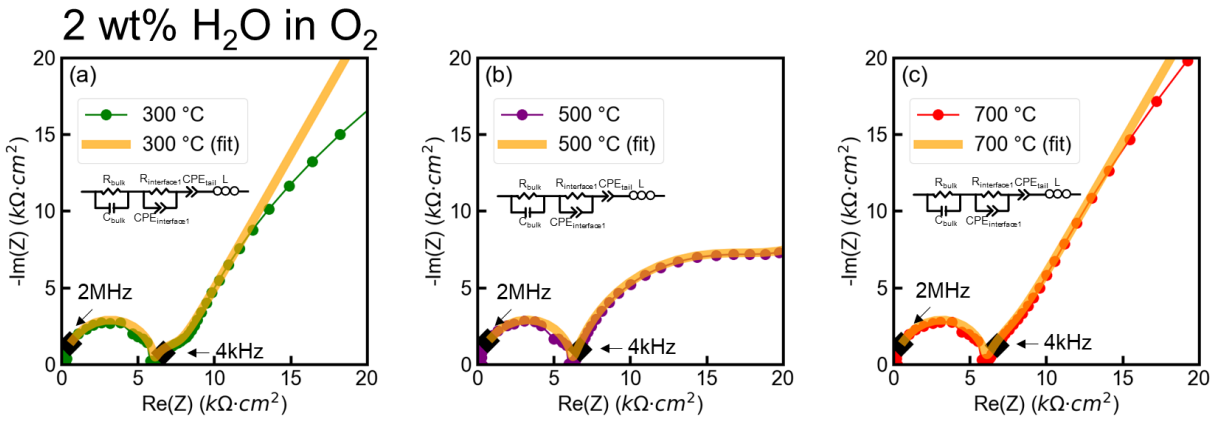

Figure 21 Electrochemical Impedance Spectroscopy plot for Au|NMC622|LLZO|NMC622|Au symmetric cells annealed in humidified O_2 (2 wt% H_2O in O_2) for 4 h. Frequency range for the data with impedance less than 20 kΩ·cm^2 has been plotted. (a) Annealed at 300 °C (5 MHz-15.8 Hz): $R_{interface1}/2$=0.58 kΩ·cm^2, (b) 500 °C (3.97 MHz-50 Hz): $R_{interface1}/2$=5.65 kΩ·cm^2, (c) 700 °C (3.97 MHz-50 Hz): $R_{interface1}/2$=0.35 kΩ·cm^2

EIS for samples annealed in CO_2 was drastically different from other gas conditions (Figure 22). Three arcs are present in the spectrum from the sample annealed at 300 °C, so we have used two RC elements for the interface, ($R_{bulk}C_{bulk}$)($R_{interface1}CPE_{interface1}$)($R_{interface2}CPE_{interface2}$)($CPE_{tail}$)(L),

for analysis. The second RC element that appear in the spectrum is likely due to formation of secondary phases as a result of interface reactions and degradation at 300 °C. In our previous study on NMC622|LLZO thermal degradation in air, such an additional arc appeared also from samples with interfacial degradation.[81] Total nominal resistance at the interface ($(R_{interface1}+R_{interface2})/2$) equaled 9.01 kΩ·cm^2.

The arc for the cathode|electrolyte interfacial charge transfer capacitance did not appear from the sample annealed at 500 °C. This is consistent with the finding that the NMC622 cathode degraded into secondary phases containing Ni^{2+} and Co^{2+} as indicated by XAS (Figure 12 (d), Figure 14 (d)) and XRD results (Figure 15 (d)), so the interfacial charge transfer capacitance was lost. At 700 °C, the sample became both ionic and electronic insulator. Data points for the high frequency range followed an RC element behavior with a very high resistance, but quantification was not possible due to noise in data for the low frequency range. Noisy data originate from low current used for data acquisition, which was due to high resistance. High resistance originates from formation of insulating secondary phases at 700 °C, which we have discussed above as part of the XRD analysis (Figure 15 (d)). Intensities of XRD peaks from the LLZO phase were much weaker than those at other conditions, so significant amount of electrolyte phase decomposition also took place, consistent with the disappearance of the bulk Li-ion conduction arc in EIS.

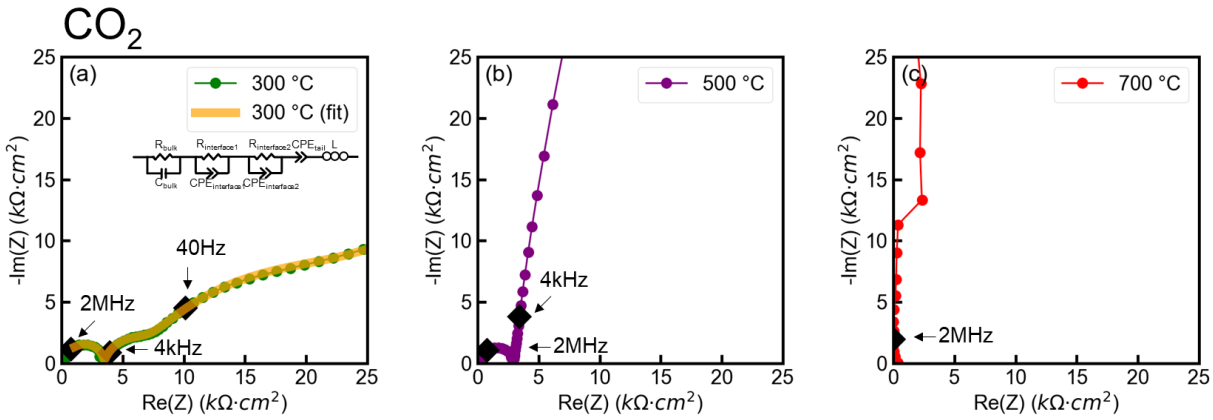

Figure 22 Electrochemical Impedance Spectroscopy plot for Au|NMC622|LLZO|NMC622|Au symmetric cells. Frequency range for the data with impedance less than 25 kΩ·cm^2 has been plotted. (a) Annealed at 300 °C (3.97 MHz-1.58 Hz): $(R_{interface1}+ R_{interface2})/2$=9.01 kΩ·cm^2, (b) 500 °C (3.97 MHz-0.63 kHz), (c) 700 °C (5 MHz-199 kHz) in CO_2 for 4 h.

Figure 23 shows Area Specific Resistance (ASR) arising from the interface component of EIS, for the as deposited sample and the samples annealed in O_2, N_2, humidified O_2, CO_2, and air. ASR data for samples annealed in air are from our previous work.[81] We plotted the data here to compare the trend. We calculated ASR for a single cathode|electrolyte interface by $\frac{R_{interface1}}{2} \times Area$ for the as-deposited sample and the samples annealed in O_2, N_2, humidified O_2, air, and by $\frac{R_{interface1}+R_{interface2}}{2} \times Area$ for the sample annealed in CO_2. Division by 2 was due to the symmetric cell design, which had two equivalent NMC622|LLZO interfaces.

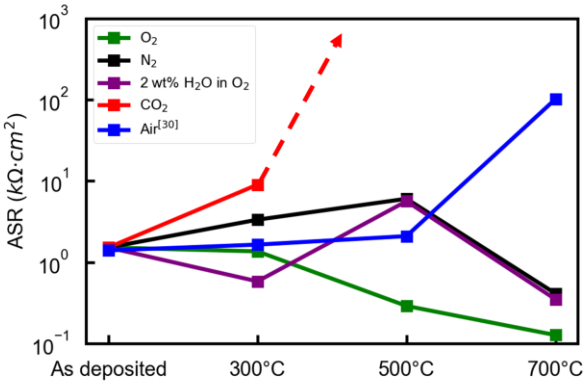

Figure 23 Area Specific Resistance (ASR) corresponding to single NMC622|LLZO interface. Data obtained from the as deposited sample and the samples annealed in O_2, N_2, humidified O_2 (2 wt% H_2O in O_2), CO_2, air for 4 h are shown. Data for samples annealed in air is from our previous work,[81] and plotted here for comparison.

ASR gradually decreased with increase in the annealing temperature the NMC622|LLZO annealed in pure O_2 environment. This confirmed that pure O_2 is the most promising condition for sintering the NMC622 and LLZO interface, since it decreased the ASR without any interfacial degradation up to 700°C.

In contrast, ASR for samples annealed in N_2 increased up to 500 °C and decreased at 700 °C. ASR increase up to 500 °C came from interfacial degradation due to oxygen loss. ASR decrease at 700 °C was likely due to expedited sintering[114] in the presence of oxygen vacancies as seen by XAS in in NMC622. This led to improved bonding between NMC622 and LLZO.

ASR for samples annealed in humidified O_2 increased at 500 °C and decreased at 700 °C. This is because of hydration at 500 °C and dehydration at 700 °C, which we identified by XAS. Li^+/H^+ substitution during hydration leads to a contraction of the O-Li-O layer thickness in the layered oxide structure, and this increases the activation energy for Li diffusion.[97] This explains the ASR increase at 500 °C. Dehydration at 700 °C restored the Li^+ transport pathway and led to ASR decrease. We believe the ASR decrease at 300 °C could arise from cold sintering in presence of humidity. Cold sintering uses a transient aqueous environment, the material surface dissolves into introduced H_2O, and the dissolution diffuses into pores and precipitates the solid phase.[115] It is considered a mediated dissolution-precipitation process, effectively decreases the volume of pores and enables sintering of particles. Therefore, the presence of controlled humidity in our experiments may have enabled further densification and sintering of the cathode layer and the cathode-electrolyte interface at low temperatures. While a lot yet has to be resolved about the mass transport at liquid-solid interfaces involved in cold sintering, this process can create a new opportunity to sinter ceramic electrolyte and cathode layers without thermally-driven reactions at the interface. Cold sintering on solid electrolyte[116] and cathode material[117] were shown to improve densification even at relatively low temperature (<300 °C). This can lead to a decreased ASR in our system as well.

Interfacial resistance increased steeply after annealing in CO_2. Notably, interfacial resistance became too high to measure when the annealing temperature was 500 °C and 700 °C. This fits with severe degradation at those temperatures demonstrated by XAS and XRD results. None of the phases in XRD characterization observed have known Li conductivity. Thus we conclude CO_2 environment is the most detrimental phase for sintering, leading to formation of insulating secondary phases.

While pure CO_2 is a lot more aggressive than the ppm-levels of CO_2 in air, the steep increase of interfacial resistance along with the formation of delithiated phases and Li_2CO_3 are consistent with our previous findings from annealing the NMC|LLZO in air.[81] After annealing at 700 °C in air, $La(Ni,Co)O_3$, $La_2Zr_2O_7$, Li_2CO_3 formed and interfacial resistance at NMC622|LLZO interface increased by two orders of magnitude compared to as deposited state. While here in pure CO_2 we find more extensive, a wider range of degradation products, similarities of reaction

pathway and interfacial resistance increase indicate that CO_2 was the key contributor of the interfacial degradation in air.

Lastly, we can also see variations of the bulk resistance of LLZO in Figures 9-11. This likely originates from the conductivity variation of LLZO pellets themselves, and are not related to annealing at different conditions. Conductivities of LLZO pellets differ in literature by two orders of magnitude even if they were prepared by nominally the same experimental procedure.[68] This can result in the different resistances of bulk LLZO in Figure 18-11. It is also possible that the LLZO bulk conductivity can vary by doping as a result of transition metal migration from NMC622 into LLZO during thermal treatment. However, doping of Ni and Co into LLZO decreases bulk ionic conductivity of LLZO.[118] This does not explain the EIS data in Figure 19 and Figure 20, in which the bulk resistance of LLZO for samples annealed at higher temperatures (potentially more diffusion of Ni and Co into LLZO) is lower than the samples annealed at lower temperatures. Therefore, potential doping of LLZO from NMC622 during annealing is not the dominant reason for the variations in bulk resistance of LLZO in the annealing experiments.

3.7. Cycling properties of the NMC622|LLZO annealed in pure O_2

We have electrochemically cycled the sample that was annealed at 500 °C in pure O_2. The NMC622|LLZO interface was chemically stable without secondary phase formation in this thermal condition as seen by the XAS and XRD results explained above. Interfacial charge transfer resistance at this condition was also lower than in the as-deposited sample, indicating improved interface sintering.

Figure 24 shows charge-discharge cycles for the Pt|NMC622|LLZO|Li cell. 1st charge capacity was 117 mAh/g, and 1st discharge capacity was 77 mAh/g, both comparable to an earlier report on NMC622|LLZO all solid battery with a Li_3BO_3 interlayer[87]. Irreversible capacity loss happened during the 1st cycle, as capacity for the 2nd charge dropped sharply to 61 mAh/g. Both the charge capacity and discharge capacity decreased gradually from 2nd to 10th cycle.

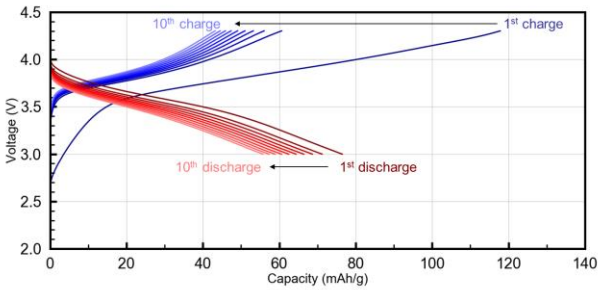

Figure 24 Charge and discharge cycles for the Pt|NMC622|LLZO|Li cell. 0.5 C current was used for cycling at 80 °C

We performed differential capacity analysis to identify the voltages at which electrochemical reactions happen. Figure 25 shows differential capacity curves for the 1st, 2nd and 10th cycles. Three distinguishable peaks appeared in the differential capacity curve for the 1st charge at 3.7 V, 3.85 V and 4.2 V. These correspond to the H1 (Hexagonal)→M (Monoclinic), M (Monoclinic) → H2 (Hexagonal), and H2 (Hexagonal)→H3 (Hexagonal) transitions of the NMC622 cathode, respectively.[119,120]

Only the features for H1→M and M→H1 transitions appeared for all charge-discharge cycles. Moreover, peaks for H1→M and M→H1 transitions shifted gradually with increasing cycle number, indicating an overpotential increase. Zhang et al. also observed peak shift during cycling of solid batteries based on $Li_{10}GeP_2S_{12}$, and attributed the phenomena to degradation at $LiCoO_2|Li_{10}GeP_2S_{12}$ interface.[121]

We attribute the sharp decrease in capacity and the increase in interfacial resistance after the first cycle to both electrochemical and mechanical instability at the NMC622|LLZO interface. Oxidation limit of LLZO according to DFT calculations is 2.91 V vs Li/Li^+.[9] Secondary phase formation due to chemical reaction could have decreased capacity, similar to the case of solid state batteries with sulfide electrolyte ($Li_{10}GeP_2S_{12}$).[122] In addition, loss of contact between NMC622 and LLZO originating from cracks and delamination at the NMC622|LLZO interface could have also decreased capacity. Crack formation and delamination at the cathode|electrolyte interface and interfacial resistance increase after initial cycling were also found in other studies on NMC622|LLZO solid state batteries with interface coatings[87,123] and on $NMC811|Li_{10}SnP_2S_{12}$ solid state batteries.[124]

As the electrochemical performance of our best cell with the thin film cathode design, and the cells with composite cathodes made of LLZO and layered oxide cathode particles from literature[87,123] are consistent with each other, we can justify the usage of our cell as a model system to understand the thermally-induced interfacial degradation in NMC622|LLZO cells.

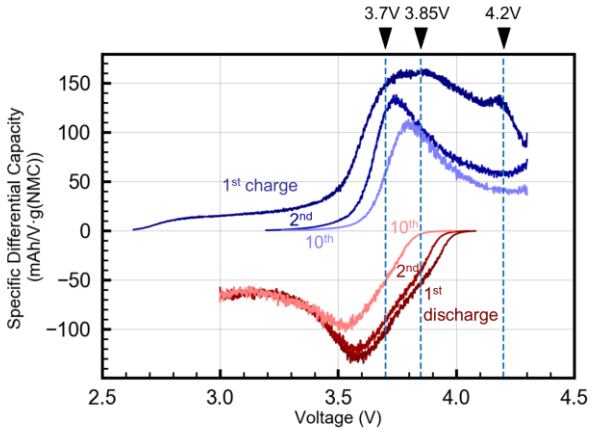

Figure 25 Differential capacity as a result of cycling the Pt|NMC622|LLZO|Li cell with 10 cycles. The 1st, 2nd and 10th cycles are shown. 0.5 C current was used for cycling at 80°C.

3.8. Discussion

We were able to isolate the potential contributions to degradation when LLZO and a layered transition metal oxide is co-sintered in air, by using gas components from air as pure gases in the annealing environment, specifically O_2, N_2, CO_2, and humidified O_2. As seen from the chemical, structural and electrochemical data presented above, pure O_2 environment was ideal during annealing the NMC622|LLZO interface up to 700 ^oC, giving rise to a chemically stable interface with lower resistance. Secondary phases did not form after annealing in N_2, either, so it can be considered as an alternative potentially less expensive choice compared to pure O_2. In contrast, annealing in humidified environment and CO_2 environment led to the formation of secondary phases. Detrimental effect of CO_2 on interfacial degradation was the most severe. These experimental results of relative stability in different gas conditions are consistent with our Gibbs free energy analysis of reactions between the layered transition metal oxide cathode material and LLZO electrolyte.

1st charge capacity of the Pt|NMC622|LLZO|Li cell was 117 mAh/g and 1st discharge capacity was 77 mAhg/g for the cell prepared by annealing the NMC622|LLZO interface at 500 °C in

pure O_2. In addition, the cell was cyclable for at least 10 more cycles afterwards. Voltages for both the lithiation and delithiation of the cathode of this cell are consistent with layered oxide cathodes in the form of powders.[119,120] This indicates that annealing NMC622|LLZO in O_2 produces cathode-electrolyte interfaces with the appropriate and relevant electrochemical properties. In addition, it justifies that our chemical and structural results obtained on such thin film cathode|LLZO model system are applicable to solid state batteries.

Sintering in O_2 would cost more, in terms of both energy and materials, compared to sintering in air due to the production of O_2, but this increase would be very small compared to the total energy consumption for the solid-state cell preparation. Based on calculations of Troy et al. on energy demand for manufacturing Al|$LiCoO_2$|LLZO|Li|Cu pouch cell,[125] we estimate co-sintering in O_2 environment will increase the total energy demand for manufacturing by only a mere 0.0027% (see Method section for details). In addition, given the relatively low cost of O_2 ($40 per ton),[126] we expect the increase in material and supply cost for sintering in O_2 environment would be negligible. Moreover, O_2 is already being used to synthesize layered oxide cathodes such as Lithium Manganese Rich Lithium Nickel Manganese Cobalt Oxide cathodes (LMR-NMC).[127] However, the more complicated system to keep operations safe in pure O_2 and to minimize O_2 loss can add to the cost of this approach. N_2 environment can be a more cost-effective alternative to pure O_2 environment. No secondary phases were detectable by XAS and XRD in NMC622|LLZO. In N_2, however, oxygen loss from NMC622 takes place at 700 °C according to XAS. Nevertheless, oxygen loss did not cause degradation of the cathode phase or its interface. Interfacial resistance decreased at 700 °C, and this is attributed to better sintering in the presence of oxygen vacancies.

In humidified O_2 environment, degradation driven by hydration took place at 500 °C and recovery due to dehydration at 700 °C. A γ-NiOOH-like local environment formed at 500 °C, which we justified by XAS and attributed to Li^+/H^+ exchange in the cathode by hydration. Annealing at 700 °C reversed the detrimental effect of humidity by dehydration. Therefore, heat treatment at sufficiently high temperature could restore the sample even after hydration. This finding is consistent with former studies on Li containing ceramics which are prone to Li^+/H^+ exchange in humidified environment. Protonated LLZO loses mass around 450 °C to 500 °C due

to deprotonation in a form of H_2O evolution.[128–130] Deprotonation of $Li_{1-x}H_xNiO_2$ was also found at 200 °C to 220 °C and 300 °C to 320 °C by thermogravimetric analysis.[97]

CO_2 environment was the most detrimental to the NMC622|LLZO interface, leading to the formation of secondary phases at 500 °C and 700 °C. The presence of Li_2CO_3 and $La_2Zr_2O_7$ as a result of annealing in CO_2 matched with our previous findings in NMC622|LLZO when annealed in air.[81] Peak intensities of LLZO from the sample annealed at 700 °C was very low, indicating most of LLZO within the detection depth had degraded into secondary phases. In addition, carbonated species ($La_2O_2CO_3$, $NiCO_3$, $CoCO_3$) and reduced species (La_2NiO_4, La_2CoO_4) were also found when the sample was annealed in CO_2. This severe degradation originates from higher P_{CO_2} and lower P_{O_2} in pure CO_2 compared to air. These found secondary phases are not Li-ion conductors. Li_2CO_3 has limited Li-ion conductivity (10^{-3} mS/cm) at room temperature, much lower compared to that in LLZO.[72] $La_2Zr_2O_7$ and Ruddelsden-popper phases are also not Li-ion conductors.[25,70] We do not expect carbonated species ($La_2O_2CO_3$, $NiCO_3$, $CoCO_3$) to have good Li-ion conductivities since they do not have Li in their lattice nor cation vacancy channel for Lithium ion transport. As a result, these insulating secondary phases block Li transfer at the interface, resulting in the very high resistances found by EIS (Figure 22).

These findings justify our claim that Li_2CO_3 formation by reaction with ambient CO_2 is the deciding factor for the thermal interfacial degradation when the cathode(NMC622, LCO)-LLZO interface is sintered in air.[37,81] This experimental finding is in accordance with the Gibbs free energy analysis, which predicted spontaneous reaction between cathode and electrolyte even with partial pressure of CO_2 in air (4.12×10^{-4} atm for 412 ppm concentration[131]) at 300 °C to 700 °C (Figure 10).

The degradation reactions nucleate at the interface between the ceramic cathode and the ceramic electrolyte. In order to be sensitive to this process initiating at the interface, we have used thin film (≤100 nm) cathode layers, so that we could capture the onset of the reactions even if only a small volume is affected. Because we are working with thin cathode layers, once the interface reactions nucleate and propagate, it looks as if we are transforming the bulk of the cathode layer, but this is because we are working with thin films. This is different from conventional cell design in which cathode particles with diameter larger than 1 μm are used.[84] For example in our prior work with LCO|LLZO, we have shown that 5-20 nm thickness from the interface is affected by

these reactions at 300 °C, and about 100 nm at 500 °C.[37] Given the small volume and the disordered nature of these reacted interface zones, it is impossible to capture them with powder XRD at their onset conditions. Our approach combining thin-films with spectroscopy targets that, and captures the chemical and structural changes nucleating at the interface and propagating from the interface after they onset. This process indeed relates to the cathode-electrolyte interface reactions if powder cathode particles were used on an LLZO, but this does not necessarily mean the entire bulk of the cathode particles would have reacted in that more conventional geometry.

As a result, pure O_2 gas condition was ideal, with good interface stability and decrease of interface resistance up to 700 °C. NMC622|LLZO annealed at 700 °C in O_2 had the lowest Area Specific Resistance (ASR), 130 $\Omega \cdot cm^2$. This value is comparable to the lowest ASRs obtained at $LiCoO_2$|LLZO interfaces *with* coated interlayers[132]; for example 230 $\Omega \cdot cm^2$ with Li_3BO_3 interlayer[83], 101 $\Omega \cdot cm^2$ with Li_2CO_3 + $Li_{2.3}C_{0.7}B_{0.3}O_3$ interlayer[84], 150 $\Omega \cdot cm^2$ with Nb interlayer[85], and 53.5 $\Omega \cdot cm^2$ with Nb_2O_5 interlayer[86]. In this work, by removing CO_2 from the gas environment during sintering, we succeeded in obtaining comparably low ASRs but without the need for an interlayer. This is an advantage, because the introduction of the interlayer coatings into the battery cell also introduce additional, elaborate and costly thin-film processing steps in the fabrication of the battery. In order to be competitive with liquid batteries whose ASR is ~22 $\Omega \cdot cm^2$,[133] we need to lower the ASR further. We expect the NMC622|LLZO interface ASR could be lowered further, for example by a fast firing technique at high temperature for a short time with high ramp rate,[134] to expedite and enhance densification at the interface.

Although we have not done experiments in dry air and synthetic air, we can predict the outcome based on our findings in this paper. Dry air or synthetic air can be other potential gas environment for annealing and bonding the NMC622|LLZO interface. As for dry air, we expect interfacial degradation since dry air still has CO_2, and the Gibbs Free Energy for the reaction was negative (spontaneous) with CO_2 partial pressure (of 4.12×10^{-4} atm for 412 ppm concentration[131]) in air. On the other hand, for synthetic air (made of pure O_2 and pure N_2) we do not expect interfacial degradations, since the environment is CO_2-free and the Gibbs Free Energy for the reaction was positive (non-spontaneous) and secondary phase did not form in both O_2 and N_2.

We also note that the degradation mechanism in CO_2 and the way to mitigate it on the LLZO-cathode interface is different from that on the LLZO-Li anode interface. On the LLZO-Li metal anode interface, CO_2 reacts with LLZO and forms Li_2CO_3, and this substantially degrades physical wetting and contact area of Li metal on LLZO, thus increases the interface resistance.[22,48] Physically removing that Li_2CO_3 prior to pressing the Li metal anode layer onto the ceramic electrolyte circumvents that issue.[22] What we find on the cathode side is very different. The degradation during synthesis of the cathode-electrolyte interface in air or in CO_2 is rather due to the formation of Li-deficient secondary phases, such as $La_2Zr_2O_7$ and perovskite-related oxides (e.g. $La(Ni,Co)O_3$), as a result of Li-loss in the form of Li_2CO_3, and not by loss of physical contact between LLZO and the oxide cathode. Therefore, one has to avoid formation of Li-deficient secondary phases. This can be done by avoiding CO_2 in the environment, and this approach reduces the interface resistance to lowest values reported in literature where elaborate coatings had to be used. We believe this is an important insight to guide how to synthesize cathode-electrolyte material interfaces in the best way.

3.9. Conclusion

The goal of this chapter was to isolate and identify the key contributors to degradation when LLZO and a layered transition metal oxide is co-sintered in air. For that, we have used gas components from air as pure gases in the annealing environment of NMC622|LLZO, specifically O_2, N_2, CO_2, and humidified O_2 at 300 °C to 700 °C. Findings from our thermodynamic predictions (Gibbs Free Energy analysis of reactions), chemical and structural characterization (XAS and XRD), and electrochemical analysis (EIS) correlate well with each other. Annealing in pure O_2 gas has given the best result. The interface remained stable at up to 700 °C while interfacial resistance at room temperature decreased from 1500 $\Omega \cdot cm^2$ to 130 $\Omega \cdot cm^2$. This is comparable to the lowest interface ASR values obtained by using protective interlayer coatings between LLZO and layered transition metal cathodes; but here without the additional step of an interface coating. Capacities and potentials of charging/discharging plateaus for the Pt|NMC622|LLZO|Li cell prepared by annealing the NMC622|LLZO in pure O_2 matched well with previous studies on NMC622. The interface also remained free of secondary phases when annealed in N_2. However, oxygen loss took place at 700 °C. In humidified O_2, NMC622 was hydrated at up to 500 °C and dehydrated at 700 °C, consistent with the calculated Gibbs free energy of reactions. Therefore, if a completely dry environment is not possible, using sufficiently

high sintering temperature can minimize or avoid the detrimental effect of humidity. Annealing in CO_2 was the worst condition, and caused the formation of insulating secondary phases that block and diminish the charge transfer capability. Removing CO_2(g) from the sintering gas environment is important for the successful co-sintering of LLZO and layered transition metal oxide cathode materials without interfacial degradation. Co-sintering in pure O_2 environment gives the best result in terms of both interfacial chemical stability and interfacial resistance.

4. Electrochemical stability at $LiNi_{0.6}Mn_{0.2}Co_{0.2}O_2|Li_7La_3Zr_2O_{12}$ interface

4.1. Introduction

In Chapter 2 and Chapter 3, we discussed thermal stability at layered oxide cathodes|LLZO interface, which is related to manufacture of the All-solid-state batteries. We confirmed that avoiding CO_2 and using O_2 during sintering gives chemically stable interface with low interfacial resistance. In this chapter, we discuss electrochemical stability issues at NMC622|LLZO interface, which is related to the cell operation.

Electrochemical degradation at NMC622|LLZO interface occurs by oxidation of LLZO at high voltage along with reduction of transition metals in NMC622. LLZO has limited oxidation stability limit (2.91 V) and decomposes to secondary phases ($Li_6Zr_2O_7$, Li_2O_2, La_2O_3) over 2.91 V according to DFT calculation.[9] In addition, Ni^{4+} in charged Lithium Nickel Manganese Cobalt Oxide is susceptible to reduction by oxygen loss since energy level for lowest unoccupied molecular orbital (LUMO) of Ni^{4+}-O bond is low.[135] We hypothesized that oxidation of LLZO and reduction of transition metal in NMC622 proceeds by oxygen transfer from NMC622 to LLZO. Our proposed degradation pathway is similar to electrochemical degradation at $LiNi_{0.8}Mn_{0.1}Co_{0.1}O_2|$ β-Li_3PS_4 interface during cycling. β-Li_3PS_4 reacts with $LiNi_{0.8}Mn_{0.1}Co_{0.1}O_2$ during cycling and forms oxidized phases because of its limited oxidation stability.[136]

Although NMC622 could decompose on its own by oxygen evolution, it requires high voltage (Renfrew et al[137]: 4.55V vs Li/Li^+, Jung et al[120]: 4.7 V vs Li/Li^+). Therefore, if transition metals in NMC622 reduced during cycling when charge voltage cutoff was lower than inherent stability limit of NMC622, it was due to electrochemical degradation at NMC622|LLZO interface.

DFT analysis for reaction between delithiated NMC622 and LLZO predicts formation of phases (NiO, La_2CoMnO_4)[18] with reduced transition metals (Ni^{2+}, Co^{2+}) that have poor Li-ion conductivities. Therefore, we expect the electrochemical degradation to negatively impact cyclability of All-Solid-State Batteries with NMC622 cathode and LLZO solid electrolyte. Despite the importance of electrochemically stability on cell performance, experimental characterization of the degraded phases formed at NMC622|LLZO interface due to electrochemical cycling is still missing.

Tracking oxidation state of transition metals near the interface during cell operation is necessary to understand electrochemical stability at the interface. For this purpose, we designed All-solid-state batteries with thin film cathode and thin film current collector, so that the interfacial region was within detection depth of soft XAS. This made in-operando characterization of oxidation states of transition metals near cathode|LLZO interface possible.

We have done three electrochemical tests to evaluate electrochemical stability at the NMC622|LLZO interface. We chose voltage cutoff for charging (4.3 V vs Li/Li^+) to be below inherent stability limit of NMC622. First, we did in-operando XAS during electrochemical cycling with charging voltage cutoff at 4.3 V vs Li/Li^+ to evaluate effect of electrochemical cycling on electrochemical degradation. Second, we did in-operando potentiostatic hold experiment at 4.3 V vs Li/Li^+ to evaluate reactivity between NMC622 and LLZO at high voltage. For both experiments, we tracked oxidation states of transition metals during experiments by continuously measuring XAS. Both in-operando experiments were done at room temperature. Finally, we did ex-situ XAS experiment on the cell cycled at 80 °C, to investigate effect of temperature on the electrochemical stability at the interface.

We could not observe electrochemical degradation from in-operando XAS during electrochemical cycling done at room temperature. Ni oxidized during charge, and reduced during discharge as expected. Co oxidation state increased slightly during charge and decreased slightly during discharge. Oxidation state of Mn did not change during cycling. Even after 300 cycles, reduced phases did not form.

Ni were reduced during in-operando potentiostatic hold experiment, which demonstrated electrochemical instability at NMC622|LLZO interface at high voltage. Co was slightly reduced during potentiostaic hold as well. Oxidation state of Mn remained same regardless of potentiostatic hold.

Cycling at 80 °C formed severely reduced phase. Ni^{2+} increased and Ni^{3+} decreased compared to the as prepared state after cycling. Co^{2+} formed after cycling. Oxidation state of Mn did not change.

Reduction of transition metals observed from potentiostatic hold and cycling at 80 °C matched well with our hypothesized electrochemical degradation pathway based on thermodynamics. The

result proves that there is an inherent electrochemical stability issue at NMC622|LLZO interface. In contrast, reduced phases were not observable from the in-operando XAS done at room temperature because of kinetic reason. There was not enough time to form an observable amount of reacted phases during cycling at room temperature due to slower reaction compared to experiment at 80 °C.

NiO and La_2CoMnO_6 are predicted by DFT as reaction products, and fits with XAS data indicating formation of phase with Ni^{2+} and Co^{2+}. NiO is an insulator,[138] but La_2MnCoO_6 is a semiconductor with low resistivity (0.01 Ω·cm) at room temperature.[139] Phase distribution and morphology of the degraded interface should be studied to evaluate whether it is passivating or non-passivating.

4.2. Experimental design and methods

LLZO pellets were prepared using same experimental methods discussed in section 3.2. We deposited 60 nm NMC622 on top of LLZO pellets by RF sputtering at room temperature (RF power: 100 W, $Ar:O_2$ ratio = 3:1). Samples were annealed in O_2 at 600 °C for 30 min after NMC622 deposition. 10 nm Pt was deposited on top of NMC622 as a current collector at room temperature (RF power: 100 W, pure Ar).

We prepared samples for in-operando XAS by depositing 38 nm WO_3 thin film anode (RF power: 90 W, $Ar:O_2$ = 9.3:2.7) and 90 nm W current collector (RF power: 100 W, pure Ar) on the opposite side of NMC622 by RF sputtering at room temperature. We used mask with ¼ inch to deposit WO_3 and W to avoid short circuit with the cathode side. We used lithium metal anode for the cell for ex-situ characterization. We prepared cell with lithium metal anode using same experimental methods discussed in section 3.2.

XAS was done at the 23-ID-2 (IOS) beamline, National Synchrotron Light Source II (NSLS-II) using partial fluorescence yield mode. We used special sample holder for in-operando XAS measurement. Figure *26* shows a schematic of the cell used for in-operando XAS, and a cell mounted on in-operando stage. Ex-situ XAS was done using standard sample stage.

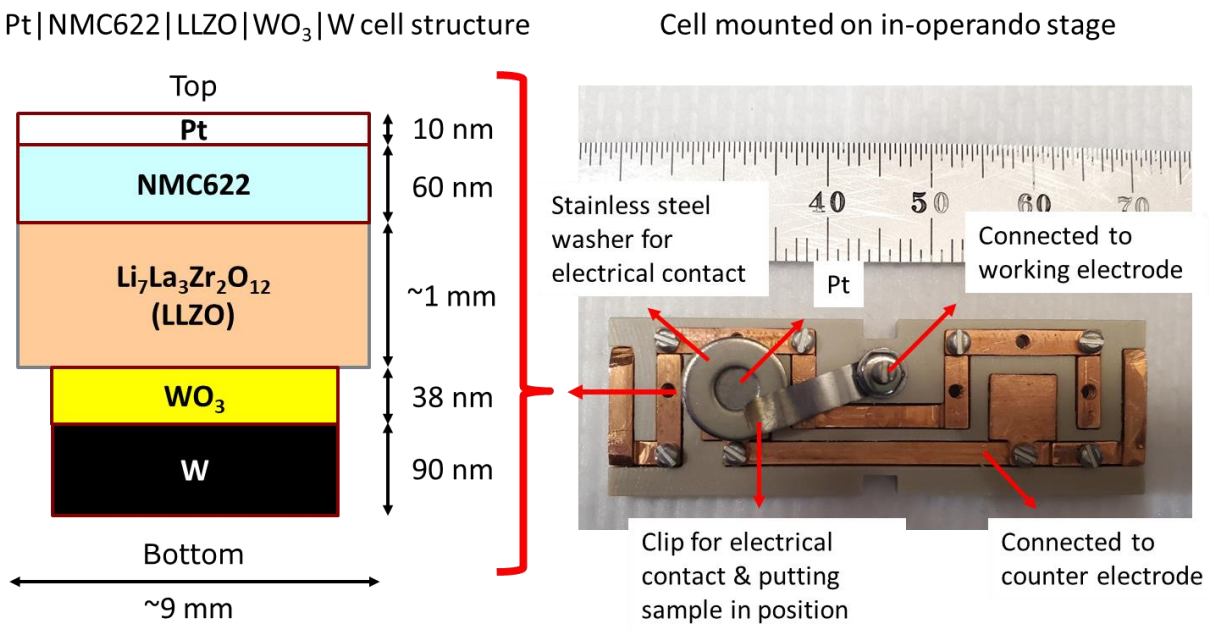

Figure 26 Structure of the in-operando cell, and the cell mounted on the sample stage for in-operando XAS

In-operando XAS during electrochemical cycling was done by measuring O K-edge, Ni L-edge & La M-edge, Co L-edge, Mn L-edge in sequence during electrochemical cycling with 4.3 V vs Li/Li^+ as charge voltage cutoff at room temperature. We measured XAS during each cycle, and after each cycle for 1^{st}-5^{th} cycles. Current used for 1^{st}-5^{th} cycles was 0.2 C. After 5th cycle, we increased current for cycling, and only measured XAS after certain numbers of cycling (10^{th}, 20^{th}, 30^{th}, 40^{th}, 50^{th}, 100^{th}, 200^{th}, 300^{th}). Currents for cycling were 1C for 6^{th}-10^{th} cycles, 2C for 11^{th}-50^{th} cycles, and 3C for 51^{th}-300^{th} cycles.

In-operando potentiostatic hold experiment was done by charging the cell up to 4.3 V vs Li/Li^+ using 1 C current, and then holding the potential at 4.3 V vs Li/Li^+ at room temperature. We acquired O K-edge, Ni L-edge & La M-edge, Co L-edge, Mn L-edge in sequence during potentiostatic hold.

The cell for ex-situ XAS was cycled between 3.0-4.3 V at 80 °C for 50 times with 5 C current. We acquired O K-edge, Ni L-edge & La M-edge, Co L-edge, Mn L-edge from the as prepared cell and the cycled cell.

4.3. Calculating the voltage on cathode side vs Li/Li^+ from the measured voltage of Pt| $LiNi_{0.6}Mn_{0.2}Co_{0.2}O_2$|LLZO|$WO_3$|W cell

We charged NMC622 cathode up to 4.3 V vs Li/Li^+ to avoid reaching inherent stability limit of the cathode. To calculate voltage on cathode during 1st charge, we used following equation.

$$V_{cathode}\ (Li_{1-x}Ni_{0.6}Mn_{0.2}Co_{0.2}O_2 \text{ vs } Li/Li^+) = V_{cell}\ (Li_{1-x}Ni_{0.6}Mn_{0.2}Co_{0.2}O_2 \text{ vs } Li_xWO_3) + V_{anode}\ (Li_xWO_3 \text{ vs } Li/Li^+) + \eta \text{ (overpotential correction)}$$

Figure 27 shows $V_{cathode}$, V_{cell}, V_{anode} corresponding to 1st charge from in-operando XAS during electrochemical cycling. V_{cell} is the cell voltage measured during charging. V_{anode} is the voltage on Li_xWO_3 anode vs Li/Li^+ during 1st lithiation of WO_3, which decreases as lithium content in the anode increases. We obtained the voltage profile for WO_3 lithiation from a separate experiment using W|WO_3|LLZO|Li cell. Correction for ohmic overpotential was needed since total resistance of W|WO_3|LLZO|Li cell was higher than Pt|$LiNi_{0.6}Mn_{0.2}Co_{0.2}O_2$|LLZO|$WO_3$|W cell. $V_{cathode}$ is the voltage of NMC622 vs Li/Li^+ during 1st charge, which was calculated by the equation.

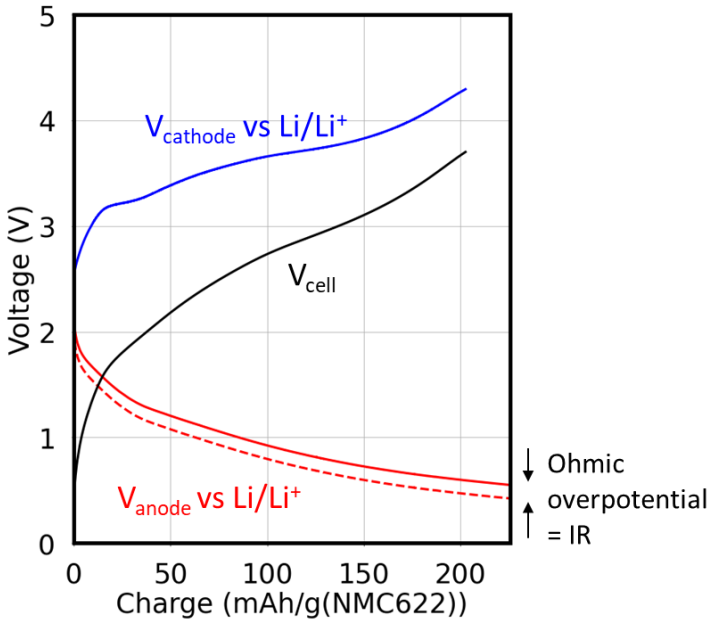

Figure 27 $V_{cathode}$ ($Li_{1-x}Ni_{0.6}Mn_{0.2}Co_{0.2}O_2$ vs Li/Li^+), V_{cell} ($Li_{1-x}Ni_{0.6}Mn_{0.2}Co_{0.2}O_2$ vs Li_xWO_3), V_{anode} (Li_xWO_3 vs Li/Li^+) corresponding to 1st charge of the cell used from in-operando XAS during electrochemical cycling. V_{cell} was measured from the Pt (10 nm)|$LiNi_{0.6}Mn_{0.2}Co_{0.2}O_2$ (60

nm)|LLZO|WO_3 (38 nm)|W (90 nm) cell. Vanode was obtained by cycling W (90 nm)|WO_3 (38 nm)|LLZO|Li cell

V_{cell} was 3.7 V when $V_{cathode}$ was 4.3 V for the 1st charge. We used 3.7 V (cell voltage) as charging cutoff for consequent cycling. Voltage cutoff for discharge was 0.5 V (cell voltage), which we chose to be close to open circuit voltage of the Pt| $LiNi_{0.6}Mn_{0.2}Co_{0.2}O_2$|LLZO|$WO_3$|W cell before cycling.

We used same strategy to calculate the cell voltage for potentiostatic hold experiment at 4.3 V vs Li/Li^+. V_{cell} was 3.6 V when $V_{cathode}$ was 4.3 V for the 1st charge. We held potential at 3.6 V (cell voltage) for potentiostatic hold experiment.

4.4. Electrochemical degradation at $LiNi_{0.6}Mn_{0.2}Co_{0.2}O_2$|LLZO interface by cycling up to 4.3 V vs Li/Li^+ at room temperature

We measured O K-edge, Ni $L_{2,3}$-edge, La $M_{4,5}$-edge, Co $L_{2,3}$-edge in sequence during cycling of Pt|$Ni_{0.6}Mn_{0.2}Co_{0.2}O_2$|LLZO|$WO_3$|W cell at room temperature. Figure 28 shows O K-edge data taken before cycling, during 1st cycle, and after 1st cycle, and corresponding voltage profile for 1st cycling. Lower energy feature of O K pre-edge increased during charging, while higher energy feature of O K pre-edge decreased. We observed opposite trend during discharging. Oxidation of transition metals bonded with oxygen increases lower energy feature of O K pre-edge.[50] Therefore, trend in O K pre-edge indicates transition metals oxidized during charge, and reduced during discharge.

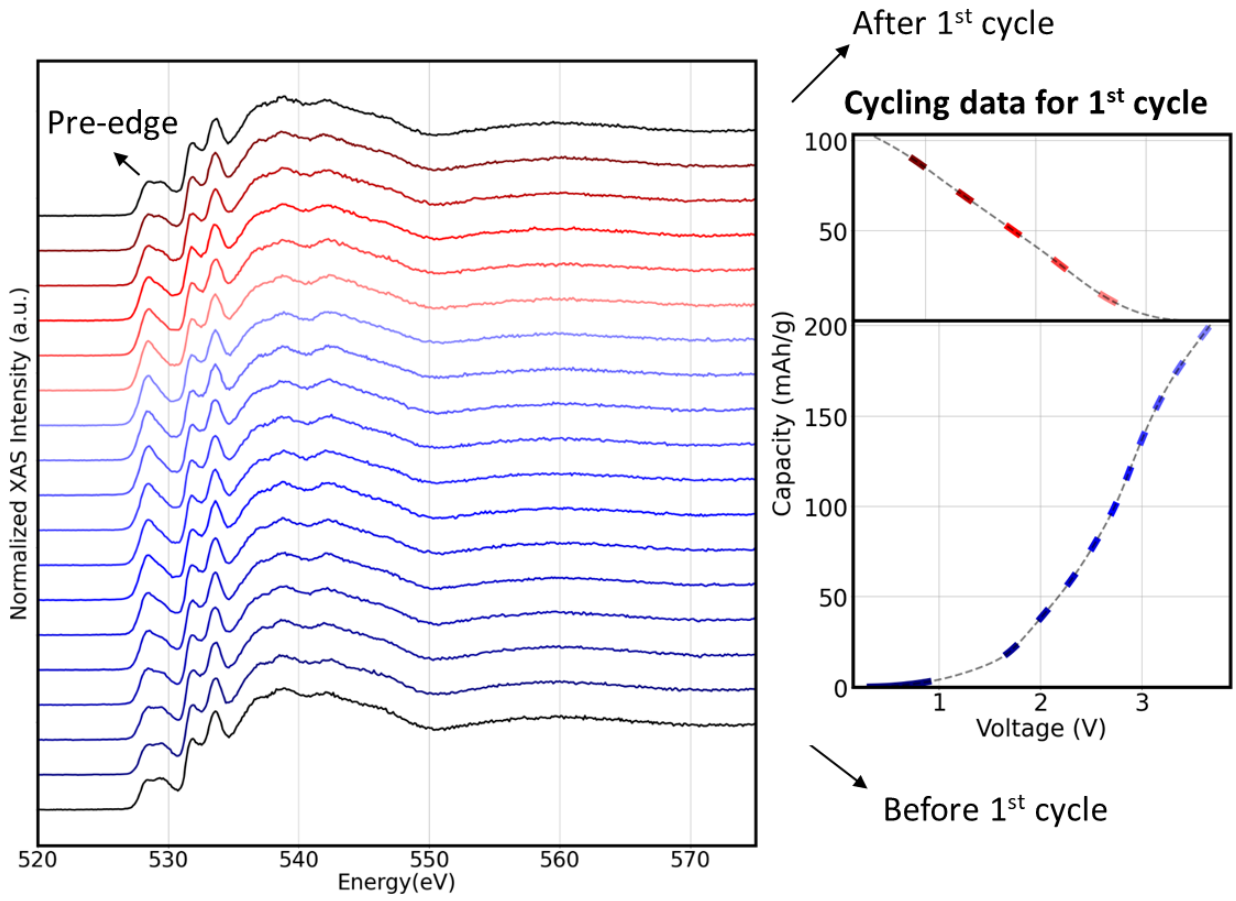

Figure 28 O K-edge X-ray Absorption Spectroscopy data (partial fluorescence yield (PFY)) for 1st cycle of Pt (10 nm)|NMC622 (60 nm)|LLZO|WO_3 (38 nm)|W (90 nm) cell. Spectra taken before 1st cycle, during 1st cycle, and after 1st cycle are shown. Each in-operando XAS data for O K-edge corresponds to a segment in the voltage profile marked with same color.

Ni oxidized during charging, and reduced during discharging. Intensity of high energy shoulder increased and low energy shoulder decreased for both Ni L_3-edge and L_2-edge during charging, which corresponds to oxidation of Ni (Figure *29*).[50,52,107] Opposite trend was observed during discharging because of Ni reduction. Ni was more oxidized compared to as prepared state after 1st cycle since 1st discharge capacity was lower than 1st charge capacity. This was due to isolation of NMC622 particles because of physical delamination at the NMC622|LLZO interface. Chemo-mechanical degradation at NMC622|LLZO will be discussed further in Chapter 5.

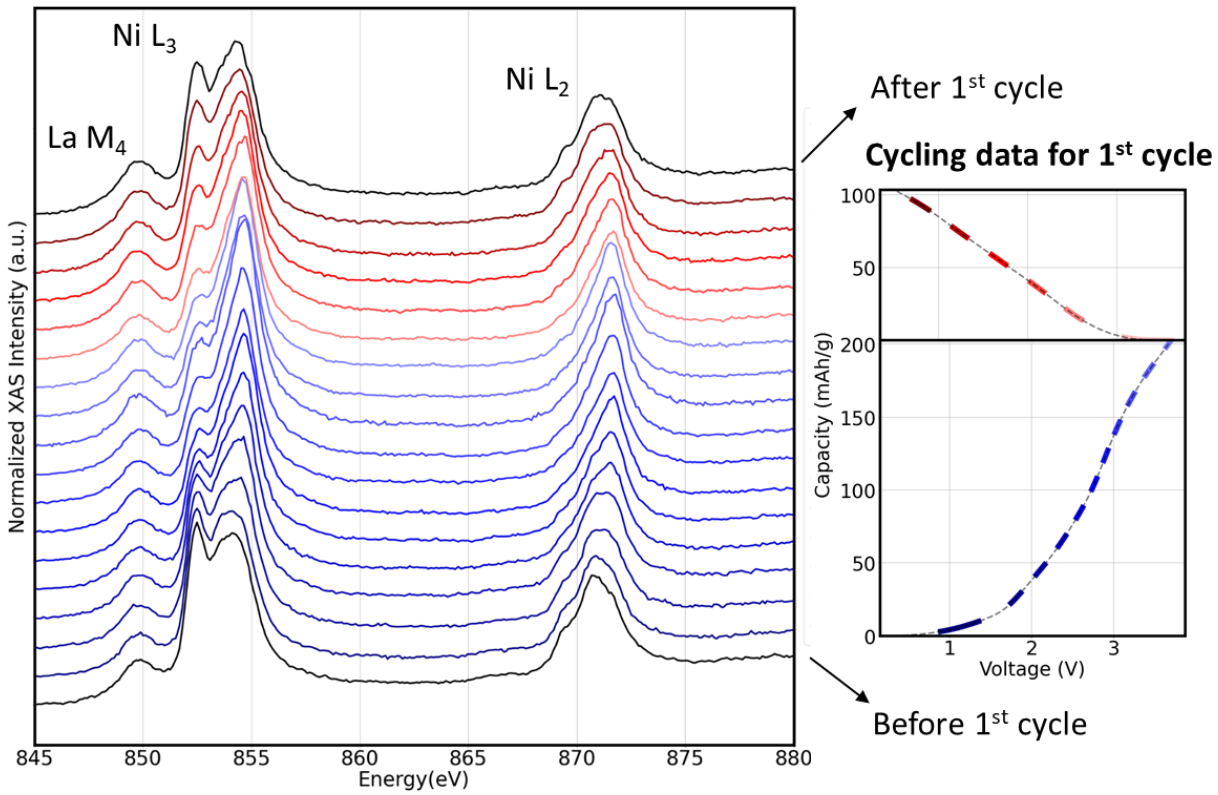

Figure 29 Ni $L_{2,3}$-edge and La M_4-edge X-ray Absorption Spectroscopy data (partial fluorescence yield (PFY)) for 1st cycle of Pt (10 nm)|NMC622 (60 nm)|LLZO|WO_3 (38 nm)|W (90 nm) cell. Spectra taken before 1st cycle, during 1st cycle, and after 1st cycle are shown. Each in-operando XAS data for Ni $L_{2,3}$-edge and La M_4-edge corresponds to a segment in the voltage profile marked with same color.

Notably, Low energy shoulder of L_2 edge disappeared at the end of charging, indicating severe oxidation compared to as prepared state. The shape of Ni L-edge at high voltage matched with γ-NiOOH, in which oxidation state of Ni is 3.48~3.68,[106,140,141] which suggested formation of Ni^{4+}.

Co oxidized during charging, and reduced during discharging, but change in oxidation state of Co was very small compared to Ni during 1st cycle (Figure 30). Both Co L_3-edge and Co L_2-edge shifts toward high energy during charge, and shifts toward low energy during discharge. However, unlike Ni $L_{2,3}$-edge, Co $L_{2,3}$-edge shape did not change drastically during cycling, and remained similar to $LaCoO_3$, in which Co oxidation state is +3.[53]

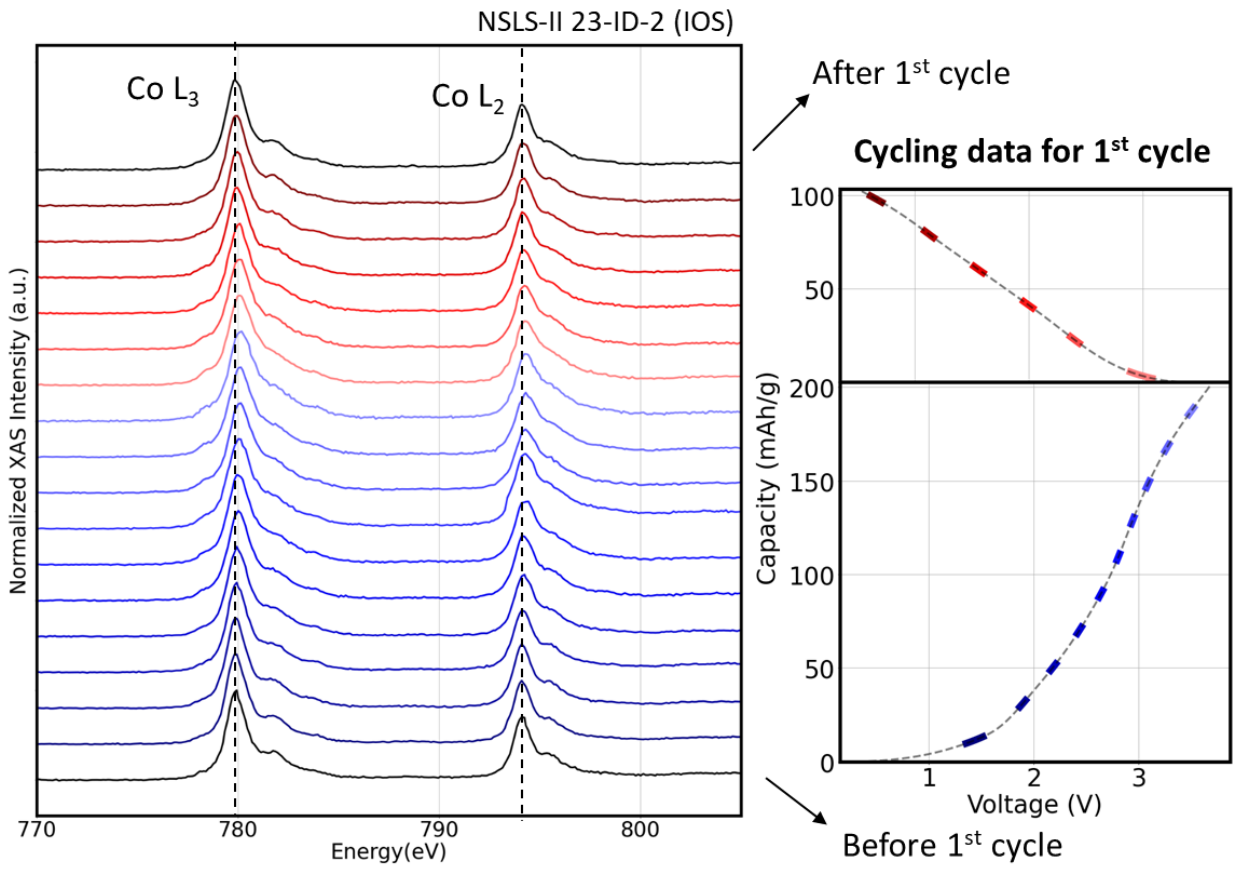

Figure 30 Co $L_{2,3}$-edge X-ray Absorption Spectroscopy data (partial fluorescence yield (PFY)) for 1st cycle of Pt (10 nm)|NMC622 (60 nm)|LLZO|WO_3 (38 nm)|W (90 nm) cell. Spectra takens before 1st cycle, during 1st cycle, and after 1st cycle are shown. Each in-operando XAS data for Co $L_{2,3}$-edge corresponds to a segment in the voltage profile marked with same color.

Oxidation state of Mn did not change during charging and discharging. Mn L-edge shape was same before cycle, during 1st cycle, and after 1st cycle, which matched with Mn^{4+} (Figure 31).[59]

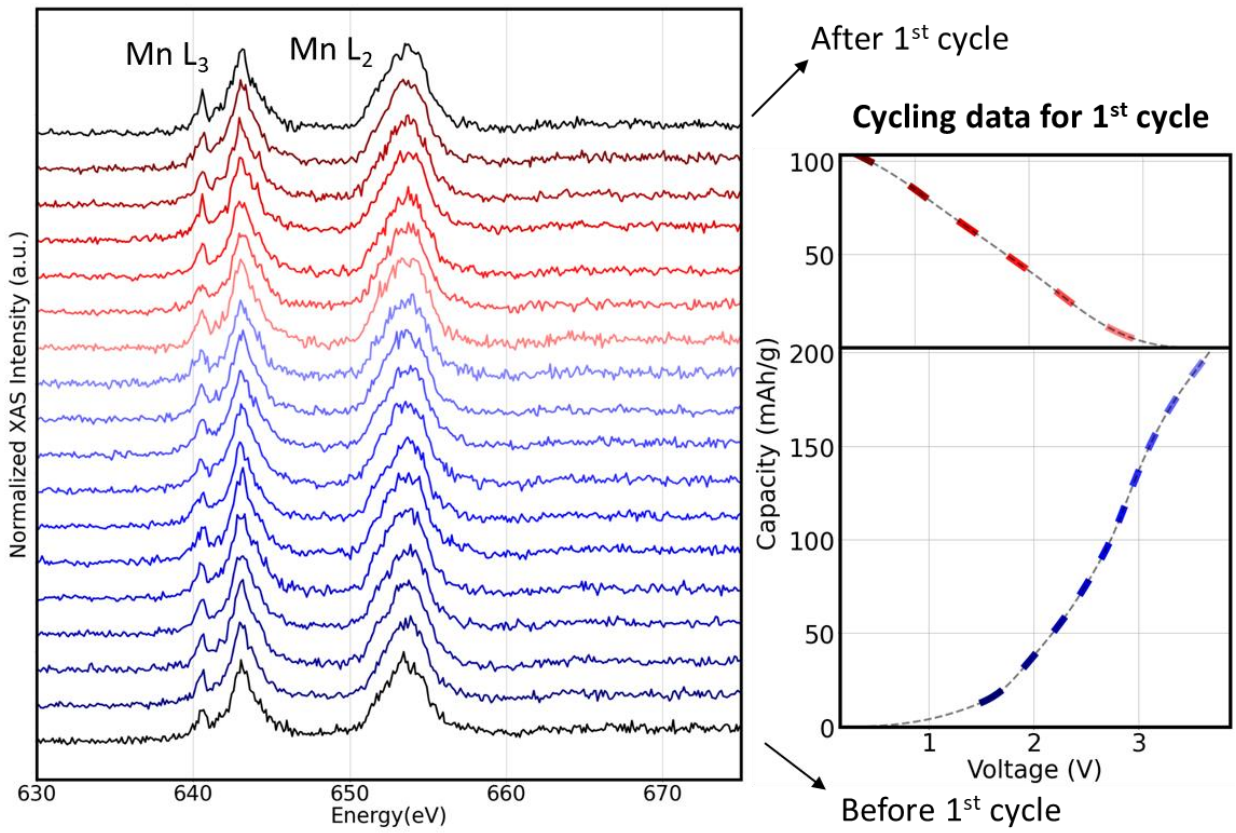

Figure 31 Mn $L_{2,3}$-edge X-ray Absorption Spectroscopy data (partial fluorescence yield (PFY)) for 1st cycle of Pt (10 nm)|NMC622 (60 nm)|LLZO|WO_3 (38 nm)|W (90 nm) cell. Spectra taken before 1st cycle, during 1st cycle, and after 1st cycle are shown. Each in-operando XAS data for Mn $L_{2,3}$-edge corresponds to a segment in the voltage profile marked with same color.

We hypothesized growth of secondary phases at the interface with reduced transition metals after cycling due to instability of the interface at high voltage during cycling. However, we could not observe the reduction of transition metals after 1st cycle. We did XAS after multiple cycling to see whether the predicted electrochemical degradation became severe enough to be characterizable. Figure 32 shows charging and discharging curves for 300 cycles. Current applied for 1st-5th cycle was 0.2 C, 2nd-5th cycle was 1 C, 11th-50th cycle was 2 C, 51st-300th cycle was 3 C.

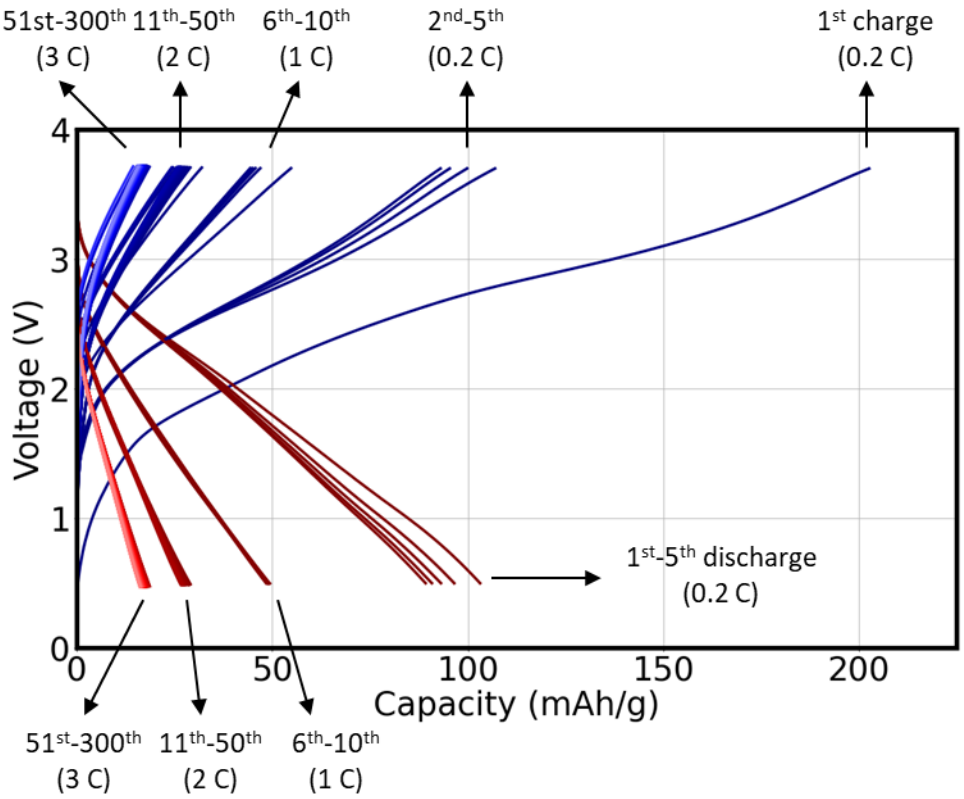

Figure 32 Chaging curves and discharging curves for Pt (10 nm)|$LiNi_{0.6}Mn_{0.2}Co_{0.2}O_2$ (60 nm)|LLZO|WO_3 (38 nm)|W (90 nm) cell cycled for 300 times.

Steep capacity decrease between 1st charge between 2nd charge indicates severe degradation during 1st cycle. This is from chemo-mechanical degradation at the NMC622|LLZO interface, which will be discussed further in chapter 5. Capacity decrease after 5th, 10th, 50th cycles is due to increased overpotential because of increased current applied during cycling. Both charge capacities and discharge capacities decreased gradually as cycling number increased.

Figure 33 shows O K-edge, Ni L-edge and La M-edge, Co L-edge, Mn L-edge for as prepared sample and after 1st-5th cycle. Figure 34 shows O K-edge Ni L-edge and La M-edge, Co L-edge, Mn L-edge for as prepared sample, and after 1st, 200th, 300th cycle.

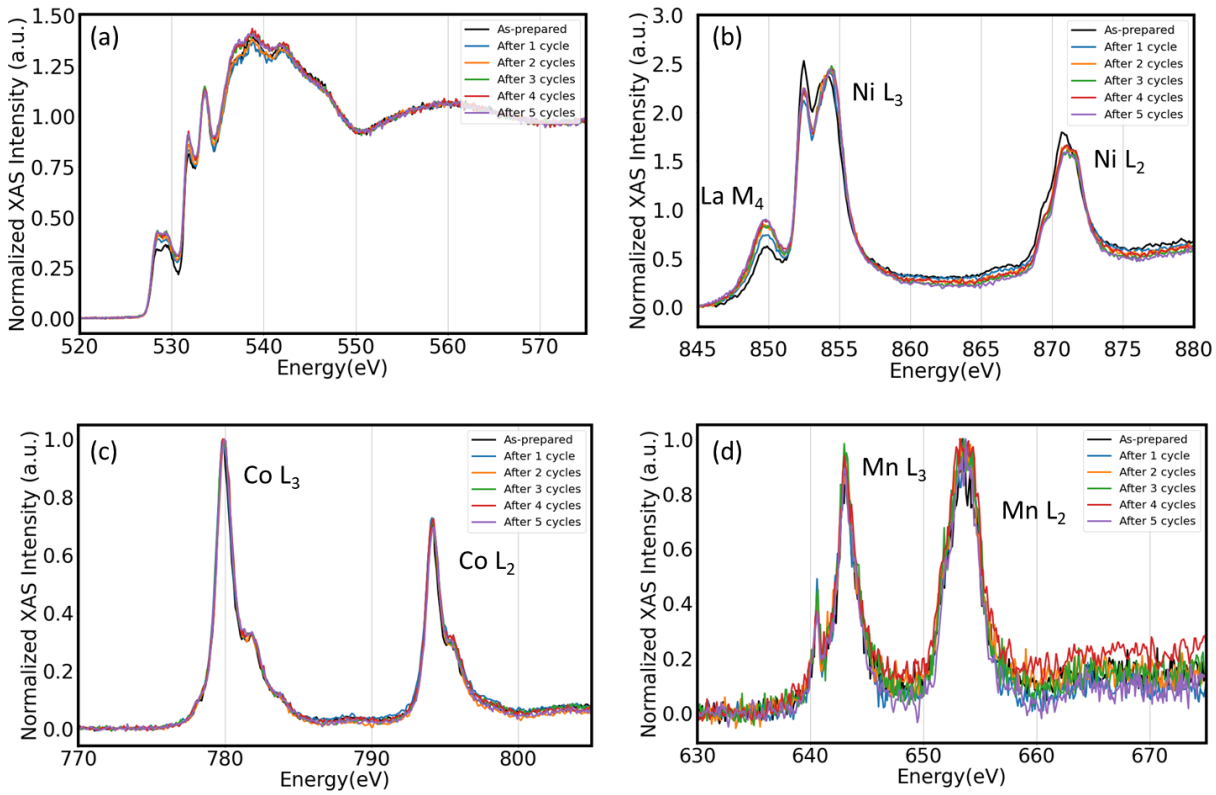

Figure 33 O K-edge, Ni $L_{2,3}$-edge and La M_4-edge, Co $L_{2,3}$-edge, Mn $L_{2,3}$-edge X-ray Absorption Spectroscopy data (partial fluorescence yield (PFY)) for Pt (10 nm)|NMC622 (60 nm)|LLZO|WO_3 (38 nm)|W (90 nm) cell before cycling, and after 1^{st}-5^{th} cycle

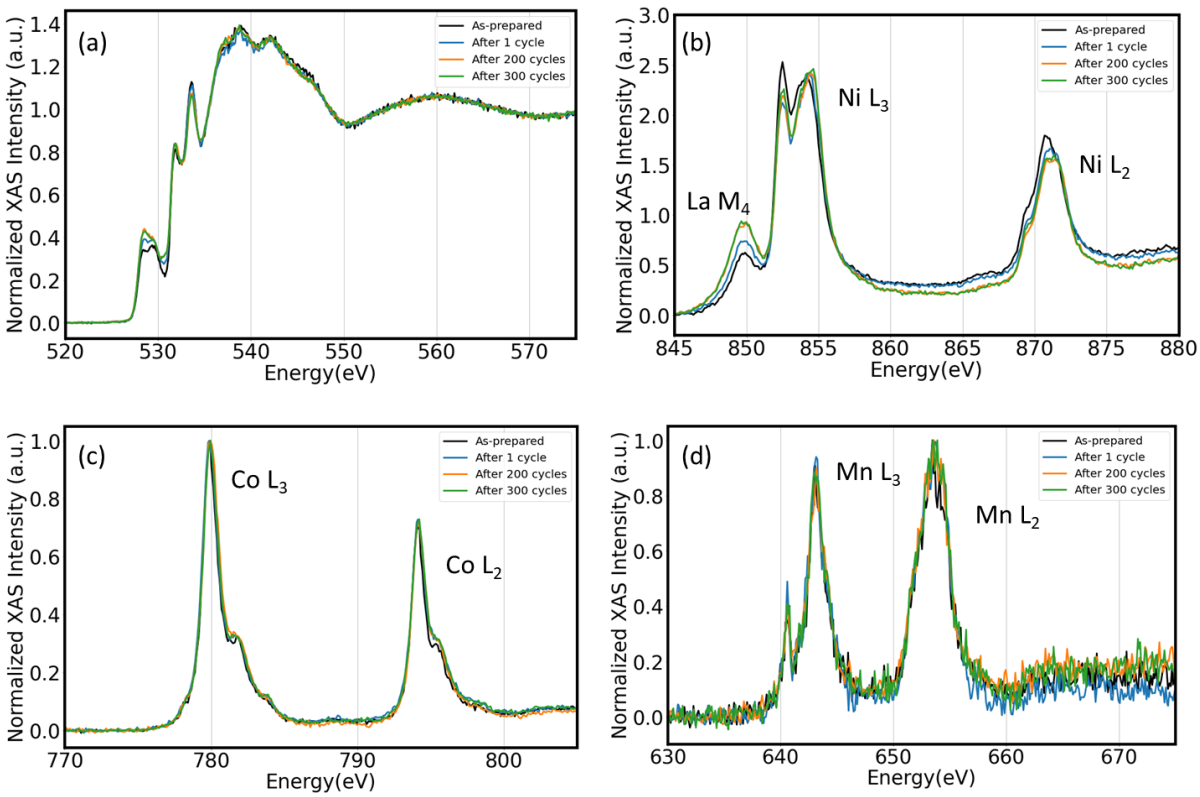

Figure 34 O K-edge, Ni $L_{2,3}$-edge and La M_4-edge, Co $L_{2,3}$-edge, Mn $L_{2,3}$-edge X-ray Absorption Spectroscopy data (partial fluorescence yield (PFY)) for Pt (10 nm)|NMC622 (60 nm)|LLZO|WO_3 (38 nm)|W (90 nm) cell before cycling, and after 1st, 200th, 300th cycle

Intensity of pre-edge feature of O K-edge increased as cycling number increased, and lower energy feature of the pre-edge became stronger compared to high energy feature (Figure 33 (a), Figure 34 (a)). This corresponds to the increase of oxidation sate of transition metals bonded to oxygen as cycling number increased. Ni oxidizes compared to as prepared state after 1 cycle, which is shown by decrease of low energy feature of Ni L_3-edge and increase of high energy feature of Ni L_3-edge (Figure 33 (b)). Oxidation state change of Ni is no longer obvious from the 2nd cycle from Ni L-edge data (Figure 33 (b), Figure 34 (b)). Oxidation state of Co and Mn did not change after cycling (Figure 33 (c-d), Figure 34 (c-d))

Oxidation state increase of transition metals is opposite from what we expected from the predicted electrochemical degradation mechanism. The discrepancy could have originated from isolation of NMC622 particles due to chemo-mechanical degradation during cycling, which we will discuss further in Chapter 5. NMC622 particle which was disconnected from other

components during cycling remains in charged state (oxidized state) even when we discharge the cell. Therefore, average oxidation state of transition metals increases by chemo-mechanical degradation. Increase of La M-edge signal intensity compared to Ni L-edge with cycling number increase justifies chemo-mechanical degradation in the sample (Figure 33 (b), Figure 34 (b)). Crack formation exposed more LLZO on the surface of the cell, which caused increase of La M-edge signal intensity versus Ni L-edge. As more NMC622 became isolated due to chemo-mechanical degradation as cycling number increased, average oxidation state of transition metals in NMC622 increased.

4.5. Electrochemical degradation at $LiNi_{0.6}Mn_{0.2}Co_{0.2}O_2$|LLZO interface by potentiostatic hold at 4.3 V vs Li/Li^+ at room temperature

We measured O K-edge, Ni $L_{2,3}$-edge, La $M_{4,5}$-edge, Co $L_{2,3}$-edge, Mn $L_{2,3}$-edge in sequence during potentiostatic hold to evaluate electrochemical degradation at NMC622|LLZO interface at 4.3 V vs Li/Li^+. Pre-edge feature of the O K-edge, which originates from oxygen-transition metal bond, was stronger after charging compared to the state before cycling (Figure 35). The shape and intensity of the pre-edge remained similar during potentiostatic hold.

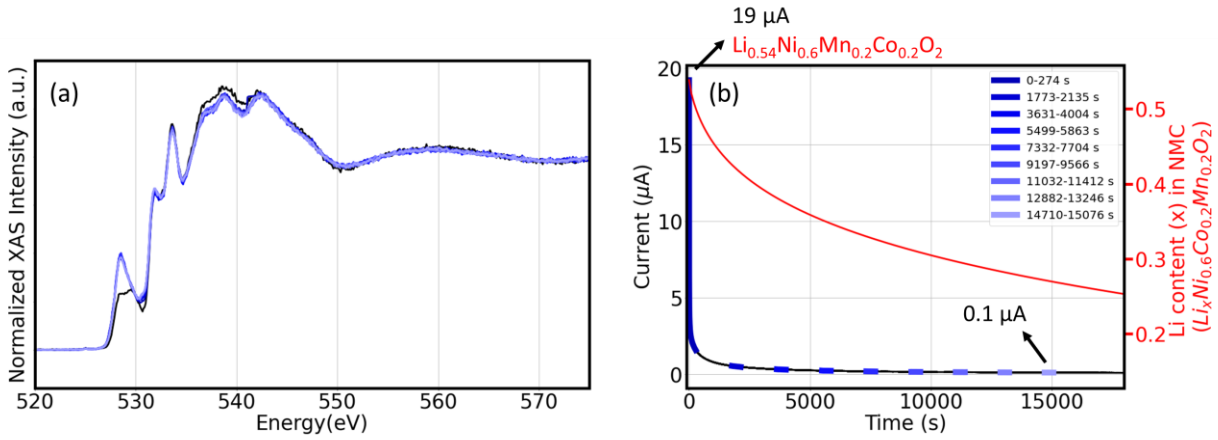

Figure 35 O K-edge X-ray Absorption Spectroscopy data (partial fluorescence yield (PFY)) for potentiostatic hold at 4.3 V vs Li/Li^+ of Pt (10 nm)|NMC622 (60 nm)|LLZO|WO_3 (38 nm)|W (90 nm) cell. Each in-operando XAS data for O K-edge corresponds to a segment in the current profile marked with same color.

Ni reduced during potentiostatic hold. Low energy feature of Ni $L_{2,3}$-edge increased and high energy feature of Ni $L_{2,3}$-edge decreased (Figure 36). The voltage applied for potentiostatic hold (4.3 V vs Li/Li^+) was lower than the inherent stability limits of NMC622 reported by previous studies (4.55 V vs Li/Li^+ (Renfrew et al.[137]), 4.7 V vs Li/Li^+ (Jung et al.[120])) Therefore, Ni reduction shown during pontentiostaic hold originated from electrochemical reaction at NMC622|LLZO interface.

The reduction of Ni was not severe during potentiostatic hold. Shape of Ni L-edge stayed similar to γ-NiOOH (Oxidation state of Ni: 3.48~3.68)[106,140,141] through the potentiostatic hold. Small oxidation state change of Ni matches with our finding on O K-edge where we did not observe clear change in pre-edge related to transition metal reduction. Limited oxygen diffusion at room temperature could have kinetically inhibited the reaction.

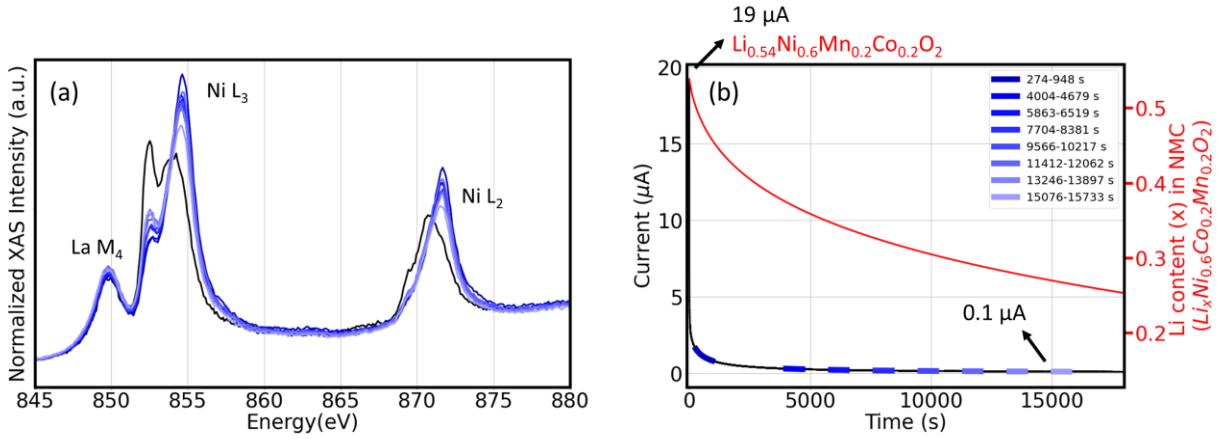

Figure 36 Ni $L_{2,3}$-edge and La M_4-edge X-ray Absorption Spectroscopy data (partial fluorescence yield (PFY)) for potentiostatic hold at 4.3 V vs Li/Li^+ of Pt (10 nm)|NMC622 (60 nm)|LLZO|WO_3 (38 nm)|W (90 nm) cell. Each in-operando XAS data for Ni $L_{2,3}$-edge and La M_4-edge corresponds to a segment in the current profile marked with same color.

Co L-edge shifted toward higher energy after charging, and it gradually returned to its original energy during potentiostatic hold. Oxidation state of Co remained close to +3, and indicators for Co^{4+} formation were not found.

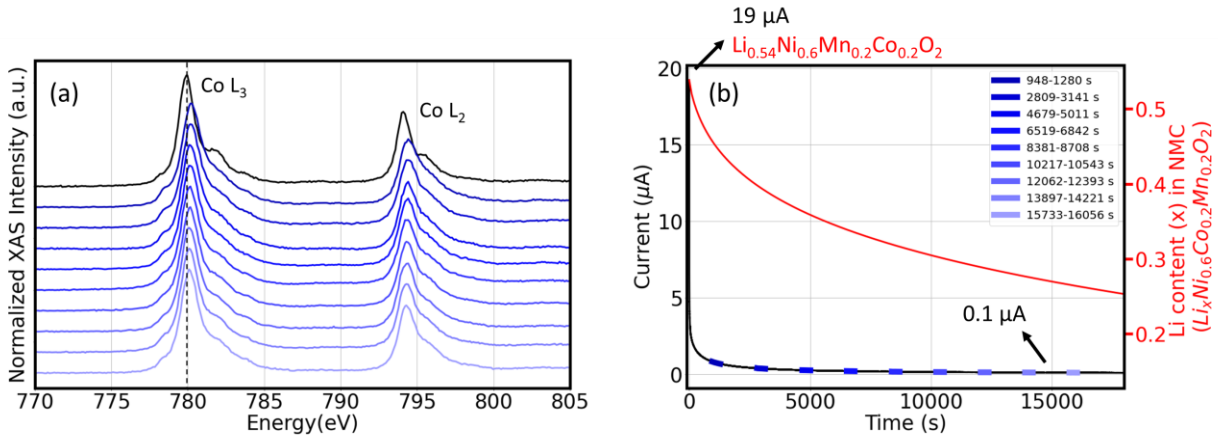

Figure 37 Co $L_{2,3}$-edge X-ray Absorption Spectroscopy data (partial fluorescence yield (PFY)) for potentiostatic hold at 4.3 V vs Li/Li^+ of Pt (10 nm)|NMC622 (60 nm)|LLZO|WO_3 (38 nm)|W (90 nm) cell. Each in-operando XAS data for Co $L_{2,3}$-edge corresponds to a segment in the current profile marked with same color.

Oxidation state of Mn stayed +4 after charging, and during potentiostatic hold. Mn was not redox active.

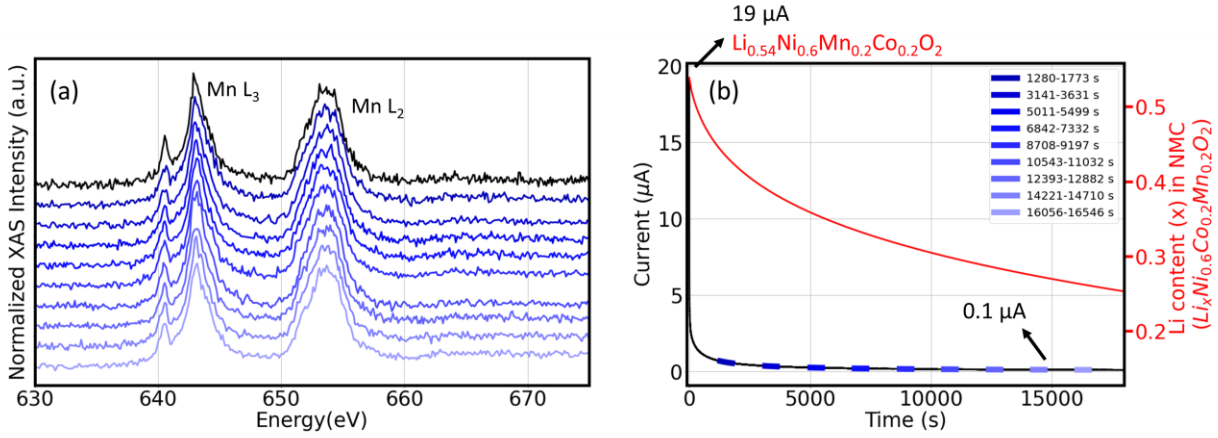

Figure 38 Mn $L_{2,3}$-edge X-ray Absorption Spectroscopy data (partial fluorescence yield (PFY)) for potentiostatic hold at 4.3 V vs Li/Li^+ of Pt (10 nm)|NMC622 (60 nm)|LLZO|WO_3 (38 nm)|W (90 nm) cell. Each in-operando XAS data for Mn $L_{2,3}$-edge corresponds to a segment in the current profile marked with same color.

4.6. Electrochemical degradation at $LiNi_{0.6}Mn_{0.2}Co_{0.2}O_2$|LLZO interface by cycling up to 4.3 V vs Li/Li^+ at 80 °C

We did ex-situ XAS on Pt|$Ni_{0.6}Mn_{0.2}Co_{0.2}O_2$|LLZO|Li cell cycled at 80 °C between 3.0-4.3 V vs Li/Li^+ to study the effect of higher temperature on degradation at cathode|LLZO interface. Figure 39 shows charging curves and discharging curves 1st-50th cycle.

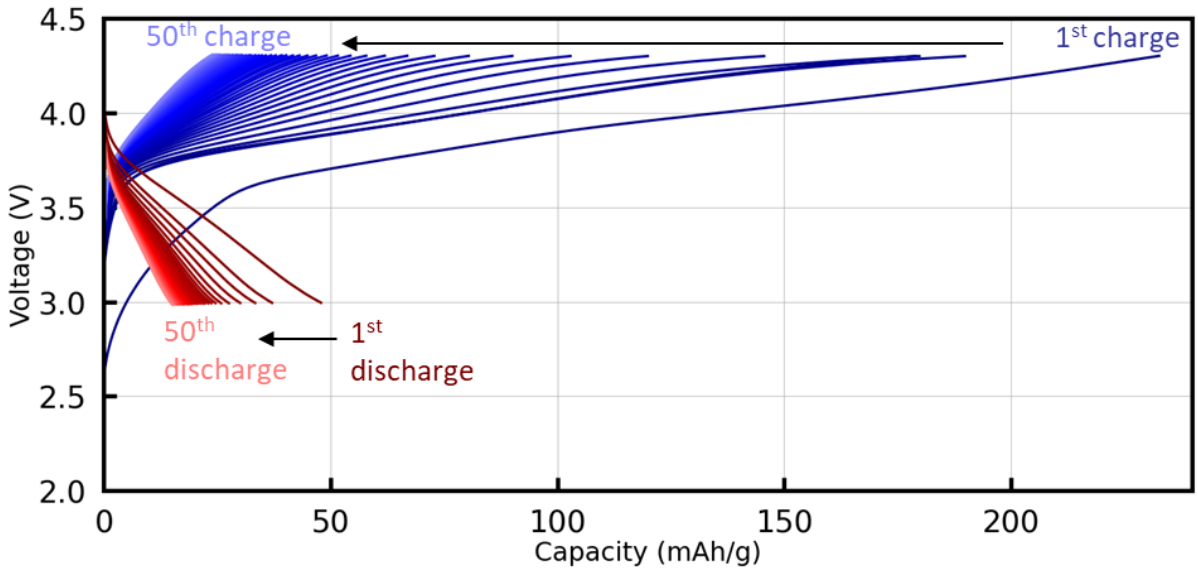

Figure 39 Chaging curves and discharging curves for Pt (10 nm)|$LiNi_{0.6}Mn_{0.2}Co_{0.2}O_2$ (60 nm)|$Li_7La_3Zr_2O_{12}$ |Li cell cycled between 3.0-4.3 V for 50 times at 80 °C with 5 C current

1st charge capacity was 232 mAh/g whereas 1st discharge capacity was 47 mAh/g. Both charge capacity and discharge capacity decreased gradually as cycling number increased. The decrease in capacities originated from overpotential increase in the cell. The differential capacity plot reveals voltages for electrochemical reactions in the cell during cycling. Features for phase transitions for H1→M and M→H2 appeared, as reported by previous studies on cycling of layered oxide cathodes.[119,120] As cycling number increased, the feature corresponds to H1→M phase transition during charging shifted toward higher voltage because of higher overpotential in the cell.

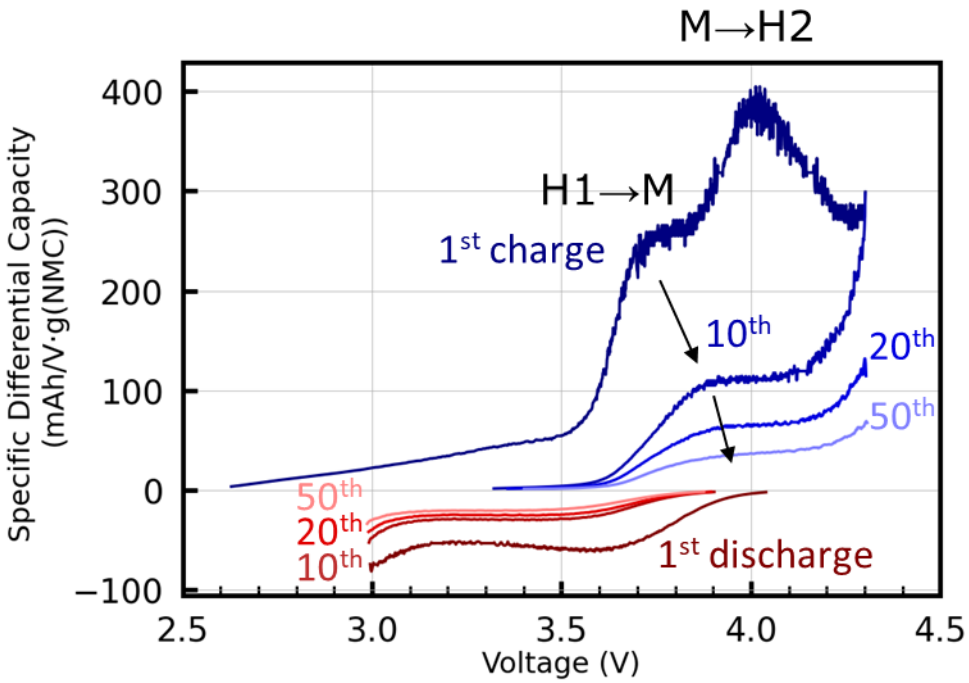

Figure 40 Differential capacity plot obtained from cycling curves in Figure 39. Processed data for 1st, 10th, 20th, 50th cycles are shown.

In order to investigate the origin of overpotential increase, we performed XAS to check whether there had been observable chemical degradation at the interface. Figure 41 compares O K-edge, Ni L-edge and La M-edge, Co L-edge, Mn L-edge for the sample before cycling, and the sample cycled at 80 °C for 50 times with 5 C current.

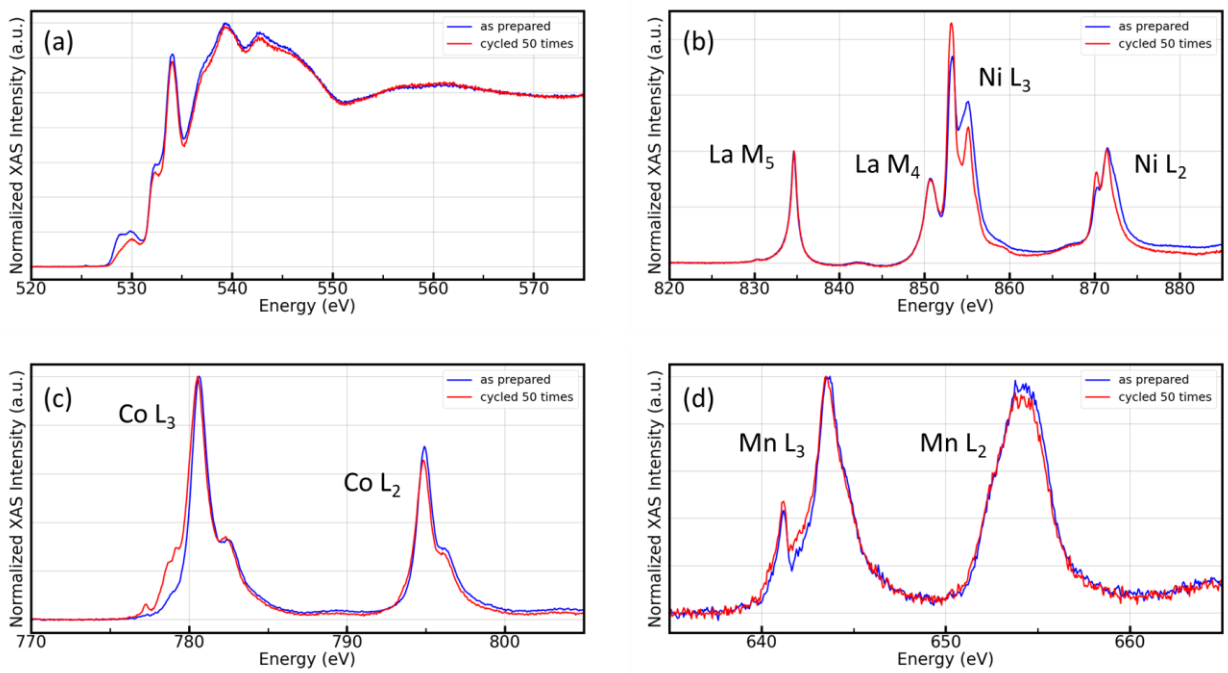

Figure 41 O K-edge, Ni $L_{2,3}$-edge and La M_4-edge, Co $L_{2,3}$-edge, Mn $L_{2,3}$-edge X-ray Absorption Spectroscopy data (partial fluorescence yield (PFY)) for Pt (10 nm)|NMC622 (60 nm)|LLZO|Li cell before cycling, and after cycling 50 times at 80 °C

Pre-edge of O K-edge showed decrease of transition metals with higher oxidation state, and increase of transition metals with lower oxidation state after cycling (Figure 41 (a)). Pre-edge intensity of O K-edge decreased after cycling 50 times. Lower energy pre-edge feature intensity, which corresponds to oxygen bond with transition metals with higher oxidation states,[50] decreased more compared to higher energy pre-energy feature. Both Ni and Co reduced after cycling. Low energy feature of both Ni L_3 and L_2 edge increased while high energy feature decreased (Figure 41 (b)). The intensity change indicates reduction of Ni.[50,52,107] A new feature at 777.5 eV appeared in Co L-edge data after cycling (Figure 41 (c)). The feature proves formation of reduced phase with Co^{2+} (High Spin).[111,112] Oxidation states of Mn were +4 before and after cycling. Shape of Mn L-edge remained same (Figure 41 (d)).

Reduced phases with Ni^{2+} and Co^{2+} formed after cycling at 80 °C. This is different from results from in-operando XAS during electrochemical cycling at room temperature, in which reduced phases were not found. Cycling at higher temperature could have expedited chemical reaction between cathode and LLZO. We did Grazing Incidence XRD on the sample before cycling, and

the sample cycled at 80 °C to characterize reduced phases formed due to secondary reaction between NMC622 and LLZO (Figure 42). The samples were sealed in glove box with plastic holder to avoid air exposure during XRD characterization. The bar chart below XRD corresponds to reference XRD peaks for NMC622 (ICDD: 00-066-0854), LLZO (ICDD: 00-063-0174), and Pt (ICDD: 00-004-0802).

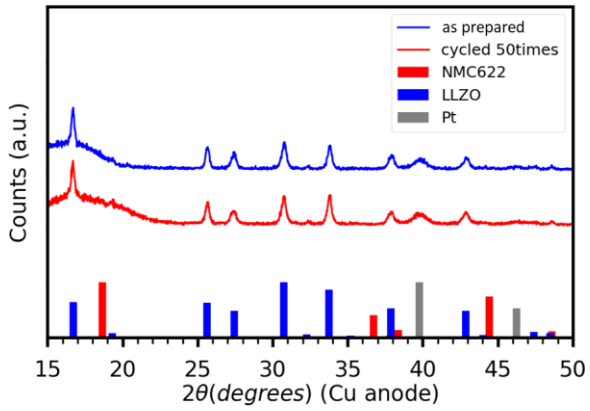

Figure 42 Grazing incidence XRD (Grazing angle: 0.5°) for Pt (10 nm)|NMC622 (60 nm)|LLZO|Li cell before cycling, and after cycling 50 times at 80 °C

Plastic holder used for XRD characterization caused broad feature around 17°. Peaks for LLZO and Pt were in both as prepared sample and the sample after cycling. In contrast, peaks for NMC622 were not found in both samples due to their low intensity. Secondary phases with reduced transitional metals (Ni^{2+}, Co^{2+}) were amorphous. Intensities of broad feature at low angles increased after cycling, but peaks for additional secondary phases did not appear.

4.7. Discussion

We expected electrochemical degradation at NMC622|LLZO based on limited oxidation limit of LLZO. We hypothesized oxidation of LLZO and reduction of NMC622 by oxygen transfer from NMC622 to LLZO. As a result of the electrochemical degradation, we expected to observe reduced transition metal in NMC622.

Experiment results from potentiostatic hold experiment at 4.3 V vs Li/Li^+ and cycling at 80 °C matched well with our hypothesized degradation pathway. Ni reduced during potentiostatic hold experiment at 4.3 V vs Li/Li^+, and reduced phases (Ni^{2+}, Co^{2+}) formed after cycling experiment

at 80 °C. The findings prove that the electrochemical degradation at the NMC622|LLZO interface is thermodynamically spontaneous.

In contrast to cycling experiment at 80 °C, reduced phases were not observable from in-operando XAS during electrochemical cycling at room temperature. The discrepancy originates from slow reaction kinetics at room temperature. Reduction of transition metals in NMC622 requires oxygen migration out of the NMC622 lattice. Therefore, we expect slower reaction at room temperature compared to at 80 °C due to slower oxygen transport. For this reason, there were not enough reaction products to be observable from in-operando XAS during electrochemical cycling.

Transition metals in NMC622 reduced due to electrochemical degradation at NMC622|LLZO interface since charge voltage cutoff (4.3 V vs Li/Li^+) was lower than inherent stability limit of NMC622. Delithiated NMC622 could decompose into reduced phases on their own by losing oxygen from the lattice when applied voltage is over its stability limit. However, experimentally found onset voltage for the oxygen evolution were higher than the charge voltage cutoff used in our study. Renfrew et al.[137] and Jung et al.[120] reported oxygen evolution above 4.55 V and 4.7 V respectively. Since the charge voltage cutoff used in the study is lower than those values, we exclude the possibility of self-degradation of NMC622.

Experimental findings for electrochemical degradation from our work matches well with DFT predicted decomposition with the exception of computationally predicted Li_2NiO_3. Nolan et al. predicted formation of Li_2NiO_3, Li_2ZrO_3, ZrO_2, NiO, La_2MnCoO_6 from reaction between $Li_{0.5}Ni_{0.6}Mn_{0.2}Co_{0.2}O_2$ and LLZO according to their DFT calculation.[18] NiO and La_2MnCoO_6 matches well with formation of reduced phases (Ni^{2+}, Co^{2+}) that we observed from the cell cycled at 80 °C. On the other hand, Li_2NiO_3 does not match with experimental findings since oxidation state of Ni is +4 in the phase. Li_2NiO_3 is only stable at oxidizing condition,[142] which was not considered during DFT prediction. Li_2NiO_3 requires oxygen environment with extremely high pressure (P_{O_2} = 150 bar) for synthesis.[143] Therefore, we believe formation of Li_2NiO_3 is unlikely in our experimental condition, in which cell was sealed in a glove box with oxygen level below 1 ppm.

Phase characterization of the reaction products at NMC622|LLZO interface formed by electrochemical degradation is not conclusive since XRD did not show peaks for crystalline phases. Considering DFT predicted phases (Li_2NiO_3, Li_2ZrO_3, ZrO_2, NiO, La_2MnCoO_6) and our XAS characterization indicating formation of reduced phases, we suggest that NiO and La_2CoMnO_6 formed at the interface. Formation of rock salt phase (NiO) matches with studies of Lithium Nickel Manganese Cobalt oxide degradation in liquid electrolytes.[50,144] Formation of La_2MnCoO_6 double perovskite structure is similar to what we observed in Chapter 2 and Chapter 3 from thermal degradation between NMC622 and LLZO ($La(Ni,Co)O_3$ in air, La_2NiO_4 and La_2CoO_4 in CO_2).

Degraded phase between cathode and electrolyte should ideally be electronically insulating phase to inhibit further electrochemical degradation. NiO is an insulator,[138] but La_2MnCoO_6 is a semiconductor with 0.01 Ω·cm resistivity at room temperature.[139] Therefore, phase distribution of secondary phases at the NMC622|LLZO should be analyzed to evaluate whether the electrochemical degradation forms passivating or non-passivating layer. The finding will indicate whether NMC622|LLZO requires additional protective interlayer due to formation of non-passivating layer, or it is not necessary.

4.8. Conclusion

In this section, we identified products of electrochemical degradation at NMC622|LLZO. Limited oxidation stability of LLZO caused electrochemical degradation at NMC622|LLZO. We hypothesized oxidation of LLZO and reduction of NMC622 occurred by oxygen transfer from NMC622 to LLZO. We designed a cell with thin film cathode and thin film electrode, so that in-operando characterization of NMC622|LLZO was possible with soft XAS. We confirmed the hypothesis by observation of Ni reduction during potentiostiatc hold, and reduced phases (Ni^{2+}, Co^{2+}) formation from the cell cycled at 80 °C. Both charge and discharge capacities decreased due to overpotential increase by formation of reduced phases. Considering DFT prediction and XAS result, we expect the formed phases to be NiO and La_2MnCoO_6. As NiO is an insulator while La_2MnCoO_6 is a semiconductor, further characterization of phase distribution is needed to investigate whether passivating interface had formed.

In-operando XAS during electrochemical cycling done at room temperature did not show reduced phases, indicating the electrochemical degradation could be kinetically inhibited during cycling at relatively low temperature. Therefore, we suggest cycling at room temperature to minimize electrochemical degradation at the interface.

5. Chemo-mechanical stability at $LiNi_{0.6}Mn_{0.2}Co_{0.2}O_2|Li_7La_3Zr_2O_{12}$ interface

5.1. Introduction

In chapter 4, we have discussed electrochemical stability issues at NMC622|LLZO interface. We focused on reduction of transition metals at the interface, and formation of secondary phases. In this chapter, we discuss chemo-mechanical stability issues at the interface stemming from lattice parameter changes of NMC622 during cycling.

Stress between crystallites in polycrystalline NMC622 and stress at NMC622|LLZO interface during cycling are inevitable since lattice parameters of NMC622 depends on lithiation content. Lattice parameter changes during cycling causes stress between crystallites with crystal orientation mismatch, which causes crack at the interface. The issue is inherent in layered oxide cathodes, and happens in both liquid electrolytes environment[145–147] and solid electrolyte environment.[36] We calculated intergranular stress between two NMC622 grains and compared it with fracture stress of NMC622 to predict mechanical stabilities at the interface.

According to the model by Ming-Yuan et al, crack approaching the interface between two elastic materials could either propagate through the interface or cause delamination by being deflected at the interface.[148] The model by Ming-Yuan et al. compares tendencies for crack propagation and crack deflection at the interface by comparing energy loss and gain for each pathway. We used mechanical properties for NMC622, LLZO and at NMC622|LLZO interface to predict the behavior of crack near NMC622|LLZO interface.

Both intergranular crack and delamination cause irreversible capacity loss during cycling as they disconnect lithium conduction pathway. Therefore, understanding the nature of the mechanical degradation is important. We used model system with thin film cathode to study mechanical degradation at the NMC622|LLZO interface. We used focused ion milling to expose the NMC622|LLZO interface, and characterized it with Scanning Electronic Microscopy (SEM). We compared as prepared cell and the cell cycled 50 times between 3.0 V-4.3 V at 80 °C. Thickness of cathodes of the cell for studying mechanical degradation (600 nm) was thicker than cells for studying chemical degradation (60 nm, 100 nm). We chose thicker cathode so that we could

observe outcomes of mechanical degradation such as cracks and delamination with the available magnification of Scanning Electronic Microscopy.

Estimated strain at the interface between two grains with different crystallographic orientation from our calculation reached up to ~5 GPa during charging. The stress was much bigger than fracture strength (~50 MPa) of lithium nickel cobalt manganese oxide,[149] so we expected intergranular crack between NMC622 grains. Considering mechanical properties of NMC622 and LLZO, we predicted intergranular crack in NMC622 approaching NMC622|LLZO interface to be deflected, forming crack between NMC622 and LLZO. Our prediction based on fracture mechanics matched well with experimental findings. Both intergranular crack and delamination were found in the cross-sectional image taken by FIB-SEM. Charge capacity dropped significantly from 121 mAh/g (1st charge capacity) to 58 mAh/g (2nd charge capacity), which demonstrated the detrimental effect of chemo-mechanical degradation on cell performance.

5.2. Experimental design and methods

We prepared LLZO pellets by same experimental steps discussed in section 3.2. We deposited 600 nm thick NMC622 on top of LLZO pellets by RF sputtering. RF power and Ar:O_2 ratio used for the experiment were 100 W and 3:1 respectively. Deposition was done at room temperature. Samples were post-annealed at 600 C for 30 min in O_2. 60 nm Pt current collector was deposited on top of NMC622 at room temperature. We used lithium metal anode for the cell for ex-situ characterization. We prepared cells with lithium metal anode using same experimental methods discussed in section 3.2. The cell was cycled between 3.0-4.3 V for 50 times. Current for cycling was 5 C, and temperature during cycling was 80 °C. We used FIB-SEM (Focused Ion Beam Scanning Electron Microscope) to characterize the interface. We characterized the cell without cycling, and the cell after cycling for 50 times.

5.3. Prediction of chemo-mechanical degradation at $LiNi_{0.6}Mn_{0.2}Co_{0.2}O_2$|LLZO interface

Intergranular crack between NMC622 grains originates from anisotropic lattice parameter changes of NMC622 as it delithiates. Crystal structure of NMC622 changes from H1 to H2 as its lithium content decreases to 60% compared to fully lithiated state.[33] This causes lattice parameter

to change from 2.86 Å to 2.81 Å in a-axis direction, and 14.227 Å to 14.375 Å in c-axis direction.[33] Intergranular strain and stress between two adjacent gains with different crystallographic directions are as following.

$$\varepsilon\ (Intergranular\ strain) = \frac{14.375/14.227}{2.81/2.86} - 1 = 0.0283$$

$$\sigma\ (Intergranular\ stress) = E\varepsilon = \ 177.5\ GPa\ \times 0.0283 = 5.041\ GPa$$

(E: Elastic modulus of Lithium Nickel Manganese Cobalt Oxide = 177.5 GPa)[150]

Calculated intergranular stress (5.041 GPa) for NMC622 was similar to the value calculated by Xue et al. (~6 GPa),[144] in which authors studied stress between NMC811 grains. The intergranular stress is much bigger than fracture stress (~50 MPa)[149] of Lithium Nickel Manganese Cobalt Oxide. Therefore, we expect formation of intergranular crack during delithiation.

Intergranular crack between NMC622 grains deflects at the NMC622|LLZO interface, which causes delamination of NMC622. Ming-Yuan et al. calculated conditions for crack propagation and crack deflection at the interface of two elastic materials, when crack formed in one of the materials reaches the interface.[148] Authors derived a curve that separates the conditions for crack propagation and crack deflection by calculating strain energy release rate for each pathway. Figure 43 shows the curve, which we replotted from the work from Shi et al.,[151] in which the authors used the model to investigate crack formation within Silicon anode. We calculated mechanical properties corresponding to NMC622|LLZO interface to evaluate mechanical stability, and marked the datapoint on Figure 43 with red dot.

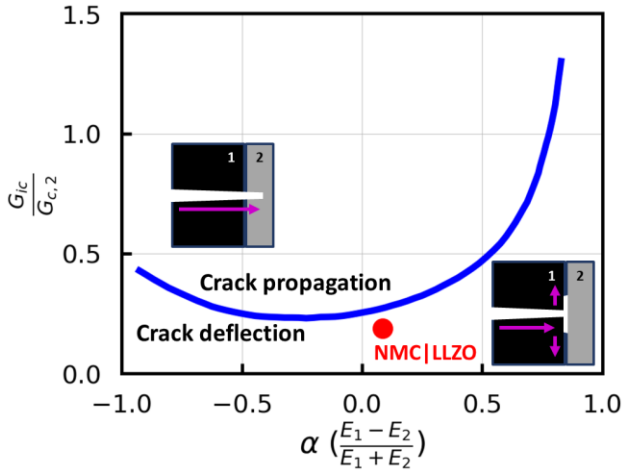

Figure 43 Curve separating regions for crack propagation and crack deflection through the interface between two materials. G_{ic}: Critical strain energy release rate between material 1 and material 2, $G_{c,2}$: Critical strain energy release rate of material 2, G_d: Energy release rate of crack deflected at the interface between material 1 and material 2, G_p: Energy release rate of crack propagating into material 2. The curve was replotted from the work by Shi et al.[151]

When material 1 and material 2 are adjacent to each other and crack formed in material 1 reaches the interface between material 1 and material 2, the condition for crack deflection at the interface is as following.

$$\frac{G_{ic}}{G_{c,2}} < \frac{G_d}{G_p}$$

(G_{ic}: Critical strain energy release rate between material 1 and material 2

$G_{c,2}$: Critical strain energy release rate of material 2

G_d: Energy release rate of crack deflected at the interface between material 1 and material 2

G_p: Energy release rate of crack propagating into material 2)

G_d/G_p is a function of dimensionless variable α ($\alpha = \frac{E_1-E_2}{E_1+E_2}$), where E_1 is elastic modulus of material 1 and E_2 is elastic modulus of material 2). The crack from material 1 will propagate into material 2 when it reaches the interface if following inequality holds.

$$\frac{G_{ic}}{G_{c,2}} > \frac{G_d}{G_p}$$

Elastic modulus of Lithium Nickel Cobalt Manganese Oxide is 177.5 GPa,[150] and elastic modulus of LLZO is 149.8 Gpa.[152] We used 1.25 MPa $\sqrt{m}$ for the fracture toughness (K_{IC}) of LLZO, which is the value corresponding to polycrystalline LLZO.[152] The critical energy release rate depends on fracture toughness and elastic modulus of the material.[153]

$$G_c = \frac{{K_{IC}}^2}{E}$$

(G_c: critical energy release rate, K_{IC}: fracture toughness, E: elastic modulus)

From the formula, critical energy release rate for LLZO is 10.4 J/m^2.

Sum of surface energy densities for new surfaces formed due to crack is equal to critical energy release rate.[154] Therefore, critical strain energy release rate at NMC622|LLZO interface is as following.

$$G_{ic} = \gamma_{NMC622} + \gamma_{LLZO}$$

(G_{ic}: critical energy release rate at NMC622|LLZO interface,

γ_{NMC622}: surface energy density of NMC622,

γ_{LLZO}: surface energy density of LLZO)

We used surface energies corresponding to most stable surfaces for each material to calculate critical energy release rate at NMC622|LLZO surface. We used surface energy of $LiCoO_2$ to estimate γ_{NMC622}. $(10\bar{1}4)$ surface of $LiCoO_2$ has the lowest surface energy, which is 1.048 J/m^2.[155] As for LLZO, (100) surface and (110) surface had lowest surface energies of 0.84 J/m^2 and 0.85 J/m^2 respectively.[156] From these values, we estimated critical energy release rate at NMC622|LLZO interface to ~2 J/m^2. α and $\frac{G_{ic}}{G_{c,2}}$ for NMC622|LLZO interface are as following.

$$\alpha = \frac{E_{NMC622} - E_{LLZO}}{E_{NMC622} + E_{LLZO}} = \frac{177.5\ GPa - 149.8\ GPa}{177.5\ GPa + 149.8\ GPa} = 0.085$$

$$\frac{G_{ic}}{G_{c,2}} = \frac{2\ J/m^2}{10.4 J/m^2} = 0.19$$

The corresponding point for $(\alpha, \frac{G_{ic}}{G_{c,2}})$ is below the curve dividing crack deflection and crack propagation conditions (Figure 43). Therefore, the mechanical analysis predicts the intergranular crack between NMC622 grains to be deflected at NMC622|LLZO interface, leading to delamination of the NMC622.

5.4. Chemo-mechanical degradation at $LiNi_{0.6}Mn_{0.2}Co_{0.2}O_2$|LLZO interface by cycling up to 4.3 V vs Li/Li^+

Figure 44 shows charging curves and discharging curves for cycling Pt|NMC622|LLZO|Li cell. Cycling was done at 80 °C. with 5 C current.

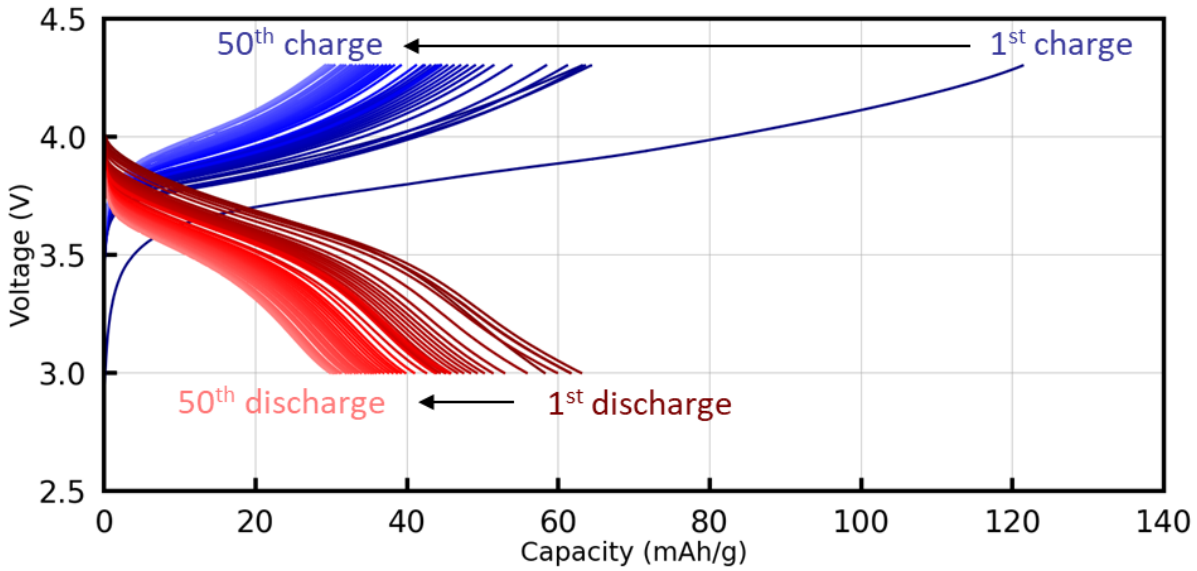

Figure 44 Chaging curves and discharging curves for Pt (60 nm)|$LiNi_{0.6}Mn_{0.2}Co_{0.2}O_2$ (600 nm)|LLZO|Li cell cycled between 3.0-4.3 V for 50 times at 80 °C with 5 C current

Charge capacity and discharge capacities for 1st cycle were 121 mAh/g and 58 mAh/g. Capacities were comparable to previous study on All-solid-state Lithium Ion batteries with similar configuration (NMC622|Li_3BO_3|LLZO|Li).[87] Capacity dropped significantly between 1st charge (121 mAh/g) and 2nd charge (58 mAh/g). Steep capacity drop between 1st charge and 2nd charge was consistent with previous work on $LiCoO_2$|LLZO|Li all solid battery with Li_3BO_3 and $In_{2(1-x)}Sn_{2x}O_3$ interlayers, in which the authors attributed it to crack formation at cathode|electrolyte interface during 1st cycling.[123]

In order to investigate chemo-mechanical degradation near the interface, we exposed cross-section of the as prepared sample and the sample cycled at 80 °C for 50 times between 3.0-4.3 V by Focused Ion Milling (FIB). The cross-sectional images (Figure 45 (a)-(d)) were taken using Scanning Electron Microscope (SEM).

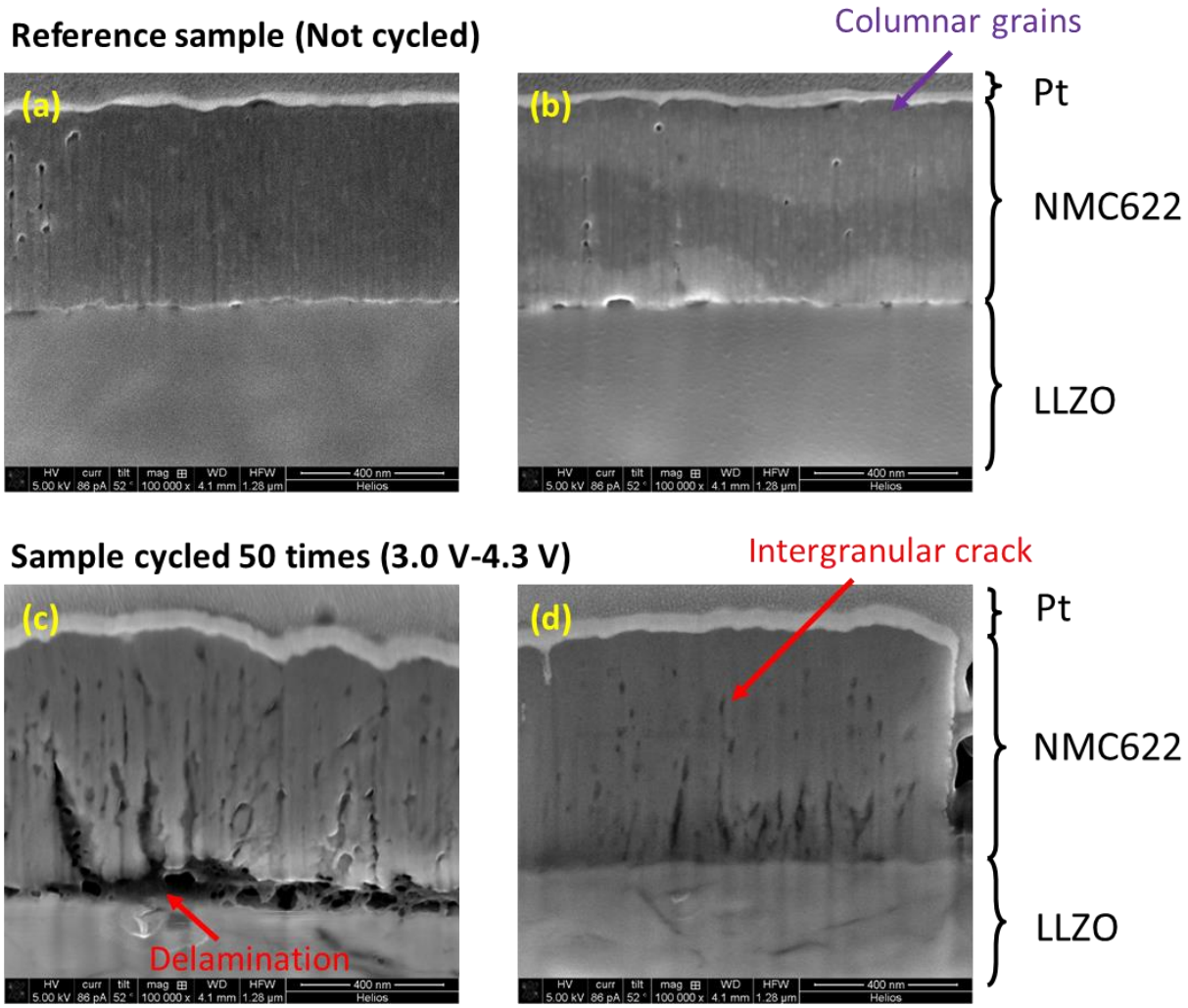

Figure 45 Cross sectional images for Pt (60 nm)|NMC622 (600 nm)|LLZO|Li cell (a-b) before cycling, and (c-d) after cycling 50 times at 80 °C. Images taken by using FIB-SEM

NMC622 thin film had columnar grains, as reported by previous study on annealed layered oxide cathode film.[157] Intergranular cracks formed within NMC622 thin film, and delamination happened at the NMC622|LLZO interface after cycling. Both intergranular crack and delamination matched with mechanical prediction in the previous section (Chapter 5.3) Isolation

of cathode particles due to crack formation made lithium transfer between NMC622 and LLZO impossible. This caused capacity drop.

5.5. Discussion

We could observe both intergranular crack in NMC622 film and delamination at NMC622|LLZO interface from the cycled sample, which matched well with our prediction based on fracture mechanics. Significant difference between 1st charge capacity and 2nd charge capacity indicates severe degradation during 1st cycle. We expect this was due to high stress within the material during 1st charge. Intergranular stress, which is the main driver of the chemo-mechanical degradation, depends on the lattice parameter changes of NMC622 as its lithium content changes. The lattice parameter change of NMC622 was largest during 1st charge, since the charge capacity was largest. Therefore, the most severe chemo-mechanical degradation occurred during 1st cycle, leading to much smaller 2nd charge capacity compared to 1st charge capacity.

The delamination is the major contributor for capacity loss, as it disconnects the lithium conduction pathway between NMC622 and LLZO. Therefore, avoiding delamination during cycling is crucial for minimizing cell performance degradation. Since the lattice parameter changes of cathodes are the origin of the chemo-mechanical degradation, using cathode with small volume changes would improve stabilities at the interface. This could be achieved by layered oxide cathodes with different ratio between transition metals. Lattice volumes of $LiNi_{0.3}Mn_{0.1}Co_{0.6}O_2$ and $LiNi_{0.2}Mn_{0.1}Co_{0.7}O_2$ changes < 1% when they were charged up to 4.4 V vs Li/Li^+.[158] Using cathodes with less lattice parameter changes will improve chemo-mechanical stability.

Using composite cathodes with flexible polymer improves chemo-mechanical stability. He et al. compared solid batteries based on LLZO with and without succinonitrile (SCN) in the composite cathode.[159] Coulombic efficiency for the cell with SCN (95.8%) was much higher than the one without SCN (14.6%). Stable contact upon cycling due to introduction of flexible polymer into composite cathode improved coulombic efficiency.

Delamination at the interface can be avoided by engineering mechanical properties near the cathode|solid electrolyte interface. According to the model by Ming-Yuan et al.[148] that we

exploited to predict behavior of crack at the interface, delamination between two materials can be avoided in following condition.

$$\frac{G_{ic}}{G_{c,2}} > \frac{G_d}{G_p}$$

If the inequality holds at cathode|solid electrolyte interface, the intergranular crack in cathode will not be deflected at the interface, but will propagate into solid electrolyte. Therefore, the interface between cathode and solid electrolyte remains in contact during cycling. We hypothesize that this will give better cyclability since there won't be steep capacity decrease due to delamination. Selecting cathode and solid electrolyte pair with proper mechanical properties is necessary for the inequality to hold.

5.6. Conclusion

In this section, we performed mechanical analysis based on fracture mechanics to predict chemo-mechanical degradation within NMC622 and at NMC622|LLZO interface during cycling, and experimentally demonstrated the degradation by FIB-SEM images. Intergranular stress between NMC622 grains was bigger than fracture strength of NMC622, so we expected intergranular crack. We expected intergranular crack to be deflected at NMC622|LLZO interface and delaminate the film according to the mechanical model based on critical energy release rates. Both intergranular crack and delamination was observed from cycled sample in FIB-SEM images, which demonstrated validity of our mechanical model. Charge capacity decreased steeply after 1st cycle, demonstrating severe chemo-mechanical degradation during 1st cycle. Using cathode with less lattice parameter changes to decrease stress at the interface, or composite cathodes with flexible polymers could improve chemo-mechanical stabilities. Engineering mechanical properties near the interface can also mitigate delamination by changing behavior of intergranular crack within cathode when it reaches cathode|solid electrolyte interface.

6. Conclusions

6.1. Summary

In this thesis, we have studied interfacial degradation pathways between cathodes and solid electrolyte during both manufacture stage (sintering needed for good contact, effect of different gas environments during sintering) and operation stage (electrochemical cycling and potentiostatic hold) With this approach, we provided comprehensive understanding on the interfacial stability issues at cathode|solid electrolyte interface. We selected $LiCoO_2$ and $LiNi_{0.6}Mn_{0.2}Co_{0.2}O_2$ (NMC622) as cathodes, and $Li_7La_3Zr_2O_{12}$ (LLZO) as solid electrolyte in this thesis. We used model system with thin film cathodes for experiment to characterize interfacial regions without the needs of destructive techniques.

Chapter 2 and Chapter 3 discussed thermal stability issues at NMC622|LLZO interface, First, we identified formation of Li_2CO_3 and other delithiated phases ($La(Ni,Co)O_3$ and $La_2Zr_2O_7$ at high temperature (700 °C) at the interface between NMC622|LLZO after annealing in air (Chapter 2). Formation of secondary phases degraded the electrochemical properties at the NMC622|LLZO interface as it increased interfacial resistance over 100 times compared to the as prepared interface. From the result, we hypothesized that delithiation of the interface by reaction with gas (formation of Li_2CO_3 by reacting with CO_2 in air) and subsequent formation of delithiated phases are key mechanisms for thermal degradation at cathode|LLZO interface. To test this hypothesis, we systematically studied chemical reactivity in different gas environments (O_2, N_2, humidified O_2, CO_2) (Chapter 3). We studied effect of H_2O (g) and CO_2 (g) as they can both delithate the interface by forming LiOH and Li_2CO_3 respectively. Reaction under CO_2 was most severe, showing formation of Li_2CO_3 and various other delithiated phases. Existence of H_2O also led to degradation, but its effect was less detrimental compared to CO_2. In contrast, the interface remained chemically stable in O_2 and N_2 environment. Especially, annealing in O_2 was most ideal as it lowered interfacial resistance at NMC622|LLZO interface by one order of magnitude compared to as prepared state. The results proved our former hypothesis since removing gas species (H_2O (g), CO_2) that could potentially delithiate the interface from the gas environment during sintering gave chemically stable interface.

Chapter 4 and Chapter 5 discussed electrochemical and chemo-mechanical issues at NMC622|LLZO interface. We discussed electrochemical instability at the interface by in-

operando XAS characterization during potentiostatic hold and electrochemical cycling. (Chapter 4) Ni^{4+}, which formed at high voltage in NMC622, reduced during potentiostatic hold (4.3 V vs Li/Li^{+}). This was due to electrochemical instability at NMC622|LLZO interface coming from limited oxidation stability of LLZO. Electrochemical cycling at room temperature did now show reduction of transition metals, whereas reduced phases with Ni^{2+} and Co^{2+} after cycling at 80 °C. This shows the electrochemical degradation can be kinetically inhibited when the cycling temperature is low. Apart from electrochemical degradation, NMC622|LLZO interface also suffered from chemo-mechanical degradation due to cycling (Chapter 5). We predicted intergranular crack with NMC622 and delamination of NMC622 film from the interface based on mechanical model. As predicted, we observed both intergranular cracks between NNC622 and delamination at NMC622|LLZO interface from the cycled sample. Mechanical degradation at the interface decreased capacity as it isolated NMC622 from other parts of the cell.

6.2. Outlook

In this thesis we provided comprehensive understanding on both thermal and electrochemical degradation mechanism at layered oxide cathode|LLZO interface by using model system consisting thin film cathode. The usage of model system enabled precise understanding of the degradation mechanism at the interface as we could use X-ray Absorption Spectroscopy. Based on our findings from the thesis, we suggest following future research directions.

6.2.1 Kinetics of thermal degradation at cathode|solid electrolyte interface

Understanding the reaction kinetics for thermal degradation at the cathode|solid electrolyte is important to choose appropriate dwell time for sintering. Increasing dwell time at high temperature will improve contact between solid components. However, increasing dwell time will also form more secondary phases if there is thermal instability at the interface. If the secondary phases have low Li-ion conductivities, this will deteriorate performance of the cell. Therefore, we expect there will be a optimized dwell time which will give good contact between components, while having low amount of secondary phases.

In chapter 2 and chapter 3, we demonstrated that we could characterize chemical degradation at cathode|solid electrolyte interface and correlate it to charge transfer properties at the interface by using model systems with thin film cathode. By using same sample design and do chemical

characterization during in-situ heating in controlled gas environments, tracking secondary phase formation during heat treatment would be possible.

Correlation of findings from chemical characterization with interfacial resistance at the interface will provide full guideline for choosing appropriate sintering conditions (temperature, gas environment, and time).

6.2.2. Heterogeneous electrochemical and chemo-mechanical degradation at cathode|solid electrolyte interface

Charged states in layered oxide cathode is not homogeneous during cycling. Tian et al. showed oxidation state of Ni was heterogeneous at the surface of NMC622 particles when they were charged by using 2D X-ray Absorption Spectroscopy.[160] As we discussed in Chapter 4, reduction of Ni^{4+} along with LLZO oxidation is a key step for electrochemical degradation at NMC622|LLZO interface. Since oxidation state of Ni was heterogeneous, we expect inhomogeneous electrochemical degradation at the interface.

Since charged states are heterogenous, applied stress on the system due to lattice parameter change of layered oxide cathodes is also heterogeneous. Tan et al. identified highly oxidized Ni around cracks in charged NMC811 particles, showing correlation between heterogeneousness of charged state and crack formation.[161] Heterogeneousness of mechanical degradation is also seen in our thesis (Figure 45, Chapter 5), where there existed a region with few cracks and little delamination, and the other region with many cracks and severe delamination. We expect the issue in All-Solid-State Batteries would be more severe compared to the conventional cell with liquid environment. Even local crack formation at cathode|solid electrolyte can completely disconnect cathode particle from solid electrolyte, leading to irreversible capacity loss.

Further study combining microscopy techniques (for structural analysis), and spectroscopy techniques (for chemical analysis) are required to fully understand the nature of heterogeneousness and is effect on electrochemical performance. Yu et al. performed in-situ X-ray Fluorescence Microscopy combined with X-ray absorption Spectroscopy on Li-S batteries to investigate heterogeneous electrochemical reaction at the interface during cycling.[162] We have demonstrated in chapter 4 that in-operando XAS characterization of cathode|solid electrolyte interface is possible with the model cell that we developed. Therefore, we expect study of

chemical heterogeneity at the interface with in-operando X-ray Fluorescence Microscopy to be possible. Correlation of findings on heterogeneousness in both electrochemical degradation and chemo-mechanical degradation will give more complete understanding of interfacial degradation during cell operation.

References

(1) Placke, T.; Kloepsch, R.; Dühnen, S.; Winter, M. Lithium Ion, Lithium Metal, and Alternative Rechargeable Battery Technologies: The Odyssey for High Energy Density. *J Solid State Electrochem* **2017**, *21* (7), 1939–1964. https://doi.org/10.1007/s10008-017-3610-7.

(2) Judez, X.; Eshetu, G. G.; Li, C.; Rodriguez-Martinez, L. M.; Zhang, H.; Armand, M. Opportunities for Rechargeable Solid-State Batteries Based on Li-Intercalation Cathodes. *Joule* **2018**, *2* (11), 2208–2224. https://doi.org/10.1016/j.joule.2018.09.008.

(3) Goodenough, J. B.; Kim, Y. Challenges for Rechargeable Li Batteries †. *Chemistry of Materials* **2010**, *22* (3), 587–603. https://doi.org/10.1021/cm901452z.

(4) Gerischer, H.; Decker, F.; Scrosati, B. The Electronic and the Ionic Contribution to the Free Energy of Alkali Metals in Intercalation Compounds. *J. Electrochem. Soc.* **1994**, *141* (9), 2297–2300. https://doi.org/10.1149/1.2055115.

(5) Hess, S.; Wohlfahrt-Mehrens, M.; Wachtler, M. Flammability of Li-Ion Battery Electrolytes: Flash Point and Self-Extinguishing Time Measurements. *Journal of The Electrochemical Society* **2015**, *162* (2), A3084–A3097. https://doi.org/10.1149/2.0121502jes.

(6) Xu, K. Nonaqueous Liquid Electrolytes for Lithium-Based Rechargeable Batteries. *Chemical Reviews* **2004**, *104* (10), 4303–4418. https://doi.org/10.1021/cr030203g.

(7) Kim, K. J.; Balaish, M.; Wadaguchi, M.; Kong, L.; Rupp, J. L. M. Solid-State Li–Metal Batteries: Challenges and Horizons of Oxide and Sulfide Solid Electrolytes and Their Interfaces. *Advanced Energy Materials* **2021**, *11* (1), 2002689. https://doi.org/10.1002/aenm.202002689.

(8) Cano, Z. P.; Banham, D.; Ye, S.; Hintennach, A.; Lu, J.; Fowler, M.; Chen, Z. Batteries and Fuel Cells for Emerging Electric Vehicle Markets. *Nat Energy* **2018**, *3* (4), 279–289. https://doi.org/10.1038/s41560-018-0108-1.

(9) Han, F.; Zhu, Y.; He, X.; Mo, Y.; Wang, C. Electrochemical Stability of $Li_{10}GeP_2S_{12}$ and $Li_7La_3Zr_2O_{12}$ Solid Electrolytes. *Adv. Energy Mater.* **2016**, *6* (8), 1501590. https://doi.org/10.1002/aenm.201501590.

(10) Richards, W. D.; Miara, L. J.; Wang, Y.; Kim, J. C.; Ceder, G. Interface Stability in Solid-State Batteries. *Chemistry of Materials* **2016**, *28* (1), 266–273. https://doi.org/10.1021/acs.chemmater.5b04082.

(11) Sharafi, A.; Kazyak, E.; Davis, A. L.; Yu, S.; Thompson, T.; Siegel, D. J.; Dasgupta, N. P.; Sakamoto, J. Surface Chemistry Mechanism of Ultra-Low Interfacial Resistance in the Solid-State Electrolyte $Li_7La_3Zr_2O_{12}$. *Chem. Mater.* **2017**, *29* (18), 7961–7968. https://doi.org/10.1021/acs.chemmater.7b03002.

(12) Ren, Y.; Shen, Y.; Lin, Y.; Nan, C.-W. Direct Observation of Lithium Dendrites inside Garnet-Type Lithium-Ion Solid Electrolyte. *Electrochemistry Communications* **2015**, *57*, 27–30. https://doi.org/10.1016/j.elecom.2015.05.001.

(13) Cheng, E. J.; Sharafi, A.; Sakamoto, J. Intergranular Li Metal Propagation through Polycrystalline $Li_{6.25}Al_{0.25}La_3Zr_2O_{12}$ Ceramic Electrolyte. *Electrochimica Acta* **2017**, *223*, 85–91. https://doi.org/10.1016/j.electacta.2016.12.018.

(14) Tsai, C.-L.; Roddatis, V.; Chandran, C. V.; Ma, Q.; Uhlenbruck, S.; Bram, M.; Heitjans, P.; Guillon, O. $Li_7La_3Zr_2O_{12}$ Interface Modification for Li Dendrite Prevention. *ACS Appl. Mater. Interfaces* **2016**, *8* (16), 10617–10626. https://doi.org/10.1021/acsami.6b00831.

(15) Duan, H.; Yin, Y.-X.; Shi, Y.; Wang, P.-F.; Zhang, X.-D.; Yang, C.-P.; Shi, J.-L.; Wen, R.; Guo, Y.-G.; Wan, L.-J. Dendrite-Free Li-Metal Battery Enabled by a Thin Asymmetric Solid Electrolyte with Engineered Layers. *J. Am. Chem. Soc.* **2018**, *140* (1), 82–85. https://doi.org/10.1021/jacs.7b10864.

(16) Wu, B.; Wang, S.; Lochala, J.; Desrochers, D.; Liu, B.; Zhang, W.; Yang, J.; Xiao, J. The Role of the Solid Electrolyte Interphase Layer in Preventing Li Dendrite Growth in Solid-State Batteries. *Energy Environ. Sci.* **2018**, *11* (7), 1803–1810. https://doi.org/10.1039/C8EE00540K.
(17) Smetaczek, S.; Pycha, E.; Ring, J.; Siebenhofer, M.; Ganschow, S.; Berendts, S.; Nenning, A.; Kubicek, M.; Rettenwander, D.; Limbeck, A.; Fleig, J. Investigating the Electrochemical Stability of $Li_7La_3Zr_2O_{12}$ Solid Electrolytes Using Field Stress Experiments. *J. Mater. Chem. A* **2021**, *9* (27), 15226–15237. https://doi.org/10.1039/D1TA02983E.
(18) Nolan, A. M.; Wachsman, E. D.; Mo, Y. Computation-Guided Discovery of Coating Materials to Stabilize the Interface between Lithium Garnet Solid Electrolyte and High-Energy Cathodes for All-Solid-State Lithium Batteries. *Energy Storage Materials* **2021**, *41*, 571–580. https://doi.org/10.1016/j.ensm.2021.06.027.
(19) Xiao, Y.; Miara, L. J.; Wang, Y.; Ceder, G. Computational Screening of Cathode Coatings for Solid-State Batteries. *Joule* **2019**, *3* (5), 1252–1275. https://doi.org/10.1016/j.joule.2019.02.006.
(20) Liu, H. S.; Zhang, Z. R.; Gong, Z. L.; Yang, Y. Origin of Deterioration for $LiNiO_2$ Cathode Material during Storage in Air. *Electrochemical and Solid-State Letters* **2004**, *7* (7), A190. https://doi.org/10.1149/1.1738471.
(21) Liu, H.; Yang, Y.; Zhang, J. Investigation and Improvement on the Storage Property of $LiNi_{0.8}Co_{0.2}O_2$ as a Cathode Material for Lithium-Ion Batteries. *Journal of Power Sources* **2006**, *162* (1), 644–650. https://doi.org/10.1016/j.jpowsour.2006.07.028.
(22) Sharafi, A.; Yu, S.; Naguib, M.; Lee, M.; Ma, C.; M. Meyer, H.; Nanda, J.; Chi, M.; J. Siegel, D.; Sakamoto, J. Impact of Air Exposure and Surface Chemistry on Li–$Li_7La_3Zr_2O_{12}$ Interfacial Resistance. *Journal of Materials Chemistry A* **2017**, *5* (26), 13475–13487. https://doi.org/10.1039/C7TA03162A.
(23) Xia, W.; Xu, B.; Duan, H.; Tang, X.; Guo, Y.; Kang, H.; Li, H.; Liu, H. Reaction Mechanisms of Lithium Garnet Pellets in Ambient Air: The Effect of Humidity and CO_2. *J Am Ceram Soc* **2017**, *100* (7), 2832–2839. https://doi.org/10.1111/jace.14865.
(24) Bak, S.-M.; Hu, E.; Zhou, Y.; Yu, X.; Senanayake, S. D.; Cho, S.-J.; Kim, K.-B.; Chung, K. Y.; Yang, X.-Q.; Nam, K.-W. Structural Changes and Thermal Stability of Charged $LiNi_xMn_yCo_zO_2$ Cathode Materials Studied by Combined *In Situ* Time-Resolved XRD and Mass Spectroscopy. *ACS Applied Materials & Interfaces* **2014**, *6* (24), 22594–22601. https://doi.org/10.1021/am506712c.
(25) Kim, K. H.; Iriyama, Y.; Yamamoto, K.; Kumazaki, S.; Asaka, T.; Tanabe, K.; Fisher, C. A. J.; Hirayama, T.; Murugan, R.; Ogumi, Z. Characterization of the Interface between $LiCoO_2$ and $Li_7La_3Zr_2O_{12}$ in an All-Solid-State Rechargeable Lithium Battery. *Journal of Power Sources* **2011**, *196* (2), 764–767. https://doi.org/10.1016/j.jpowsour.2010.07.073.
(26) Ren, Y.; Liu, T.; Shen, Y.; Lin, Y.; Nan, C.-W. Chemical Compatibility between Garnet-like Solid State Electrolyte $Li_{6.75}La_3Zr_{1.75}Ta_{0.25}O_{12}$ and Major Commercial Lithium Battery Cathode Materials. *Journal of Materiomics* **2016**, *2* (3), 256–264. https://doi.org/10.1016/j.jmat.2016.04.003.
(27) Yu, C.-Y.; Choi, J.; Han, J.; Lee, E.; Kim, J.-H. Phase Stability of Garnet Solid-Electrolyte Interfacing with Various Cathodes in All Solid-State Batteries. *J. Electrochem. Soc.* **2022**, *169*, 020520. https://doi.org/10.1149/1945-7111/ac4e5b.
(28) Hong, S.; Song, S. H.; Cho, M.; Kim, S.; Yu, S.-H.; Lee, D.; Kim, H. Structural and Chemical Compatibilities of $Li_{1-x}Ni_{0.5}Co_{0.2}Mn_{0.3}O_2$ Cathode Material with Garnet-Type Solid Electrolyte for All-Solid-State Batteries. *Small* **2021**, *17* (46), 2103306. https://doi.org/10.1002/smll.202103306.
(29) Wakasugi, J.; Munakata, H.; Kanamura, K. Thermal Stability of Various Cathode Materials against $Li_{6.25}Al_{0.25}La_3Zr_2O_{12}$ Electrolyte. *Electrochemistry* **2017**, *85* (2), 77–81. https://doi.org/10.5796/electrochemistry.85.77.
(30) Uhlenbruck, S.; Dornseiffer, J.; Lobe, S.; Dellen, C.; Tsai, C.-L.; Gotzen, B.; Sebold, D.; Finsterbusch, M.; Guillon, O. Cathode-Electrolyte Material Interactions during Manufacturing of Inorganic Solid-

State Lithium Batteries. *Journal of Electroceramics* **2017**, *38* (2–4), 197–206. https://doi.org/10.1007/s10832-016-0062-x.
(31) Park, K.; Yu, B.-C.; Jung, J.-W.; Li, Y.; Zhou, W.; Gao, H.; Son, S.; Goodenough, J. B. Electrochemical Nature of the Cathode Interface for a Solid-State Lithium-Ion Battery: Interface between $LiCoO_2$ and Garnet-$Li_7La_3Zr_2O_{12}$. *Chem. Mater.* **2016**, *28* (21), 8051–8059. https://doi.org/10.1021/acs.chemmater.6b03870.
(32) Zhang, N.; Long, X.; Wang, Z.; Yu, P.; Han, F.; Fu, J.; Ren, G.; Wu, Y.; Zheng, S.; Huang, W.; Wang, C.; Li, H.; Liu, X. Mechanism Study on the Interfacial Stability of a Lithium Garnet-Type Oxide Electrolyte against Cathode Materials. *ACS Applied Energy Materials* **2018**, *1* (11), 5968–5976. https://doi.org/10.1021/acsaem.8b01035.
(33) Quilty, C. D.; Bock, D. C.; Yan, S.; Takeuchi, K. J.; Takeuchi, E. S.; Marschilok, A. C. Probing Sources of Capacity Fade in $LiNi_{0.6}Mn_{0.2}Co_{0.2}O_2$ (NMC622): An *Operando* XRD Study of Li/NMC622 Batteries during Extended Cycling. *J. Phys. Chem. C* **2020**, *124* (15), 8119–8128. https://doi.org/10.1021/acs.jpcc.0c00262.
(34) Barai, P.; Rojas, T.; Narayanan, B.; Ngo, A. T.; Curtiss, L. A.; Srinivasan, V. Investigation of Delamination-Induced Performance Decay at the Cathode/LLZO Interface. *Chem. Mater.* **2021**, *33* (14), 5527–5541. https://doi.org/10.1021/acs.chemmater.0c04656.
(35) Liu, T.; Zhang, Y.; Chen, R.; Zhao, S.-X.; Lin, Y.; Nan, C.-W.; Shen, Y. Non-Successive Degradation in Bulk-Type All-Solid-State Lithium Battery with Rigid Interfacial Contact. *Electrochemistry Communications* **2017**, *79*, 1–4. https://doi.org/10.1016/j.elecom.2017.03.016.
(36) Besli, M. M.; Xia, S.; Kuppan, S.; Huang, Y.; Metzger, M.; Shukla, A. K.; Schneider, G.; Hellstrom, S.; Christensen, J.; Doeff, M. M.; Liu, Y. Mesoscale Chemomechanical Interplay of the $LiNi_{0.8}Co_{0.15}Al_{0.05}O_2$ Cathode in Solid-State Polymer Batteries. *Chem. Mater.* **2019**, *31* (2), 491–501. https://doi.org/10.1021/acs.chemmater.8b04418.
(37) Vardar, G.; Bowman, W. J.; Lu, Q.; Wang, J.; Chater, R. J.; Aguadero, A.; Seibert, R.; Terry, J.; Hunt, A.; Waluyo, I.; Fong, D. D.; Jarry, A.; Crumlin, E. J.; Hellstrom, S. L.; Chiang, Y.-M.; Yildiz, B. Structure, Chemistry, and Charge Transfer Resistance of the Interface between $Li_7La_3Zr_2O_{12}$ Electrolyte and $LiCoO_2$ Cathode. *Chemistry of Materials* **2018**, *30* (18), 6259–6276. https://doi.org/10.1021/acs.chemmater.8b01713.
(38) Chebiam, R. V.; Kannan, A. M.; Prado, F.; Manthiram, A. Comparison of the Chemical Stability of the High Energy Density Cathodes of Lithium-Ion Batteries. *Electrochemistry Communications* **2001**, *3* (11), 624–627. https://doi.org/10.1016/S1388-2481(01)00232-6.
(39) Zheng, J.; Liu, T.; Hu, Z.; Wei, Y.; Song, X.; Ren, Y.; Wang, W.; Rao, M.; Lin, Y.; Chen, Z.; Lu, J.; Wang, C.; Amine, K.; Pan, F. Tuning of Thermal Stability in Layered $Li(Ni_xMn_yCo_z)O_2$. *Journal of the American Chemical Society* **2016**, *138* (40), 13326–13334. https://doi.org/10.1021/jacs.6b07771.
(40) Li, W.; Song, B.; Manthiram, A. High-Voltage Positive Electrode Materials for Lithium-Ion Batteries. *Chem. Soc. Rev.* **2017**, *46* (10), 3006–3059. https://doi.org/10.1039/C6CS00875E.
(41) Stöhr, J. *NEXAFS Spectroscopy*; Springer: Berlin; London, 2011.
(42) Wang, B.; Bates, J. B.; Hart, F. X.; Sales, B. C.; Zuhr, R. A.; Robertson, J. D. Characterization of Thin-Film Rechargeable Lithium Batteries with Lithium Cobalt Oxide Cathodes. *J. Electrochem. Soc.* **1996**, *143* (10), 3203. https://doi.org/10.1149/1.1837188.
(43) Zhu, X.; Guo, Z.; Du, G.; Zhang, P.; Liu, H. $LiCoO_2$ Cathode Thin Film Fabricated by RF Sputtering for Lithium Ion Microbatteries. *Surface and Coatings Technology* **2010**, *204* (11), 1710–1714. https://doi.org/10.1016/j.surfcoat.2009.10.057.
(44) Kim, H.-S.; Oh, Y.; Kang, K. H.; Kim, J. H.; Kim, J.; Yoon, C. S. Characterization of Sputter-Deposited $LiCoO_2$ Thin Film Grown on NASICON-Type Electrolyte for Application in All-Solid-State Rechargeable Lithium Battery. *ACS Appl. Mater. Interfaces* **2017**, *9* (19), 16063–16070. https://doi.org/10.1021/acsami.6b15305.

(45) Bates, J. B.; Dudney, N. J.; Neudecker, B. J.; Hart, F. X.; Jun, H. P.; Hackney, S. A. Preferred Orientation of Polycrystalline $LiCoO_2$ Films. *Journal of The Electrochemical Society* **2000**, *147* (1), 59–70. https://doi.org/10.1149/1.1393157.
(46) de Groot, F. M. F.; Grioni, M.; Fuggle, J. C.; Ghijsen, J.; Sawatzky, G. A.; Petersen, H. Oxygen 1*s* x-Ray-Absorption Edges of Transition-Metal Oxides. *Phys. Rev. B* **1989**, *40* (8), 5715–5723. https://doi.org/10.1103/PhysRevB.40.5715.
(47) Suntivich, J.; Hong, W. T.; Lee, Y.-L.; Rondinelli, J. M.; Yang, W.; Goodenough, J. B.; Dabrowski, B.; Freeland, J. W.; Shao-Horn, Y. Estimating Hybridization of Transition Metal and Oxygen States in Perovskites from O *K* -Edge X-Ray Absorption Spectroscopy. *J. Phys. Chem. C* **2014**, *118* (4), 1856–1863. https://doi.org/10.1021/jp410644j.
(48) Cheng, L.; Crumlin, E. J.; Chen, W.; Qiao, R.; Hou, H.; Lux, S. F.; Zorba, V.; Russo, R.; Kostecki, R.; Liu, Z.; Persson, K.; Yang, W.; Cabana, J.; Richardson, T.; Chen, G.; Doeff, M. The Origin of High Electrolyte–Electrode Interfacial Resistances in Lithium Cells Containing Garnet Type Solid Electrolytes. *Phys. Chem. Chem. Phys.* **2014**, *16* (34), 18294–18300. https://doi.org/10.1039/C4CP02921F.
(49) Hwang, S.; Kim, S. M.; Bak, S.-M.; Kim, S. Y.; Cho, B.-W.; Chung, K. Y.; Lee, J. Y.; Stach, E. A.; Chang, W. Using Real-Time Electron Microscopy To Explore the Effects of Transition-Metal Composition on the Local Thermal Stability in Charged $Li_x Ni_y Mn_z Co_{1-y-z} O_2$ Cathode Materials. *Chemistry of Materials* **2015**, *27* (11), 3927–3935. https://doi.org/10.1021/acs.chemmater.5b00709.
(50) Tian, C.; Nordlund, D.; Xin, H. L.; Xu, Y.; Liu, Y.; Sokaras, D.; Lin, F.; Doeff, M. M. Depth-Dependent Redox Behavior of $LiNi_{0.6}Mn_{0.2}Co_{0.2}O_2$. *Journal of The Electrochemical Society* **2018**, *165* (3), A696–A704. https://doi.org/10.1149/2.1021803jes.
(51) Lin, F.; Markus, I. M.; Nordlund, D.; Weng, T.-C.; Asta, M. D.; Xin, H. L.; Doeff, M. M. Surface Reconstruction and Chemical Evolution of Stoichiometric Layered Cathode Materials for Lithium-Ion Batteries. *Nature Communications* **2014**, *5* (1). https://doi.org/10.1038/ncomms4529.
(52) Xu, J.; Hu, E.; Nordlund, D.; Mehta, A.; Ehrlich, S. N.; Yang, X.-Q.; Tong, W. Understanding the Degradation Mechanism of Lithium Nickel Oxide Cathodes for Li-Ion Batteries. *ACS Appl. Mater. Interfaces* **2016**, *8* (46), 31677–31683. https://doi.org/10.1021/acsami.6b11111.
(53) Merz, M.; Nagel, P.; Pinta, C.; Samartsev, A.; v. Löhneysen, H.; Wissinger, M.; Uebe, S.; Assmann, A.; Fuchs, D.; Schuppler, S. X-Ray Absorption and Magnetic Circular Dichroism of $LaCoO_3$, $La_{0.7}Ce_{0.3}CoO_3$, and $La_{0.7}Sr_{0.3}CoO_3$ Films: Evidence for Cobalt-Valence-Dependent Magnetism. *Physical Review B* **2010**, *82* (17). https://doi.org/10.1103/PhysRevB.82.174416.
(54) Huang, M.-J. The Electronic Structure and Magnetic Interactions in the Mixed Transition-Metal Oxide La(Co,Ni)O_3 Studied by X-Ray Absorption Spectroscopies. Doctor of Science, Karlsruher Instituts für Technologie, 2016.
(55) Pérez, J.; García, J.; Blasco, J.; Stankiewicz, J. Spin-Glass Behavior and Giant Magnetoresistance in the (RE)$Ni_{0.3}Co_{0.7}O_3$ (RE = La, Nd, Sm) System. *Phys. Rev. Lett.* **1998**, *80* (11), 2401–2404. https://doi.org/10.1103/PhysRevLett.80.2401.
(56) Miyoshi, S.; Yamaguchi, S. Soft X-Ray Absorption and Photoemission Study on the Electronic Structure of (La,Sr)CoO_3. *ECS Transactions* **2015**, *68* (1), 591–597. https://doi.org/10.1149/06801.0591ecst.
(57) Karvonen, L.; Valkeapää, M.; Liu, R.-S.; Chen, J.-M.; Yamauchi, H.; Karppinen, M. O-*K* and Co-*L* XANES Study on Oxygen Intercalation in Perovskite $SrCoO_{3-\delta}$. *Chem. Mater.* **2010**, *22* (1), 70–76. https://doi.org/10.1021/cm9021563.
(58) Henderson, G. S.; de Groot, F. M. F.; Moulton, B. J. A. X-Ray Absorption Near-Edge Structure (XANES) Spectroscopy. *Reviews in Mineralogy and Geochemistry* **2014**, *78* (1), 75–138. https://doi.org/10.2138/rmg.2014.78.3.

(59) Gilbert, B.; Frazer, B. H.; Belz, A.; Conrad, P. G.; Nealson, K. H.; Haskel, D.; Lang, J. C.; Srajer, G.; De Stasio, G. Multiple Scattering Calculations of Bonding and X-Ray Absorption Spectroscopy of Manganese Oxides. *J. Phys. Chem. A* **2003**, *107* (16), 2839–2847. https://doi.org/10.1021/jp021493s.

(60) Bak, S.-M.; Nam, K.-W.; Chang, W.; Yu, X.; Hu, E.; Hwang, S.; Stach, E. A.; Kim, K.-B.; Chung, K. Y.; Yang, X.-Q. Correlating Structural Changes and Gas Evolution during the Thermal Decomposition of Charged $Li_xNi_{0.8}Co_{0.15}Al_{0.05}O_2$ Cathode Materials. *Chemistry of Materials* **2013**, *25* (3), 337–351. https://doi.org/10.1021/cm303096e.

(61) Aryal, S.; Timofeeva, E. V.; Segre, C. U. Structural Studies of Capacity Activation and Reduced Voltage Fading in Li-Rich, Mn-Ni-Fe Composite Oxide Cathode. *Journal of The Electrochemical Society* **2018**, *165* (2), A71–A78. https://doi.org/10.1149/2.0031802jes.

(62) Deb, A.; Bergmann, U.; Cramer, S. P.; Cairns, E. J. *In Situ* x-Ray Absorption Spectroscopic Study of the $Li[Ni_{1/3}Co_{1/3}Mn_{1/3}]O_2$ Cathode Material. *Journal of Applied Physics* **2005**, *97* (11), 113523. https://doi.org/10.1063/1.1921328.

(63) Jain, A.; Ong, S. P.; Hautier, G.; Chen, W.; Richards, W. D.; Dacek, S.; Cholia, S.; Gunter, D.; Skinner, D.; Ceder, G.; Persson, K. A. Commentary: The Materials Project: A Materials Genome Approach to Accelerating Materials Innovation. *APL Materials* **2013**, *1* (1), 011002. https://doi.org/10.1063/1.4812323.

(64) Langford, J. I.; Wilson, A. J. C. Scherrer after Sixty Years: A Survey and Some New Results in the Determination of Crystallite Size. *Journal of Applied Crystallography* **1978**, *11* (2), 102–113. https://doi.org/10.1107/S0021889878012844.

(65) Bouwman, P. J.; Boukamp, B. A.; Bouwmeester, H. J. M.; Wondergem, H. J.; Notten, P. H. L. Structural Analysis of Submicrometer $LiCoO_2$ Films. *Journal of The Electrochemical Society* **2001**, *148* (4), A311–A317. https://doi.org/10.1149/1.1353570.

(66) Jeon, S.-W.; Lim, J.-K.; Lim, S.-H.; Lee, S.-M. As-Deposited $LiCoO_2$ Thin Film Cathodes Prepared by Rf Magnetron Sputtering. *Electrochimica Acta* **2005**, *51* (2), 268–273. https://doi.org/10.1016/j.electacta.2005.04.035.

(67) Rettenwander, D.; Welzl, A.; Cheng, L.; Fleig, J.; Musso, M.; Suard, E.; Doeff, M. M.; Redhammer, G. J.; Amthauer, G. Synthesis, Crystal Chemistry, and Electrochemical Properties of $Li_{7-2x}La_3Zr_{2-x}Mo_xO_{12}$ (x = 0.1–0.4): Stabilization of the Cubic Garnet Polymorph via Substitution of Zr^{4+} by Mo^{6+}. *Inorg. Chem.* **2015**, *54* (21), 10440–10449. https://doi.org/10.1021/acs.inorgchem.5b01895.

(68) Wachter-Welzl, A.; Kirowitz, J.; Wagner, R.; Smetaczek, S.; Brunauer, G. C.; Bonta, M.; Rettenwander, D.; Taibl, S.; Limbeck, A.; Amthauer, G.; Fleig, J. The Origin of Conductivity Variations in Al-Stabilized $Li_7La_3Zr_2O_{12}$ Ceramics. *Solid State Ionics* **2018**, *319*, 203–208. https://doi.org/10.1016/j.ssi.2018.01.036.

(69) Wachter-Welzl, A.; Wagner, R.; Rettenwander, D.; Taibl, S.; Amthauer, G.; Fleig, J. Microelectrodes for Local Conductivity and Degradation Measurements on Al Stabilized $Li_7La_3Zr_2O_{12}$ Garnets. *J Electroceram* **2017**, *38* (2), 176–181. https://doi.org/10.1007/s10832-016-0058-6.

(70) Chen, Y.; Rangasamy, E.; dela Cruz, C. R.; Liang, C.; An, K. A Study of Suppressed Formation of Low-Conductivity Phases in Doped $Li_7La_3Zr_2O_{12}$ Garnets by in Situ Neutron Diffraction. *J. Mater. Chem. A* **2015**, *3* (45), 22868–22876. https://doi.org/10.1039/C5TA04902D.

(71) Alonso, J. A.; Sanz, J.; Santamaría, J.; León, C.; Várez, A.; Fernández-Díaz, M. T. On the Location of Li^+ Cations in the Fast Li-Cation Conductor $La_{0.5}Li_{0.5}TiO_3$ Perovskite. *Angewandte Chemie International Edition* **2000**, *39* (3), 619–621. https://doi.org/10.1002/(SICI)1521-3773(20000204)39:3<619::AID-ANIE619>3.0.CO;2-O.

(72) Ebrahiminia, M.; Hooper, J.; Bedrov, D. Structural, Mechanical, and Dynamical Properties of Amorphous Li_2CO_3 from Molecular Dynamics Simulations. *Crystals* **2018**, *8* (12), 473. https://doi.org/10.3390/cryst8120473.

(73) Reed, J.; Ceder, G. Role of Electronic Structure in the Susceptibility of Metastable Transition-Metal Oxide Structures to Transformation. *Chemical Reviews* **2004**, *104* (10), 4513–4534. https://doi.org/10.1021/cr020733x.
(74) Hoang, K.; Johannes, M. Defect Physics and Chemistry in Layered Mixed Transition Metal Oxide Cathode Materials: (Ni,Co,Mn) vs (Ni,Co,Al). *Chem. Mater.* **2016**, *28* (5), 1325–1334. https://doi.org/10.1021/acs.chemmater.5b04219.
(75) Gu, M.; Belharouak, I.; Genc, A.; Wang, Z.; Wang, D.; Amine, K.; Gao, F.; Zhou, G.; Thevuthasan, S.; Baer, D. R.; Zhang, J.-G.; Browning, N. D.; Liu, J.; Wang, C. Conflicting Roles of Nickel in Controlling Cathode Performance in Lithium Ion Batteries. *Nano Lett.* **2012**, *12* (10), 5186–5191. https://doi.org/10.1021/nl302249v.
(76) Moradabadi, A.; Kaghazchi, P. Mechanism of Li Intercalation/Deintercalation into/from the Surface of $LiCoO_2$. *Phys. Chem. Chem. Phys.* **2015**, *17* (35), 22917–22922. https://doi.org/10.1039/C5CP02246K.
(77) Ning, F.; Li, S.; Xu, B.; Ouyang, C. Strain Tuned Li Diffusion in $LiCoO_2$ Material for Li Ion Batteries: A First Principles Study. *Solid State Ionics* **2014**, *263*, 46–48. https://doi.org/10.1016/j.ssi.2014.05.008.
(78) Ong, S. P.; Chevrier, V. L.; Hautier, G.; Jain, A.; Moore, C.; Kim, S.; Ma, X.; Ceder, G. Voltage, Stability and Diffusion Barrier Differences between Sodium-Ion and Lithium-Ion Intercalation Materials. *Energy Environ. Sci.* **2011**, *4* (9), 3680. https://doi.org/10.1039/c1ee01782a.
(79) Manthiram, A. Electrical Energy Storage: Materials Challenges and Prospects. *MRS Bulletin* **2016**, *41* (8), 624–631. https://doi.org/10.1557/mrs.2016.167.
(80) Xiao, Y.; Wang, Y.; Bo, S.-H.; Kim, J. C.; Miara, L. J.; Ceder, G. Understanding Interface Stability in Solid-State Batteries. *Nat Rev Mater* **2020**, *5* (2), 105–126. https://doi.org/10.1038/s41578-019-0157-5.
(81) Kim, Y.; Kim, D.; Bliem, R.; Vardar, G.; Waluyo, I.; Hunt, A.; Wright, J. T.; Katsoudas, J. P.; Yildiz, B. Thermally Driven Interfacial Degradation between $Li_7La_3Zr_2O_{12}$ Electrolyte and $LiNi_{0.6}Mn_{0.2}Co_{0.2}O_2$ Cathode. *Chem. Mater.* **2020**, *32* (22), 9531–9541. https://doi.org/10.1021/acs.chemmater.0c02261.
(82) Zhu, Y.; He, X.; Mo, Y. First Principles Study on Electrochemical and Chemical Stability of Solid Electrolyte–Electrode Interfaces in All-Solid-State Li-Ion Batteries. *Journal of Materials Chemistry A* **2016**, *4* (9), 3253–3266. https://doi.org/10.1039/C5TA08574H.
(83) Ohta, S.; Komagata, S.; Seki, J.; Saeki, T.; Morishita, S.; Asaoka, T. All-Solid-State Lithium Ion Battery Using Garnet-Type Oxide and Li3BO3 Solid Electrolytes Fabricated by Screen-Printing. *Journal of Power Sources* **2013**, *238*, 53–56. https://doi.org/10.1016/j.jpowsour.2013.02.073.
(84) Han, F.; Yue, J.; Chen, C.; Zhao, N.; Fan, X.; Ma, Z.; Gao, T.; Wang, F.; Guo, X.; Wang, C. Interphase Engineering Enabled All-Ceramic Lithium Battery. *Joule* **2018**, *2* (3), 497–508. https://doi.org/10.1016/j.joule.2018.02.007.
(85) Kato, T.; Hamanaka, T.; Yamamoto, K.; Hirayama, T.; Sagane, F.; Motoyama, M.; Iriyama, Y. In-Situ Li7La3Zr2O12/LiCoO2 Interface Modification for Advanced All-Solid-State Battery. *Journal of Power Sources* **2014**, *260*, 292–298. https://doi.org/10.1016/j.jpowsour.2014.02.102.
(86) Sastre, J.; Chen, X.; Aribia, A.; Tiwari, A. N.; Romanyuk, Y. E. Fast Charge Transfer across the $Li_7La_3Zr_2O_{12}$ Solid Electrolyte/$LiCoO_2$ Cathode Interface Enabled by an Interphase-Engineered All-Thin-Film Architecture. *ACS Appl. Mater. Interfaces* **2020**, *12* (32), 36196–36207. https://doi.org/10.1021/acsami.0c09777.
(87) Wang, D.; Sun, Q.; Luo, J.; Liang, J.; Sun, Y.; Li, R.; Adair, K.; Zhang, L.; Yang, R.; Lu, S.; Huang, H.; Sun, X. Mitigating the Interfacial Degradation in Cathodes for High-Performance Oxide-Based Solid-State Lithium Batteries. *ACS Appl. Mater. Interfaces* **2019**, *11* (5), 4954–4961. https://doi.org/10.1021/acsami.8b17881.

(88) Chase, M. W. *NIST-JANAF Themochemical Tables*, 4th ed.; Journal of Physical and Chemical Reference Data, Monograph 9; 1998.
(89) Il'ina, E. A.; Raskovalov, A. A.; Reznitskikh, O. G. Thermodynamic Properties of Solid Electrolyte $Li_7La_3Zr_2O_{12}$. *The Journal of Chemical Thermodynamics* **2019**, *128*, 68–73. https://doi.org/10.1016/j.jct.2018.08.009.
(90) Gotcu-Freis, P.; Cupid, D. M.; Rohde, M.; Seifert, H. J. New Experimental Heat Capacity and Enthalpy of Formation of Lithium Cobalt Oxide. *The Journal of Chemical Thermodynamics* **2015**, *84*, 118–127. https://doi.org/10.1016/j.jct.2014.12.007.
(91) Bolech, M.; Cordfunke, E. H. P.; Van Genderen, A. C. G.; Van Der Laan, R. R.; Janssen, F. J. J. G.; Van Miltenburg, J. C. The Heat Capacity and Derived Thermodynamic Functions of $La_2Zr_2O_7$ and $Ce_2Zr_2O_7$ from 4 to 1000K. *Journal of Physics and Chemistry of Solids* **1997**, *58* (3), 433–439. https://doi.org/10.1016/S0022-3697(06)00137-5.
(92) Stølen, S.; Grønvold, F.; Brinks, H.; Atake, T.; Mori, H. Heat Capacity and Thermodynamic Properties of $LaFeO_3$ and $LaCoO_3$ from T=13K to T=1000K. *The Journal of Chemical Thermodynamics* **1998**, *30* (3), 365–377. https://doi.org/10.1006/jcht.1997.0309.
(93) Wang, M. Enthalpy of Formation of $LiNiO_2$, $LiCoO_2$ and Their Solid Solution, $LiNi_{1-x}Co_xO_2$. *Solid State Ionics* **2004**, *166* (1–2), 167–173. https://doi.org/10.1016/j.ssi.2003.11.004.
(94) Cheng, J.; Navrotsky, A.; Zhou, X.-D.; Anderson, H. U. Enthalpies of Formation of $LaMO_3$ Perovskites (M = Cr, Fe, Co, and Ni). *J. Mater. Res.* **2005**, *20* (1), 191–200. https://doi.org/10.1557/JMR.2005.0018.
(95) Guo, E.-J.; Liu, Y.; Sohn, C.; Desautels, R. D.; Herklotz, A.; Liao, Z.; Nichols, J.; Freeland, J. W.; Fitzsimmons, M. R.; Lee, H. N. Oxygen Diode Formed in Nickelate Heterostructures by Chemical Potential Mismatch. *Advanced Materials* **2018**, *30* (15), 1705904. https://doi.org/10.1002/adma.201705904.
(96) Zhong, Y.; Dai, J.; Xu, X.; Su, C.; Shao, Z. Facilitating Oxygen Redox on Manganese Oxide Nanosheets by Tuning Active Species and Oxygen Defects for Zinc-Air Batteries. *ChemElectroChem* **2020**, *7* (24), 4949–4955. https://doi.org/10.1002/celc.202001419.
(97) Toma, T.; Maezono, R.; Hongo, K. Electrochemical Properties and Crystal Structure of Li^+/H^+ Cation-Exchanged $LiNiO_2$. *ACS Appl. Energy Mater.* **2020**, acsaem.0c00602. https://doi.org/10.1021/acsaem.0c00602.
(98) Shkrob, I. A.; Gilbert, J. A.; Phillips, P. J.; Klie, R.; Haasch, R. T.; Bareño, J.; Abraham, D. P. Chemical Weathering of Layered Ni-Rich Oxide Electrode Materials: Evidence for Cation Exchange. *J. Electrochem. Soc.* **2017**, *164* (7), A1489–A1498. https://doi.org/10.1149/2.0861707jes.
(99) Moshtev, R.; Zlatilova, P.; Vasilev, S.; Bakalova, I.; Kozawa, A. Synthesis, XRD Characterization and Electrochemical Performance of Overlithiated $LiNiO_2$. *Journal of Power Sources* **1999**, *81–82*, 434–441. https://doi.org/10.1016/S0378-7753(99)00247-5.
(100) Pritzl, D.; Teufl, T.; Freiberg, A. T. S.; Strehle, B.; Sicklinger, J.; Sommer, H.; Hartmann, P.; Gasteiger, H. A. Editors' Choice—Washing of Nickel-Rich Cathode Materials for Lithium-Ion Batteries: Towards a Mechanistic Understanding. *J. Electrochem. Soc.* **2019**, *166* (16), A4056–A4066. https://doi.org/10.1149/2.1351915jes.
(101) Jeong, S.; Kim, J.; Mun, J. Self-Generated Coating of $LiCoO_2$ by Washing and Heat Treatment without Coating Precursors. *J. Electrochem. Soc.* **2019**, *166* (3), A5038–A5044. https://doi.org/10.1149/2.0071903jes.
(102) Li, N.; Bediako, D. K.; Hadt, R. G.; Hayes, D.; Kempa, T. J.; von Cube, F.; Bell, D. C.; Chen, L. X.; Nocera, D. G. Influence of Iron Doping on Tetravalent Nickel Content in Catalytic Oxygen Evolving Films. *Proc Natl Acad Sci USA* **2017**, *114* (7), 1486–1491. https://doi.org/10.1073/pnas.1620787114.

(103) Qiao, R.; Chuang, Y.-D.; Yan, S.; Yang, W. Soft X-Ray Irradiation Effects of Li_2O_2, Li_2CO_3 and Li_2O Revealed by Absorption Spectroscopy. *PLoS ONE* **2012**, *7* (11), e49182. https://doi.org/10.1371/journal.pone.0049182.

(104) de Groot, F. M. F.; Hu, Z. W.; Lopez, M. F.; Kaindl, G.; Guillot, F.; Tronc, M. Differences between L_3 and L_2 X-ray Absorption Spectra of Transition Metal Compounds. *The Journal of Chemical Physics* **1994**, *101* (8), 6570–6576. https://doi.org/10.1063/1.468351.

(105) May, F.; Tischer, M.; Arvanitis, D.; Russo, M.; Dunn, J. H.; Henneken, H.; Wende, H.; Chauvistré, R.; Mårtensson, N.; Baberschke, K. Modifications of the Electronic and Magnetic Properties of Ultrathin Ni/Cu(100) Films Induced by Stepwise Oxidation. *Phys. Rev. B* **1996**, *53* (3), 1076–1079. https://doi.org/10.1103/PhysRevB.53.1076.

(106) Kim, M.-S.; Hwang, T.-S.; Kim, K.-B. A Study of the Electrochemical Redox Behavior of Electrochemically Precipitated Nickel Hydroxides Using Electrochemical Quartz Crystal Microbalance. *J. Electrochem. Soc.* **1997**, *144* (5), 1537. https://doi.org/10.1149/1.1837637.

(107) Lin, F.; Markus, I. M.; Nordlund, D.; Weng, T.-C.; Asta, M. D.; Xin, H. L.; Doeff, M. M. Surface Reconstruction and Chemical Evolution of Stoichiometric Layered Cathode Materials for Lithium-Ion Batteries. *Nature Communications* **2014**, *5* (1). https://doi.org/10.1038/ncomms4529.

(108) Pan, J.; Sun, Y.; Wan, P.; Wang, Z.; Liu, X. Synthesis, Characterization and Electrochemical Performance of Battery Grade NiOOH. *Electrochemistry Communications* **2005**, *7* (8), 857–862. https://doi.org/10.1016/j.elecom.2005.05.004.

(109) Ikeno, H.; Tanaka, I.; Koyama, Y.; Mizoguchi, T.; Ogasawara, K. First-Principles Multielectron Calculations of Ni $L_{2,3}$ NEXAFS and ELNES for $LiNiO_2$ and Related Compounds. *Phys. Rev. B* **2005**, *72* (7), 075123. https://doi.org/10.1103/PhysRevB.72.075123.

(110) Montoro, L. A.; Abbate, M.; Almeida, E. C.; Rosolen, J. M. Electronic Structure of the Transition Metal Ions in $LiCoO_2$, $LiNiO_2$ and $LiCo_{0.5}Ni_{0.5}O_2$. *Chemical Physics Letters* **1999**, *309* (1–2), 14–18. https://doi.org/10.1016/S0009-2614(99)00650-8.

(111) Groot, F. M. F. de; Abbate, M.; Elp, J. van; Sawatzky, G. A.; Ma, Y. J.; Chen, C. T.; Sette, F. Oxygen 1s and Cobalt 2p X-Ray Absorption of Cobalt Oxides. *J. Phys.: Condens. Matter* **1993**, *5* (14), 2277–2288. https://doi.org/10.1088/0953-8984/5/14/023.

(112) van Elp, J.; Wieland, J. L.; Eskes, H.; Kuiper, P.; Sawatzky, G. A.; de Groot, F. M. F.; Turner, T. S. Electronic Structure of CoO, Li-Doped CoO, and $LiCoO_2$. *Phys. Rev. B* **1991**, *44* (12), 6090–6103. https://doi.org/10.1103/PhysRevB.44.6090.

(113) Irvine, J. T. S.; Sinclair, D. C.; West, A. R. Electroceramics: Characterization by Impedance Spectroscopy. *Advanced Materials* **1990**, *2* (3), 132–138. https://doi.org/10.1002/adma.19900020304.

(114) Reimanis, I.; Kleebe, H.-J. A Review on the Sintering and Microstructure Development of Transparent Spinel ($MgAl_2O_4$). *Journal of the American Ceramic Society* **2009**, *92* (7), 1472–1480. https://doi.org/10.1111/j.1551-2916.2009.03108.x.

(115) Guo, J.; Guo, H.; Baker, A. L.; Lanagan, M. T.; Kupp, E. R.; Messing, G. L.; Randall, C. A. Cold Sintering: A Paradigm Shift for Processing and Integration of Ceramics. *Angewandte Chemie International Edition* **2016**, *55* (38), 11457–11461. https://doi.org/10.1002/anie.201605443.

(116) Berbano, S. S.; Guo, J.; Guo, H.; Lanagan, M. T.; Randall, C. A. Cold Sintering Process of $Li_{1.5}Al_{0.5}Ge_{1.5}(PO_4)_3$ Solid Electrolyte. *J Am Ceram Soc* **2017**, *100* (5), 2123–2135. https://doi.org/10.1111/jace.14727.

(117) Seo, J.-H.; Verlinde, K.; Guo, J.; Heidary, D. S. B.; Rajagopalan, R.; Mallouk, T. E.; Randall, C. A. Cold Sintering Approach to Fabrication of High Rate Performance Binderless $LiFePO_4$ Cathode with High Volumetric Capacity. *Scripta Materialia* **2018**, *146*, 267–271. https://doi.org/10.1016/j.scriptamat.2017.12.005.

(118) Cheng, X.; Huang, J.; Qiang, W.; Huang, B. Synthesis of Mixed Ionic and Electronic Conducting Garnet with Doping of Transition Elements (Fe, Co, Ni). *Ceramics International* **2020**, *46* (3), 3731–3737. https://doi.org/10.1016/j.ceramint.2019.10.094.

(119) Noh, H.-J.; Youn, S.; Yoon, C. S.; Sun, Y.-K. Comparison of the Structural and Electrochemical Properties of Layered Li[NixCoyMnz]O2 (x = 1/3, 0.5, 0.6, 0.7, 0.8 and 0.85) Cathode Material for Lithium-Ion Batteries. *Journal of Power Sources* **2013**, *233*, 121–130. https://doi.org/10.1016/j.jpowsour.2013.01.063.

(120) Jung, R.; Metzger, M.; Maglia, F.; Stinner, C.; Gasteiger, H. A. Oxygen Release and Its Effect on the Cycling Stability of $LiNi_x Mn_yCo_zO_2$ (NMC) Cathode Materials for Li-Ion Batteries. *Journal of The Electrochemical Society* **2017**, *164* (7), A1361–A1377. https://doi.org/10.1149/2.0021707jes.

(121) Zhang, W.; Richter, F. H.; Culver, S. P.; Leichtweiss, T.; Lozano, J. G.; Dietrich, C.; Bruce, P. G.; Zeier, W. G.; Janek, J. Degradation Mechanisms at the $Li_{10}GeP_2S_{12}/LiCoO_2$ Cathode Interface in an All-Solid-State Lithium-Ion Battery. *ACS Applied Materials & Interfaces* **2018**, *10* (26), 22226–22236. https://doi.org/10.1021/acsami.8b05132.

(122) Wang, C.; Hwang, S.; Jiang, M.; Liang, J.; Sun, Y.; Adair, K.; Zheng, M.; Mukherjee, S.; Li, X.; Li, R.; Huang, H.; Zhao, S.; Zhang, L.; Lu, S.; Wang, J.; Singh, C. V.; Su, D.; Sun, X. Deciphering Interfacial Chemical and Electrochemical Reactions of Sulfide-Based All-Solid-State Batteries. *Adv. Energy Mater.* **2021**, *11* (24), 2100210. https://doi.org/10.1002/aenm.202100210.

(123) Liu, T.; Zhang, Y.; Chen, R.; Zhao, S.-X.; Lin, Y.; Nan, C.-W.; Shen, Y. Non-Successive Degradation in Bulk-Type All-Solid-State Lithium Battery with Rigid Interfacial Contact. *Electrochemistry Communications* **2017**, *79*, 1–4. https://doi.org/10.1016/j.elecom.2017.03.016.

(124) Liu, X.; Zheng, B.; Zhao, J.; Zhao, W.; Liang, Z.; Su, Y.; Xie, C.; Zhou, K.; Xiang, Y.; Zhu, J.; Wang, H.; Zhong, G.; Gong, Z.; Huang, J.; Yang, Y. Electrochemo-Mechanical Effects on Structural Integrity of Ni-Rich Cathodes with Different Microstructures in All Solid-State Batteries. *Adv. Energy Mater.* **2021**, *11* (8), 2003583. https://doi.org/10.1002/aenm.202003583.

(125) Troy, S.; Schreiber, A.; Reppert, T.; Gehrke, H.-G.; Finsterbusch, M.; Uhlenbruck, S.; Stenzel, P. Life Cycle Assessment and Resource Analysis of All-Solid-State Batteries. *Applied Energy* **2016**, *169*, 757–767. https://doi.org/10.1016/j.apenergy.2016.02.064.

(126) Tuson, G. B.; Kobayashi, H.; Campbell, M. J. *Oxygen Enriched Combustion System Performance Study. Phase 2: 100 Percent Oxygen Enriched Combustion in Regenerative Glass Melters, Final Report*; United States, 1994. https://doi.org/10.2172/10196777.

(127) Dunn, J. B.; Gaines, L.; Kelly, J. C.; James, C.; Gallagher, K. G. The Significance of Li-Ion Batteries in Electric Vehicle Life-Cycle Energy and Emissions and Recycling's Role in Its Reduction. *Energy Environ. Sci.* **2015**, *8* (1), 158–168. https://doi.org/10.1039/C4EE03029J.

(128) Larraz, G.; Orera, A.; Sanjuán, M. L. Cubic Phases of Garnet-Type Li7La3Zr2O12: The Role of Hydration. *Journal of Materials Chemistry A* **2013**, *1* (37), 11419. https://doi.org/10.1039/c3ta11996c.

(129) Yow, Z. F.; Oh, Y. L.; Gu, W.; Rao, R. P.; Adams, S. Effect of Li+/H+ Exchange in Water Treated Ta-Doped Li7La3Zr2O12. *Solid State Ionics* **2016**, *292*, 122–129. https://doi.org/10.1016/j.ssi.2016.05.016.

(130) Liu, C.; Rui, K.; Shen, C.; Badding, M. E.; Zhang, G.; Wen, Z. Reversible Ion Exchange and Structural Stability of Garnet-Type Nb-Doped $Li_7La_3Zr_2O_{12}$ in Water for Applications in Lithium Batteries. *Journal of Power Sources* **2015**, *282*, 286–293. https://doi.org/10.1016/j.jpowsour.2015.02.050.

(131) Cui, Y.; Schubert, B. A.; Jahren, A. H. A 23 m.y. Record of Low Atmospheric CO_2. *Geology* **2020**, *48* (9), 888–892. https://doi.org/10.1130/G47681.1.

(132) Xu, S.; Jacobs, R. M.; Nguyen, H. M.; Hao, S.; Mahanthappa, M.; Wolverton, C.; Morgan, D. Lithium Transport through Lithium-Ion Battery Cathode Coatings. *J. Mater. Chem. A* **2015**, *3* (33), 17248–17272. https://doi.org/10.1039/C5TA01664A.

(133) Kim, A.; Woo, S.; Kang, M.; Park, H.; Kang, B. Research Progresses of Garnet-Type Solid Electrolytes for Developing All-Solid-State Li Batteries. *Front. Chem.* **2020**, *8*, 468. https://doi.org/10.3389/fchem.2020.00468.

(134) Kang, S.-J. L. (Suk-J. L.). *Sintering : Densification, Grain Growth, and Microstructure*; Elsevier Butterworth-Heinemann: Amsterdam ;, 2005.

(135) Dixit, M.; Markovsky, B.; Schipper, F.; Aurbach, D.; Major, D. T. Origin of Structural Degradation During Cycling and Low Thermal Stability of Ni-Rich Layered Transition Metal-Based Electrode Materials. *J. Phys. Chem. C* **2017**, *121* (41), 22628–22636. https://doi.org/10.1021/acs.jpcc.7b06122.

(136) Koerver, R.; Aygün, I.; Leichtweiß, T.; Dietrich, C.; Zhang, W.; Binder, J. O.; Hartmann, P.; Zeier, W. G.; Janek, J. Capacity Fade in Solid-State Batteries: Interphase Formation and Chemomechanical Processes in Nickel-Rich Layered Oxide Cathodes and Lithium Thiophosphate Solid Electrolytes. *Chemistry of Materials* **2017**, *29* (13), 5574–5582. https://doi.org/10.1021/acs.chemmater.7b00931.

(137) Renfrew, S. E.; McCloskey, B. D. Quantification of Surface Oxygen Depletion and Solid Carbonate Evolution on the First Cycle of $LiNi_{0.6}Mn_{0.2}Co_{0.2}O_2$ Electrodes. *ACS Appl. Energy Mater.* **2019**, *2* (5), 3762–3772. https://doi.org/10.1021/acsaem.9b00459.

(138) Vernon, M. W. ANOMALIES IN THE ELECTRICAL CONDUCTIVITY OF NICKEL OXIDE ABOVE ROOM TEMPERATURE. 7.

(139) Mahato, R. N.; Sethupathi, K.; Sankaranarayanan, V. Colossal Magnetoresistance in the Double Perovskite Oxide La_2CoMnO_6. *Journal of Applied Physics* **2010**, *107* (9), 09D714. https://doi.org/10.1063/1.3350907.

(140) Fu, X.-Z.; Zhu, Y.-J.; Xu, Q.-C.; Li, J.; Pan, J.-H.; Xu, J.-Q.; Lin, J.-D.; Liao, D.-W. Nickel Oxyhydroxides with Various Oxidation States Prepared by Chemical Oxidation of Spherical β-Ni(OH)2. *Solid State Ionics* **2007**, *178* (13–14), 987–993. https://doi.org/10.1016/j.ssi.2007.04.011.

(141) Al Samarai, M.; Hahn, A. W.; Beheshti Askari, A.; Cui, Y.-T.; Yamazoe, K.; Miyawaki, J.; Harada, Y.; Rüdiger, O.; DeBeer, S. Elucidation of Structure–Activity Correlations in a Nickel Manganese Oxide Oxygen Evolution Reaction Catalyst by Operando Ni L-Edge X-Ray Absorption Spectroscopy and 2p3d Resonant Inelastic X-Ray Scattering. *ACS Appl. Mater. Interfaces* **2019**, *11* (42), 38595–38605. https://doi.org/10.1021/acsami.9b06752.

(142) Kim, S.; Aykol, M.; Hegde, V. I.; Lu, Z.; Kirklin, S.; Croy, J. R.; Thackeray, M. M.; Wolverton, C. Material Design of High-Capacity Li-Rich Layered-Oxide Electrodes: Li_2MnO_3 and Beyond. *Energy Environ. Sci.* **2017**, *10* (10), 2201–2211. https://doi.org/10.1039/C7EE01782K.

(143) Migeon, H.-N.; Zanne, M.; Gleitzer, C.; Aubry, J. The Li_2O-NiO-O System at 670°C and the Consequences of Non-Stoichiometry on the Magnetic Properties of the $Li_xNi_{1-x}O_{1+\pm y}$ Phases. *JOURNAL OF MATERIALS SCIENCE* **1978**, *13*, 461–466.

(144) Xue, W.; Huang, M.; Li, Y.; Zhu, Y. G.; Gao, R.; Xiao, X.; Zhang, W.; Li, S.; Xu, G.; Yu, Y.; Li, P.; Lopez, J.; Yu, D.; Dong, Y.; Fan, W.; Shi, Z.; Xiong, R.; Sun, C.-J.; Hwang, I.; Lee, W.-K.; Shao-Horn, Y.; Johnson, J. A.; Li, J. Ultra-High-Voltage Ni-Rich Layered Cathodes in Practical Li Metal Batteries Enabled by a Sulfonamide-Based Electrolyte. *Nat Energy* **2021**, *6* (5), 495–505. https://doi.org/10.1038/s41560-021-00792-y.

(145) Liu, H.; Wolf, M.; Karki, K.; Yu, Y.-S.; Stach, E. A.; Cabana, J.; Chapman, K. W.; Chupas, P. J. Intergranular Cracking as a Major Cause of Long-Term Capacity Fading of Layered Cathodes. *Nano Lett.* **2017**, *17* (6), 3452–3457. https://doi.org/10.1021/acs.nanolett.7b00379.

(146) Sun, G.; Sui, T.; Song, B.; Zheng, H.; Lu, L.; Korsunsky, A. M. On the Fragmentation of Active Material Secondary Particles in Lithium Ion Battery Cathodes Induced by Charge Cycling. *Extreme Mechanics Letters* **2016**, *9*, 449–458. https://doi.org/10.1016/j.eml.2016.03.018.
(147) Kondrakov, A. O.; Schmidt, A.; Xu, J.; Geßwein, H.; Mönig, R.; Hartmann, P.; Sommer, H.; Brezesinski, T.; Janek, J. Anisotropic Lattice Strain and Mechanical Degradation of High- and Low-Nickel NCM Cathode Materials for Li-Ion Batteries. *J. Phys. Chem. C* **2017**, *121* (6), 3286–3294. https://doi.org/10.1021/acs.jpcc.6b12885.
(148) Ming-Yuan, H.; Hutchinson, J. W. Crack Deflection at an Interface between Dissimilar Elastic Materials. *International Journal of Solids and Structures* **1989**, *25* (9), 1053–1067. https://doi.org/10.1016/0020-7683(89)90021-8.
(149) Huddleston, W.; Dynys, F.; Sehirlioglu, A. Effects of Microstructure on Fracture Strength and Conductivity of Sintered NMC333. *J Am Ceram Soc* **2020**, *103* (3), 1527–1535. https://doi.org/10.1111/jace.16829.
(150) Xu, R.; Sun, H.; de Vasconcelos, L. S.; Zhao, K. Mechanical and Structural Degradation of $LiNi_xMn_yCo_zO_2$ Cathode in Li-Ion Batteries: An Experimental Study. *J. Electrochem. Soc.* **2017**, *164* (13), A3333–A3341. https://doi.org/10.1149/2.1751713jes.
(151) Shi, F.; Song, Z.; Ross, P. N.; Somorjai, G. A.; Ritchie, R. O.; Komvopoulos, K. Failure Mechanisms of Single-Crystal Silicon Electrodes in Lithium-Ion Batteries. *Nat Commun* **2016**, *7* (1), 11886. https://doi.org/10.1038/ncomms11886.
(152) Wolfenstine, J.; Jo, H.; Cho, Y.-H.; David, I. N.; Askeland, P.; Case, E. D.; Kim, H.; Choe, H.; Sakamoto, J. A Preliminary Investigation of Fracture Toughness of $Li_7La_3Zr_2O_{12}$ and Its Comparison to Other Solid Li-Ionconductors. *Materials Letters* **2013**, *96*, 117–120. https://doi.org/10.1016/j.matlet.2013.01.021.
(153) Zehnder, A. T. *Fracture Mechanics*; Lecture Notes in Applied and Computational Mechanics; Springer Netherlands: Dordrecht, 2012; Vol. 62. https://doi.org/10.1007/978-94-007-2595-9.
(154) Sun, C. T.; Jin, Z.-H. Chapter 2 - Griffith Theory of Fracture. In *Fracture Mechanics*; Sun, C. T., Jin, Z.-H., Eds.; Academic Press: Boston, 2012; pp 11–24. https://doi.org/10.1016/B978-0-12-385001-0.00002-X.
(155) Kramer, D.; Ceder, G. Tailoring the Morphology of $LiCoO_2$: A First Principles Study. *Chem. Mater.* **2009**, *21* (16), 3799–3809. https://doi.org/10.1021/cm9008943.
(156) Thompson, T.; Yu, S.; Williams, L.; Schmidt, R. D.; Garcia-Mendez, R.; Wolfenstine, J.; Allen, J. L.; Kioupakis, E.; Siegel, D. J.; Sakamoto, J. Electrochemical Window of the Li-Ion Solid Electrolyte $Li_7La_3Zr_2O_{12}$. *ACS Energy Letters* **2017**, *2* (2), 462–468. https://doi.org/10.1021/acsenergylett.6b00593.
(157) Ma, Y.; Chen, M.; Yan, Y.; Wei, Y.; Liu, W.; Zhang, X.; Li, J.; Fu, Z.; Li, J.; Zhang, X. Annealing of $LiCoO_2$ Films on Flexible Stainless Steel for Thin Film Lithium Batteries. *J. Mater. Res.* **2020**, *35* (1), 31–41. https://doi.org/10.1557/jmr.2019.299.
(158) Strauss, F.; de Biasi, L.; Kim, A.-Y.; Hertle, J.; Schweidler, S.; Janek, J.; Hartmann, P.; Brezesinski, T. Rational Design of Quasi-Zero-Strain NCM Cathode Materials for Minimizing Volume Change Effects in All-Solid-State Batteries. *ACS Materials Lett.* **2020**, *2* (1), 84–88. https://doi.org/10.1021/acsmaterialslett.9b00441.
(159) He, M.; Cui, Z.; Han, F.; Guo, X. Construction of Conductive and Flexible Composite Cathodes for Room-Temperature Solid-State Lithium Batteries. *Journal of Alloys and Compounds* **2018**, *762*, 157–162. https://doi.org/10.1016/j.jallcom.2018.05.255.
(160) Tian, C.; Xu, Y.; Nordlund, D.; Lin, F.; Liu, J.; Sun, Z.; Liu, Y.; Doeff, M. Charge Heterogeneity and Surface Chemistry in Polycrystalline Cathode Materials. *Joule* **2018**, *2* (3), 464–477. https://doi.org/10.1016/j.joule.2017.12.008.

(161) Tan, C.; Leach, A. S.; Heenan, T. M. M.; Parks, H.; Jervis, R.; Weker, J. N.; Brett, D. J. L.; Shearing, P. R. Nanoscale State-of-Charge Heterogeneities within Polycrystalline Nickel-Rich Layered Oxide Cathode Materials. *Cell Reports Physical Science* **2021**, *2* (12), 100647. https://doi.org/10.1016/j.xcrp.2021.100647.

(162) Yu, X.; Pan, H.; Zhou, Y.; Northrup, P.; Xiao, J.; Bak, S.; Liu, M.; Nam, K.-W.; Qu, D.; Liu, J.; Wu, T.; Yang, X.-Q. Direct Observation of the Redistribution of Sulfur and Polysufides in Li-S Batteries During the First Cycle by In Situ X-Ray Fluorescence Microscopy. *Adv. Energy Mater.* **2015**, *5* (16), 1500072. https://doi.org/10.1002/aenm.201500072.